Investigations into Electrochemical CO_2 Reduction Catalysts *via* Gas Diffusion Electrodes

by

Ella Fidment

A thesis presented for the degree of

Doctor of Philosophy

School of Natural and Environmental Sciences

Newcastle University, UK

March 2024

Abstract

The advancement of carbon dioxide (CO_2) electroreduction technology is crucial for addressing climate change by transforming CO_2 into valuable chemicals and fuels. eCO2RR offers a route to decarbonise energy requirements for industries where energy-dense molecules are typically used to provide energy, such as aviation and domestic heating. However, developing catalysts that afford selectivity towards multi-carbon products is still the focus of much research. With longer reduction pathways requiring more electrons, multi-carbon products are still hard to produce at significant rates. Furthermore, degradation of the gas diffusion electrode is an issue under the electrochemical conditions for CO_2 electroreduction. Flooding of the gas diffusion electrode reduces the availability of CO_2 at the ideal triple phase reaction centres and hence the selectivity towards carbonaceous products reduces and hydrogen evolution (HER) increases. This thesis presents research on the optimization of gas diffusion electrodes for CO_2 electroreduction, focusing on the effects of bimetallic catalyst selectivity and hydrophobicity.

The hypothesis of this work was the addition of gold with the Cu_2O catalyst would have a higher faradaic efficiency for multi-carbon products. The catalytic performance of Au-Cu_2O bimetallic catalysts in gas diffusion electrodes was evaluated and it showed enhanced selectivity for CO_2 reduction to ethanol and propanol when compared to the Cu_2O catalyst. The research found that the presence of gold in the catalyst composition significantly influences the reaction pathway by facilitating CO insertion and dimerization, leading to a higher selectivity for C2+ oxygenates over ethylene.

Chapter 4 presents the work on Au decorated Cu_2O microparticles via electrodeposition were observed to produce higher faradaic efficiency of longer chain alcohols compared to Cu_2O microparticles, however the overall rate of production of carbonaceous products decreased. The rate of ethanol and propanol production increased by 2 and 4.5 nmol s^{-1} cm^{-2} respectively with the $AuCu_2O$ compared to Cu_2O. Overall the inclusion of gold in the catalytic layer resulted in higher *CO concentration which favoured high length carbon products. Faradaic efficiency of hydrogen was marginally lower at 16% faradaic efficiency with $AuCu_2O$ with respect to Cu_2O.

In exploring the role of hydrophobicity, the impact of modifying gas diffusion layers with hydrophobic additives was assessed. Nanoporous carbon particles, functionalized with polyfluoroaromatic compounds, were employed aiming to enhance CO_2 diffusion whilst maintaining hydrophobicity. The hypothesis of this work was that the use of polyfluorophenyl carbons as an additive in the catalyst layer would prevent flooding in the gas diffusion electrode. Initial results indicate that these hydrophobic substrates improve the faradaic efficiency for carbon monoxide production with Ag catalysts. However, the durability of hydrophobicity under electrochemical conditions poses a challenge, as the effectiveness of these additives decreases over time, affecting the overall stability and efficiency of the CO_2 reduction process.

The hydrophobicity of nanoporous carbon particles functionalised with fluorophenyl molecules was measured with capacitance in different potential windows and compared to nanoporous carbons absent of functionalisation. It was found that the capacitance per mass was 2.69 F/g of PhF_5CIC with respect to a capacitance per mass of 10.92 F/g of CIC. When a more negative potential window was applied, the capacitance of PhF_5CIC per mass increased to 6.8 F/g for the PhF_5CIC, providing evidence for electrowetting of PhF_5CIC.

PhF_5CIC was utilised as a hydrophobic additive in the catalyst layer with Ag particles and the ratio of CO/H_2 was measured. At 5 min, the ratio of CO/H_2 faradaic efficiency was 50, showing preference of CO_2 electroreduction with respect to HER. However, under longer electrochemical conditions, the CO/H_2 faradaic efficiency ratio lowered to 3 at 22 min, indicating electrolyte intrusion. This is in agreement with the capacitance studies conducted to measure hydrophobicity, whereby hydrophobicity of PhF_5CIC decreases significantly under electrochemical conditions.

Table of Contents

Nomenclature

List of Main Abbreviations

BET	Brunauer–Emmett–Teller
BSE	Back scatter electron
CL	Catalyst layer
CO2RR	CO_2 electroreduction reaction
CV	Cyclic voltammetry
DFT	Density functional theory
DLS	Dynamic Light Scattering
E	Potential
ECSA	Electrochemical surface area
EDXS	Energy-dispersive X-ray spectroscopy
GC	Gas chromatography
GDE	Gas diffusion electrode
GDL	Gas diffusion layer
GHG	Greenhouse gases
HER	Hydrogen evolution reaction
IC	Ion chromatography
IPCC	Intergovernmental Panel on Climate Change

MD	Molecular dynamics
MPL	Microporous layer
MPS	Macroporous substrate
NA	$n \sin(\alpha)$
NP	Nanoparticles
P2X	Power-to-X
RHE	Reversible hydrogen electrode
RWGS	Reverse water gas shift
SEM	Scanning electron microscopy
WCA	Water contact angle

Table of Figure

Figure 5-5 (next page) a) CVs within the 0.4-0.7 V vs. RHE window for CIC85 material drop cast onto a glassy carbon electrode from a water-based ink with an additive of Nafion. The scan rate varies from 10 mV/s to 140 mV/s overall. The reference electrode was a mercury based RE-61AP and counter electrode was a graphite electrode. The electrolyte was degassed with argon and was 0.1 M KOH. B) The current value of the CVs displayed in a) of this figure were extracted at 0.52 V vs. RHE and their absolute value was plotted. Both the forward (blue) and backward (orange) sweep is shown. A linear equation is used to fit this data, where y = ax + c. The gradient is presented for both the forward and backward sweep. The R^2 values are shown to evaluate fit quality. C) The CVs of the PhF_5CIC85 material are shown here with the same experimental conditions as discussed for a). D) The current values were extracted at 0.52 V vs. RHE from Figure C). E) The calculated values of capacitance per mass are shown. Capacitance is calculated as an average of the forward and backward gradient values, shown as a in Figure b and d. The mass used was the total mass of the material used (CIC85 = 11.58 mg, PhF_5CIC85 = 11.73 mg) divided by the amount of catalyst ink pipetted onto the glassy carbon electrode (28 mL) as ratio of the total amount of catalyst ink (1.4 mL). 142

Figure 5-6 (next page) a) CVs in different potential windows (0.0-0.4 V vs. RHE and 0.4 – 0.7 V vs. RHE) for the same CIC85 sample are shown. The scanrates vary from 10mV/s top 140 mV/s. The 0.4-0.7 V vs. RHE window CVs were conducted first. Then a chronoamperometry measurement at 0.05V vs. RHE was done. Then the 0-0.4 V vs. RHE window CVs were performed. The current is divided by mass of the material deposited onto the glassy carbon electrode (11.58 mg divided by 28 µL of catalyst ink deposited from the overall volume of catalyst ink created 1.4 mL). B) CVs in different potentials windows for the PhF_5CIC85 material. C) Capacitance per mass in the 0.4-0.7 V vs. RHE and 0.0 – 0.4 V vs. RHE window. These values

SEM imaging was employed to observe whether morphological changes to the PhF_5CIC85 occurred

A film of PhF_5CIC85 was studied under SEM, as shown in **Figure 5-14.**. In all previous work related to capacitance measurements, a 5 cm glassy carbon rod electrode was the electrode upon which all the films were drop-casted onto. In order for the films to be imaged in the SEM equipment, the glassy carbon rod was swapped for glassy carbon discs that were 0.5 cm in length and are electrically contacted within the electrode holder as seen in Figure 5-14a). The different architecture of the electrode (i.e. the rubber seal between the glassy carbon electrode and the plastic body of the holder and the plastic body itself) caused the electrolyte and air to behave differently to the surface of the PhF_5CIC85 film. Therefore, an air bubble formed on the surface of the electrode which could be seen in Figure 5-15a) and is highlighted by a blue ring in in Figure 5-16 d) and in Figure 5-17e). The air bubble could not be replaced with electrolyte due to the highly hydrophobic character of the film and experiments were conducted regardless. But, overall, this provided an opportunity to measure SEM on a sample, which contained areas that had been in contact with electrolyte and undergone electrochemical testing, and a “clean” area in the centre of the film which had not. It was possible to image the surfaces of both areas and perform EDS. 153

1

Introduction

In this chapter we will discuss the fundamental research objective that this thesis will discuss.

1.1 Motivation: The Challenges of Climate Change

Since the Industrial Revolution, the concentration of CO_2 in the atmosphere has significantly increased due to emissions from fossil fuels and changes in land use, mainly deforestation.[1] As illustrated in Figure 2.1, the CO_2 concentration in the atmosphere has risen from approximately 278 parts per million (ppm) in 1740 to 417 ppm in 2022.[2] The rise in CO_2 and other greenhouse gases (GHG), including methane and nitrous oxide, has resulted in higher average temperatures, sea temperatures, more frequent and severe extreme weather events, rising sea levels, and reduced glacial ice volume, among other environmental impacts. [3] Climate change will cause significant environmental and social damage globally.

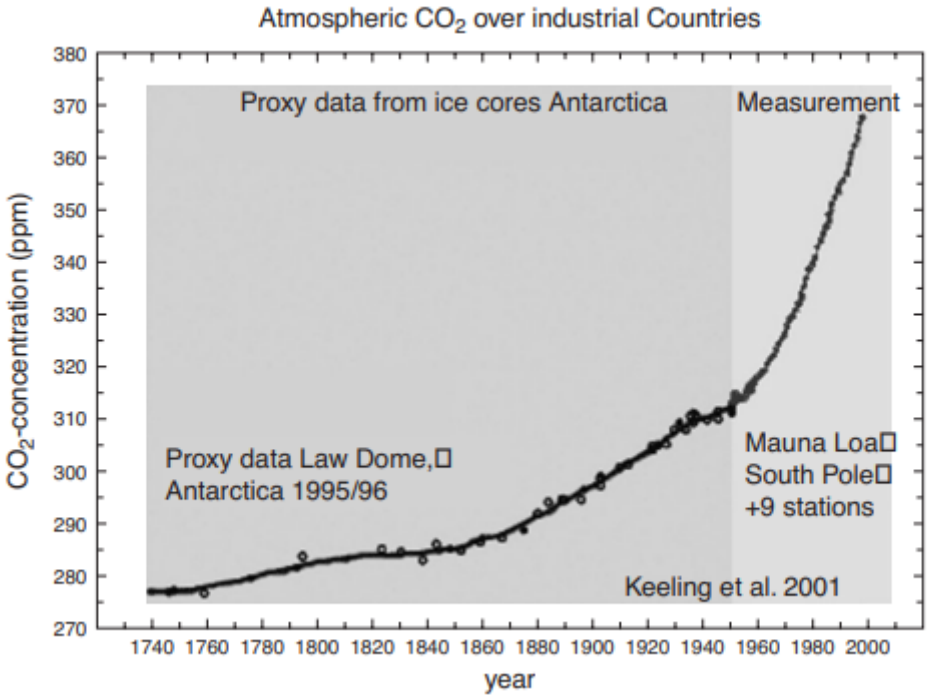

Figure 1-1 The calculated CO_2 concentration from ice cores pre-1950, and atmospheric measurements post-1950. Adapted from Beck et al. [4]

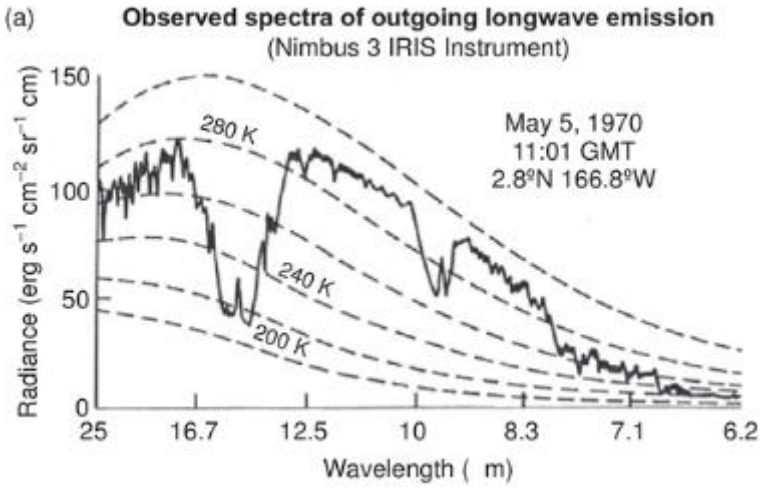

Figure 1-2 Spectrum of radiation measured by satellite, Nimbus 3 IRIS. [5]

The Greenhouse Effect is a physical phenomenon whereby CO_2 and other gases cause the Earth to heat up. [6] Figure 2-2 illustrates how the Earth re-emits solar radiation it has absorbed as black body radiation, represented by the dotted lines. A satellite recorded the radiation that reaches the outer atmosphere and shows a drop in emission at specific wavelengths. The

solid line represents the recorded emission spectra, while the dotted lines show the black body radiation at specified temperatures. The spectra significantly deviate from the dotted lines at certain wavelengths due to the absorption of those wavelengths by gases such as water vapour, carbon dioxide, and ozone. These gases absorb the electromagnetic spectrum and then re-emit it in all directions, including towards the lower atmosphere and the Earth's surface, resulting in heating. [6]

Greenhouse gases increase radiative forcing, which in turn increases the average global temperature. The effects of this warming are being measured today. The Sixth Assessment Report of the International Panel on Climate Change (IPCC) provides evidence of the physical changes that can be observed today as a result of 1.1 degrees C of global surface warming in 2011-2020 compared to 1850-1900.[3] These include glacial retreat not seen for 2,000 years, the last decade being warmer than any period in about 125,000 years, and sea levels rising faster than in any previous century for 3,000 years. In addition to these existing environmental changes, it is believed that further warming could trigger tipping points.[3] Tipping points are positive feedbacks that contribute to higher levels of greenhouse gas emissions, such as permafrost thawing or forest dieback.

Environmental impacts have global social consequences. Floods, droughts and crop shortages are predicted to increase as global temperatures rise. Reducing greenhouse gas (GHG) emissions is therefore a key objective. To limit global warming to 1.5 degrees Celsius, GHG emissions would need to be reduced by 43% by 2030 from 2019 levels.[3]

1.1.1 Climate-carbon cycle

The release of anthropogenic carbon dioxide into the atmosphere occurs as part of interconnected geophysical Earth processes. The carbon cycle is one of the Earth's systems where the net total of carbon is zero between the carbon allocations to land, sea and atmosphere.

$$B_{IM} = E_{FOS} + E_{LUC} - (G_{ATM} + S_{OCEAN} + S_{LAND}) \quad (1\text{-}1)$$

Understanding the different responses of carbon sinks is critical to understanding how anthropogenic CO_2 emissions led to atmospheric CO_2 concentrations. This is illustrated in equation 1. Currently, land and ocean carbon sinks have absorbed 53% of carbon emissions. When considering the equation used by the Global Carbon Project to calculate the carbon budget, the equation does not include anthropogenic carbon removal (which does not include land-based carbon removal such as afforestation) because the magnitude of carbon removal is a million times smaller than any other fluxes. Therefore, the current technological implementation of carbon removal has a negligible impact on carbon dioxide concentrations.

1.1.2 Renewable Energy

The global approach to reducing current CO_2 emissions has been to generate electricity using renewable energy technologies instead of burning fossil fuels.

However, with the introduction of renewable energy sources, such as wind and solar, issues related to the supply of electricity occur. Unpredictability and asynchronicity of generation with respect to energy consumption and inability to control the scale of generation compared

to traditional fossil fuels. These issues need to be addressed to ensure that energy needs can be met from renewable sources.

Specifically in the UK, the carbon intensity of electricity from the grid has decreased from 485 g to 261 g of CO_2 produced per kilowatt-hour (kWh) from 2000 to 2022.[7] Many factors contributed to the reduction of carbon intensity of electricity. These include: the switch from coal to gas combustion, the introduction of offshore wind, the maintenance of nuclear power and the introduction of residential and commercial solar photovoltaics. However significant challenges remain if the UK is to achieve its target of cutting emissions by 78% by 2035 compared to 1990 levels.[8] The demand for electricity is predicted to double due to the up take of electric powered vehicles and 7 out of the 8 of the UK's current nuclear power plants are due to be phased out by 2030.[9]

Despite the decarbonisation of electricity, not all energy-intensive lifestyle processes are easy to electrify. Domestic transport, which uses on liquid hydrocarbons, was responsible for 27% of greenhouse gas (GHG) emissions in the UK.[10] Heating of homes and commercial buildings is also a huge contributor to GHG emissions, due to the legacy of natural gas-fired boilers. In 2017, 92% of residential homes in the UK used a natural gas-fired boiler.[11]

Globally, the production of concrete results in significant carbon emissions, contributing to 8% of the world's CO_2 emissions.[12] Hence lots of processes of human activity result in the net emission of CO_2 to the atmosphere.

Looking at the main sources of greenhouse gas emissions, transport accounted for one fifth of global CO_2 emissions in 2016.[13] One method of reducing greenhouse gas emissions from

transport is to electrify road vehicles, aviation and shipping. However, a major obstacle for vehicles, such as trucks and aircraft, is that the specific energy required is much higher than the specific energy of today's batteries. After energy losses throughout the aircraft, the useful specific energy of jet fuel is 4,500 Wh/kg. This compares with 250 Wh/kg for a state-of-the-art battery.[14]

One avenue to address decarbonisation of transport is the use of Power-to-X (P2X) technology to enable the production of chemicals and fuels with a low carbon intensity. P2X technology enables the decarbonisation of hard-to-electrify industries, grid stability and seasonal energy storage.[15] P2X uses excess renewable electricity to convert abundant molecules to energy carriers, such as water to hydrogen and CO_2 to CO.

1.1.3 Applications of CO_2 reduction

CO_2 is a potential energy vector with surplus renewable energy, CO_2 can be converted into several different molecules that can be used in fuel cells.

1.2 Conversion of CO_2 to fuel

Within the last 100 years, many geopolitical events have stimulated research of CO_2 conversion, whilst the interest in CO_2 conversion has inversely trended with availability of oil.[16] For example, from circa. 1955 – 1970, oil supply was plentiful and hence interest in CO_2 conversion to fuel was marginal outside of academic groups. However, during the decades of the 1970s and 1980s, the 1973 oil crisis and forecast of dwindling oil reserves motivated research.[17] Within more recent years, the determination to find alternative sources to fossil fuel derived fuels and the concern to find less carbon intensive avenues for generating fuels and

chemical feedstocks is driven by alarm of climate change, fossil fuel reserves and national energy security.[17,18]

1.2.1 Thermocatalytic gas-phase CO_2 conversion

CO_2 can be reacted with more reduced molecules than itself at high temperatures in the presence of catalysts to convert it into molecules that are useful chemical feedstocks, such as syngas. It requires reactants, such as hydrogen or methane, and high-temperature reaction conditions.

Gas-phase CO_2 conversion is an attractive route for large point source carbon dioxide emitters (e.g., cement manufacturers, steel plants) to convert their CO_2 into industrially relevant chemical feedstocks.[19] However, there are significant hurdles with current catalysts. Noble metal catalysts are suitable for CO_2 methanation, RWGS reaction and methane reforming, but have limited availability and high cost. Transition metal catalysts offer an alternative but are subject to carbon deposition and sintering.

Table 1-1 Common thermocatalytic reactions of CO_2 conversions.

Molecule	Reaction Name	Reaction	Reference
Methane	CO_2 methanation Sabatier	$CO_2 + 4H_2 \leftrightarrow CH_4 + 2H_2O$ $\Delta H = -165$ kJ mol^{-1}	[20]
Carbon monoxide	Reverse water gas shift	$CO_2 + H_2 \leftrightarrow CO + H_2O$ $\Delta H = 41$ kJ mol^{-1}	[21]
Syngas	Dry reforming of methane	$CO_2 + CH_4 \leftrightarrow 2CO + 2H_2$ $\Delta H = 247.3$ kJ mol−1	[22]
Methanol or liquid products	Fischer Tropsch	nCO + 2nH$_2$ → –(CH$_2$)$_n$– + nH$_2$O	[23]

A recent development in the industrial implementation of dry reforming of methane is Linde's DRYREFTM, a commercial plant for reforming methane[24] with both steam and CO_2. BASF's SYNSPIRE novel nickel oxide catalyst is designed to withstand the coking process and therefore has an expected lifetime of 5-8 years.[25] However, dry methane reforming and these other processes still require high temperature and pressure operating conditions (850°C and 20-40 bar).

Thermocatalytic reactions are easy to scale up, but certain reactions, such as RWGS, may be limited by thermodynamic equilibrium and therefore the reaction requires a higher temperature to achieve single-pass conversion.[26,27]

The hydrogen required for CO_2 conversion via hydrogenation, such as RWGS, is predominantly generated by fossil fuels. In addition, thermocatalytic conversion of CO_2 requires significant energy input also provided by the burning of fossil fuels within an engine. Hence 5 of the thermocatalytic conversions of CO_2 via hydrogenation (3 direct processes of CO_2 to CO, CH_3OH and CH_4 and 2 indirect processes of CO_2 via CO intermediate to CH_3OH and CH_4) have been found to emit more CO_2 than it coverts when fossil fuel derived H_2 is used.[28]

1.2.2 Photocatalytic CO_2 conversion

One method of photocatalysis of liquid phase CO_2 is to use a wide band gap semiconductor such as TiO_2, where an electron is promoted from the valence band to the conduction band by the interaction of a short wavelength photon, creating an electron-hole pair.[29] The electron can be used as a reducing agent. However, the band gap of titanium is so large that only

photons with a wavelength of less than 380 nm can provide the energy required to promote electrons. One technique to overcome this problem is to dope semiconductors with non-metallic elements to introduce more filled orbitals and reduce the energy gap required.

Photocatalysis of CO_2 is difficult to achieve because CO_2 is a stable molecule and therefore requires significant energy to drive the reaction, which very few photocatalytic materials can provide. Finding an architecture of material(s) that can combine the role of photoexcitation of an electron and surface catalysis of an adsorbed CO_2 is very difficult, especially in reasonable quantities. It is difficult to reduce CO_2 at significant rates in the photocatalytic process.

1.2.3 Electrochemical CO_2 conversion

The electrochemical reduction of CO_2 (eCO2RR) occurs when external voltage is applied to an electrode in the presence of CO_2 in an electrochemical cell. Utilising electrical energy, CO_2 can be converted into several carbonaceous products, such as carbon monoxide and formate, as well as longer chain molecules, such as ethylene and ethanol.[30] Central to this technology is the role of electrocatalysts, which dictate the selectivity, rate and overpotential of the reaction. The electrochemical reaction can be conducted at atmospheric pressure and room temperature. This set-up can be compared to electrochemical reduction of water to hydrogen (HER) in an electrolyser. HER occurs simultaneously during eCO2RR at the cathode in aqueous electrolytes as a parasitic reaction because it more facile than the CO_2 reduction.[31]

Equations 1 to 7 show the reactions and thermodynamic potentials of the common products. The E_0 values close to 0V vs. RHE suggest that the reactions can occur at low potentials vs. RHE. However, the multiple electron transfer and intermediate activation energies require

high overpotentials to achieve high rates and faradaic efficiencies. By definition, C2+ products have more carbons within the molecule than C1 products. Per molecule of product, more electrons are required for C2 products. Each electron is thought to be added step-wise, hence C2 products have more intermediates which results in higher onset potentials to produce them. Furthermore, oxygenate products (such as alcohols and acids) are dissolved within the electrolyte and hence will require further energy and equipment to separate and isolate.[32]

Standard Thermodynamic Potentials of common products:

$$CO_2 + 2e^- + H^+ \rightarrow HCO_2^- \; E_0 = -0.02 \text{ V vs. RHE} \quad (1)$$

$$CO_2 + 2e^- + 2H^+ \rightarrow CO + H_2O \; E_0 = -0.10 \text{ V vs. RHE} \quad (2)$$

$$CO_2 + 8e^- + 8H^+ \rightarrow CH_4 + 2H_2O \; E_0 = 0.03 \text{ V vs. RHE} \quad (3)$$

$$2CO_2 + 12e^- + 12H^+ \rightarrow C_2H_4 + 4H_2O \; E_0 = 0.08 \text{ V vs. RHE} \quad (4)$$

$$2CO_2 + 12e^- + 12H^+ \rightarrow CH_3CH_2OH + 3H_2O \; E_0 = 0.09 \text{ V vs. RHE} \quad (5)$$

$$3CO_2 + 18e^- + 18H^+ \rightarrow CH_3CH_2CH_2OH + 5H_2O \; E_0 = 0.21 \text{ V vs. RHE} \quad (6)$$

$$2H^+ + 2e^- \rightarrow H_2 \; E_0 = 0.00 \text{ V vs. RHE} \quad (7)$$

1.3 Copper catalysts for eCO2RR

The use of catalysts is essential to afford selectivity, lower overpotential and overcome kinetic limitations for these multi-carbon products.[33] Copper-based electrocatalysts have been studied extensively due to their appropriate binding energy and coordination to form multi-carbon products, such as ethylene, as reported first in literature by Hori.[34] Copper is the only metal that is capable of the selectivity to multi-carbon products.[35]

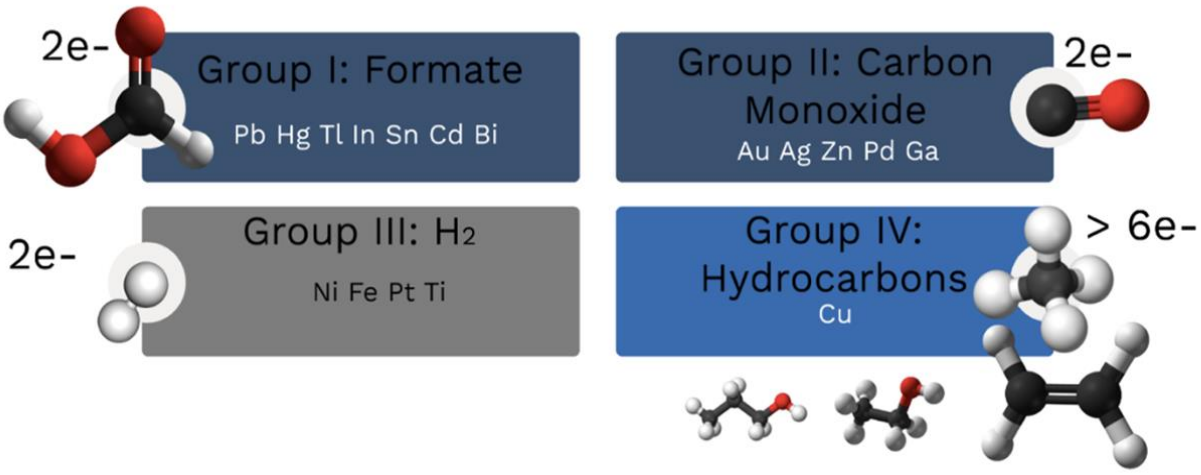

Figure 1-3 Electrocatalytic metals grouped by the main product evolved during eCO2RR.

However, many barriers remain; the copper catalysts are not selective to one product, HER occurs still, the overpotential required is high and kinetically the process is slow. Research has focused on morphology, particle size, grain boundaries of copper to address the current limitations for eCO2RR.[36–39]

1.3.1 Oxide-derived copper

Oxide-derived Cu (OD Cu) represents a research avenue for copper-based electrocatalysts, offering unique catalytic environments with the potential to enhance catalytic activity towards multi-carbon products. For example, Mistry et al. treated Cu foils with oxygen plasma,

thereby creating a CuO_x layer rich in Cu^+. The presence of stable Cu^+ species has been shown to promote CO–CO dimerization, leading to enhanced selectivity towards C_2 products.[40]

The presence of residual subsurface oxygen has been demonstrated to alter the electronic structure of Cu, increasing its affinity for CO_2 and CO intermediates. For example, Ren et al. electrochemically deposited Cu_2O layers onto Cu, which underwent in situ reduction, achieving an FE of 38.79% for ethylene and 9.01% for ethanol at -0.99 V vs. RHE.[41]

The demonstration of low energy *CO dimerization was attributed to high grain boundary concentration.[42] OD Cu was found to be an effective catalyst for C2+ due to the high concentration of stepped surfaces and edges that are formed during the reduction to the active catalyst form during reduction. These sites have low coordination number and increase the *CO adsorption strength which enables the build-up of large coverage of CH_xO intermediates which can dimerise to C2+ products.[41]

OD-Cu interacts differently with alkali cations, which affects CO_2 adsorption and local pH balance, leading to better product selectivity. Li et al. annealed Cu foil to create a Cu_2O layer, achieving an FE of 46.7% for CO at -0.35 V vs. RHE. The annealing process led to the modification of Cu's surface interactions with the electrolyte, thereby enhancing CO selectivity over HER.[43]

1.3.2 Particle size effects for C2 selectivity

Research highlights the effects of nanoparticle size on CO_2 reduction performance, demonstrating that particle size directly influences the reactivity of catalyst materials. This influence arises from a significant increase in the surface to bulk atom ratio as particle size decreases,

leading to larger surface curvature, lower average coordination of surface atoms due to more undercoordinated sites[44], perturbed electronic structures, and oftentimes increased reactivity[45].

The impact of size-activity relation of Cu nanoparticles towards hydrocarbon selectivity of eCO2RR has been studied in narrow nanoparticle size distribution of 15 nm and less. Under 5 nm, the production rate towards hydrocarbons decreases whilst production rate towards carbon monoxide and hydrogen increase.[37] Furthermore, in multiple studies copper nanoparticles have been observed to aggregate[46] and become less well-defined in shape[47] under electrochemical conditions.

1.3.3 Surface facets

Cu(100) surfaces predominantly form ethylene (C_2H_4), along with smaller amounts of methane (CH_4), whereas Cu(110) and Cu(111) surfaces favour the formation of CH_4 with very limited amounts of C_2H_4.[48] This suggests that different crystal facets exhibit distinct catalytic activities and selectivities, likely due to variations in atomic arrangements and electronic structures that affect the adsorption and activation of reactants and intermediates.

Further investigation into the role of undercoordinated sites, such as steps and kinks, reveals their significant impact on product selectivity. Cu(100) surfaces with (111) or (110) steps have been linked to increased selectivity towards alcohols and a higher propensity for C_2H_4 formation over CH_4.[49,50] These structural features promote multicarbon product formation. This suggests that engineering Cu surfaces with an optimal arrangement of (100) facets and step sites could enhance selectivity towards desired C2+ products, such as ethylene and other oxygenated compounds.

1.3.4 Scaling relationship limitation

There is a linear relationship between the binding energy of different intermediates within a pathway to a product, hence reducing the binding energy of one intermediate reduces the binding energy of the other intermediate and then the intermediate desorbs and the pathway is no longer viable.[51] In the case of C2 products such as ethylene and ethanol, the $*C_2O_2$ and *OH binding energies have been used to explain the trend in the limiting potentials of nine transition metals for the reduction of carbon monoxide to ethylene or ethanol.[52]

As demonstrated in Figure 1-4a, the *COOH binding energy varies depending on the metal and that demonstrates a “volcano” relationship with the reduction rate for carbon monoxide. Whereby, the optimum binding energy for the highest rate of reaction (the top of the volcano) is a binding energy in the middle of the range of binding energies. In the case of the highest reduction rate to CO, Au has the optimum binding energy.

Multi-carbon products are formed from CO_2 that is reduced to CO* and then reduced further. However the optimum binding energy is different again for the rate-limiting step for the intermediate for multi-carbon products, as seen in Figure 1-4b where Cu sits atop the apex of the pyramid. Hence the difficulty of binding energy engineering for multi-carbon products when the metals with the optimum binding energy for the CO intermediate and the multi-carbon intermediates are not the same. However this observation could provide good evidence to pursuit bimetallic catalysts for multi-carbon products from CO_2 reduction.

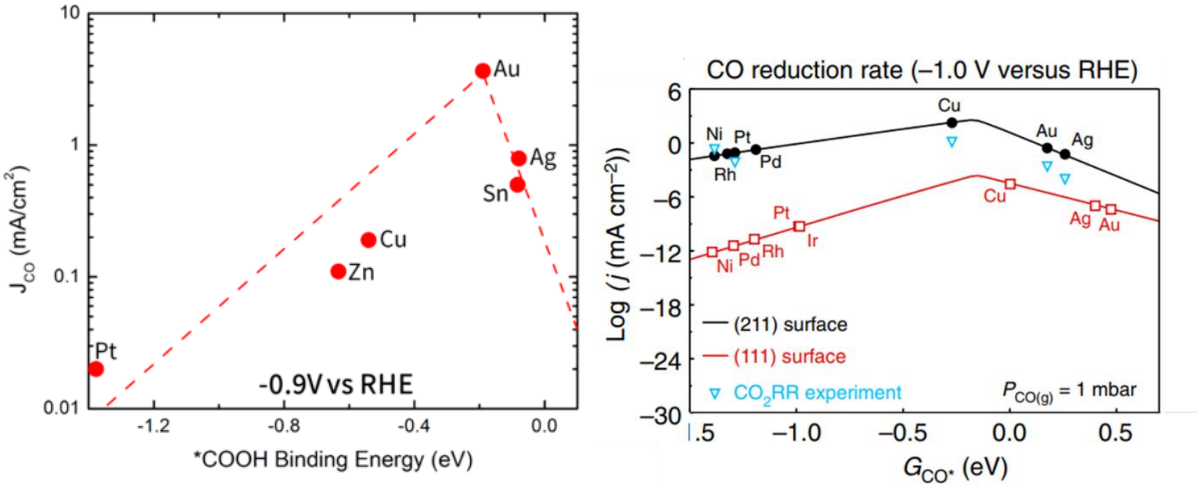

Figure 1-1-4 (a) Volcano plot of *COOH binding energy and the partial current density for carbon monoxide of polycrystalline transition metals at -0.9 V vs. RHE[14] (b) Activity volcano for flat(111) and stepped(211) transition metal surfaces as a function of CO binding energy.[54]

1.4 Bimetallic catalysts for eCO2RR

A bimetallic approach is one that aims to alter the binding energy of the surface atoms in order to alter the selectivity[55]. There is a lower reduction potential of CO_2 on Au compared with Cu[56], hence with the inclusion of gold there is the opportunity to have more facile CO_2 reduction to CO. Where Cu selectively produces hydrocarbons, Au has good selectivity towards CO[57]. Au demonstrates a lower overpotential to CO compared with Cu, hence shows a higher current density for the reaction. Importantly, CO is the key intermediate of multi-carbon products, and it could be transferred through a spill-over motion from Au to Cu, hence aiding facile carbon-carbon coupling.

The pathway to form multi-carbon products occurs via a carbon monoxide intermediate. Whilst the formation of a carbon monoxide product/intermediate occurs via a carboxyl intermediate (*COOH) through bonding of the catalyst surface to the carbon or oxygen atom of

the CO_2 molecule and proton and electron transfer. Norskov et al[53] proposed volcano plots of the partial current density of CO and the *COOH binding energy. Au is found to be at the top of apex of the pyramid showing that the *COOH binding energy to influence the activity towards carbon monoxide. In contrast, Cu is found to have a larger *COOH binding energy and lower carbon monoxide partial current density.

Whilst when considering the binding energy of the *CO intermediate, Cu is found to be at the apex of the pyramid of *C) binding energy and log (current) of CO_2 electroreduction. Furthermore, when plotting CO partial current density, Au and Ag have a lower partial current density due to a lower *CO coverage.

Much research has been focused on the experimental investigation of the effect of Cu-Au bimetallic catalysts on CO2 electroreduction. Several studies have investigated Au-Cu catalysts at low overpotentials and found that the inclusion of Cu can reduce the need for gold, a precious metal, while still maintaining high faradaic efficiencies for CO. Many different nanostructures of Au-Cu catalysts have been investigated; such as Au/Cu nanospheres[58], Au-Cu nanoparticles dispersed on multi-walled carbon nanotubes[59], nanoporous Au_3Cu alloy[60]. Nanostructuring of Au-Cu bimetallic catalysts was used as a tool to offset the loss of faradaic efficiency towards CO that occurs due to the partial replacement of gold with copper due to it being a precious metal. These studies all use Au-Cu to be selective towards carbon monoxide by optimising the *COOH intermediate and weakening the *CO adsorption through electronic modification by alloying. However none of them are selective towards multi-carbon products at the operational overpotential and experimental conditions of the CO_2RR.

One study set out to remove the impact of nanostructuring by synthesising planar uniform thin films of gold and copper alloys. Liu and et al. found that pure copper was found to be the most effective for C-C coupling but produced a broad distribution of products, such as ethylene, ethanol, carbon monoxide and methane. At low gold content, Au_1Cu_{99} still favoured C-C coupling but with reduced efficiency for ethylene and ethanol production. The gold reduced the binding strength of CO on the Cu surface, leading to CO production being favoured over C2+ products.[61]

Another key factor investigated was the impact of lattice strain that occurs as a result of alloying gold and copper in nanoparticles. Au-Cu nanoparticles demonstrated high faradaic efficiency for CO at low overpotentials, improving on the performance of both pure gold and copper. The lattice strain measured in the Au-Cu alloy nanoparticles alters the electronic structure which improves the activity and selectivity for CO production.[62]

Heterojunctions were concluded to be the defining factor for notable faradaic efficiency of ethanol at relatively low overpotential in neutral aqueous media (63.1% FE of CO at -0.76 V vs. RHE in 0.1 M $KHCO_3$). In the same study, AuCu alloy did not show selectivity towards ethanol in the same conditions. It is believed that there was selective activation of reaction intermediates at the interface between Au and Cu in the heterojunction, while the alloy exhibited broader product distributions, including less desired products like methane. The heterojunction's design ensures optimal electronic interaction between the two metals, making the catalyst more effective than a homogenous AuCu alloy where the unique electronic structures of each metal become averaged out.[63]

Alternatively, one study created a wrinkled morphology of gold film and deposited Cu nanoparticles and found it to show optimal selectivity towards ethylene and ethanol over a wrinkled copper film. This improvement is believed to be the result of tandem catalysis whereby gold primarily facilitates the CO_2 reduction to CO due to its ability to stabilise CO intermediates and enhance CO desorption. Then copper acts as the secondary catalytic site, promoting C-C coupling reaction producing C2+ products.[64]

Tandem catalysis is also referred to by a study whereby Au nanoparticles are evenly dispersed on Cu_2O nanowires. The Au component aid in CO formation and coverage on Cu, whilst also suppressing hydrogen evolution. The interaction between gold and copper can modify the electronic effect of the copper site to lower the hydrogen binding strength and make it less likely for copper to facilitate hydrogen evolution.[65]

Cu_2O nanocubes were decorated with Au nanoparticles in a study which highlighted that low Au loadings improve C-C coupling, while higher Au loadings primarily promote CO production and suppress C2+ formation. It was found that CuAu alloy formation occurs during the CO_2RR dynamically as a result of the reaction conditions.[66]

Structural variations have been explored for C2+ product selectivity, in the form of Au-Cu core-shell nanoparticles. Monzo et al. (2024) decorated a gold core with copper shells of varying thickness. The paper reports that 7-8 layers of copper on gold nanoparticles favoured the formation of ethylene whilst thicker copper layers led to higher selectivity for methane. In contrast to the tandem catalysis in the studies discussed above, the catalytic reactions are mostly limited to the copper shell. However, it is thought that when the copper shell is

relatively thin, intermediate products, such as CO, can diffuse through the copper surface to the gold core where CO desorption occurs more readily due to the lower binding energy of CO on gold compared to copper.[67]

In summary, research on Cu-Au bimetallic catalysts for CO_2 electroreduction highlights the promising potential of these materials to improve selectivity and efficiency in the production of valuable carbon-based products such as CO and C2+ compounds. Studies have shown that the incorporation of copper into gold catalysts can reduce the need for precious metals while maintaining high faradaic efficiencies for CO, particularly at low overpotentials. The various nanostructures, including nanoparticles, alloys and thin films, each offer unique advantages in terms of electronic interactions and lattice strain that can optimise catalyst performance. In addition, novel designs such as heterojunctions and tandem catalysis have shown improved selectivity for desired products such as ethanol and ethylene. These findings underscore the importance of structural and compositional engineering in developing efficient bimetallic catalysts for multi-carbon products.

1.4.1 Gas diffusion electrodes

A gas diffusion electrode (GDE) plays a valuable role in eCO2RR as it allows CO_2 to diffuse into the catalyst layer, as opposed to saturating the electrolyte with CO_2. Including the catalyst layer, GDE have 3 components; the catalyst layer, the microporous substrate and a microporous layer.[68] The macroporous layer is responsible for the mechanical strength and electrical contact between the electrode and the current collector, enables the transport of CO_2 gas through its porous network and can be coated with a hydrophobic polymer to ensure hydrophobicity. The role of the microporous layer is to increase the area of electrical contact

between the catalyst layer and the macroporous layer and to further enhance hydrophobicity. These two layers do not have a clear interface as the microporous layer is composed of carbon nanoparticles that are smaller than the macroporous layer, so some nanoparticles enter the macroporous layer and form an interstitial zone. Typically, these gas diffusion layers have been manufactured for the fuel cell industry and are therefore commercially available, but they typically degrade under eCO2RR conditions.[69] After exposure to the high current densities and alkali solute that the GDE is exposed to, the hydrophobic nature of the GDE prior to the reaction has become hydrophilic.

1.4.2 Stability issues

A stability issue of GDEs is the intrusion of electrolyte into the GDE which reduces the pore space available for CO_2 transport and hence reduces the product selectivity of carbonaceous products relative to the hydrogen evolution reaction[70]. It also increases the distance of diffusion of CO_2 through electrolyte which increases the probability that CO_2 will react with -OH to form carbonate or bicarbonate aqueous species. The solubility of these salts in aqueous electrolyte is low and hence in the eCO2RR gas diffusion conditions, where water evaporates these salts precipitate in the pores of the GDE. Due to their hygroscopic nature, they draw in electrolyte via capillary forces and increase electrolyte intrusion[71]. To counteract this detrimental effect, hydrophobic materials, such as PTFE, are sprayed onto carbon-based GDEs but over time this degrades under the cathodic current and furthermore, PTFE has unfavourably low conductivity and itself occupies pore space [70]. At present, this phenomenon is affecting the stability of the GDE, reducing the selectivity of the reaction and hence there is opportunity to engineer solutions to prevent the flooding of the gas diffusion electrode.

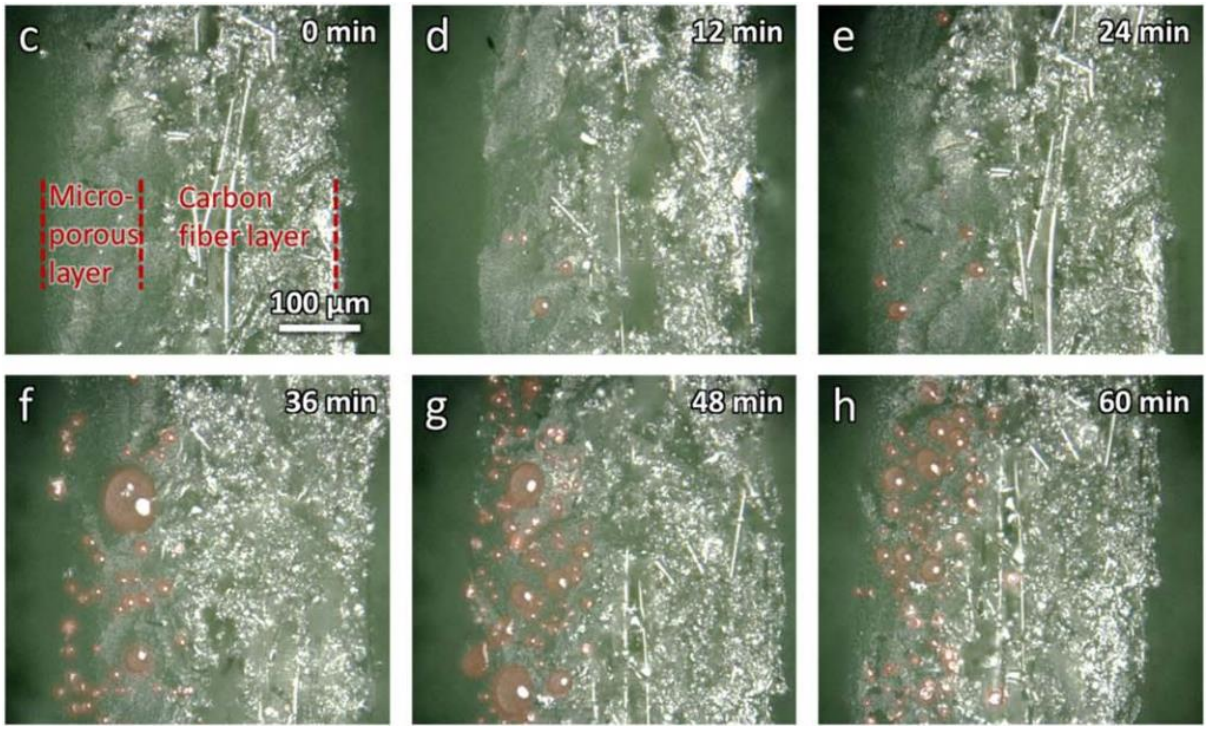

Figure 1-5 Optical microscope images of a gas diffusion layer at different points throughout the reaction.[72]

1.4.3 Additives in catalyst layer

Existing efforts to reduce flooding through the use of additives in the catalyst layer have included functionalising carbon black with fluorine-terminating molecules[73], incorporating PTFE nanoparticles into the catalyst layer[74–76] and the use of hydrophobized nanofibers[77]. As a supplementary approach, there has been work to fabricate GDEs that outperform commercially available GDEs, for example the use of PTFE binders on a carbon fibre skeleton with the adhesion of a PTFE macroporous layer which was found to operate for 103h (16 times longer than a commercial GDE)[78]. However, it has been suggested by one group that the traditional GDE design 'may not be resistant to flooding during CO_2 reduction'[72] and hence other groups have redesigned the GDE entirely, such as the use of a completely non-conductive GDE combined with a network of silver wires as the catalyst layer [79].

1.4.4 Characterisation of Electrode Flooding

Different characterisation tools are available to study electrode flooding in fuel cells and electrolysers. Various experimental techniques have been employed to investigate flooding mechanisms, enabling insight into spatial distribution, transport dynamics and electrochemical impact of water accumulation. Among the most widely used methods, electrochemical impedance spectroscopy (EIS) is a powerful diagnostic tool that enables the identification of flooding-related transport resistances by analysing frequency-dependent impedance responses. Ren et al (2019) used EIS to diagnose water failures in proton-exchange membrane fuel cells by analysing zero-phase ohmic resistance and fixed low-frequency impedance. The study showed that an increase in the low-frequency arc radius was an indicator of liquid water accumulation in the gas diffusion layer which leads to flooding. [80] Similarly, a drastic increases was observed in the low-frequency resistance in EIS measurements, indicating flooding in PEMFCs.[81,82] While EIS provides valuable in situ electrochemical insights, it lacks direct spatial resolution and requires complementary imaging techniques for a more comprehensive understanding of water accumulation.

In contrast, X-ray Tomographic Microscopy (XTM) allows researchers to capture real-time 3D images of liquid water distribution, providing a spatially resolved assessment of flooding dynamics. X-ray tomographic microscopy analysis was conducted on laser-performated GDLs in CO_2 electrolysis. The XTM visualised and quantified water transport mechanisms in the GDLs, distinguishing between water accumulation, redistribution and drainage pathways.[83]The same researchers then used XTM to study the performance of microporous layers within PEMFCs and found operando XTM imaging provided direct, three-dimensional visualisation

of how liquid water formed and moved within porous layers. The operando imaging enabled tracking of water accumulation and removal over time, particularly during the first minute of operation. XTM also found that at low humidity, water was primarily transported as vapour, whilst at high humidity and current density, liquid water accumulation increased at the catalyst layer / microporous layer interface and in the gas diffusion layer.[84]

In addition to EIS and XTM, other techniques such as neutron imaging, energy dispersive X-ray spectroscopy (EDX) and inductively coupled plasma mass spectroscopy (ICP-MS) have been employed to investigate flooding phenomena. EDX and ICP-MS provide chemical insights into electrolyte retention and ion migration associated with flooding events. Kong et al. 2022 found cracks in the MPL played a key role in electrolyte management, preventing flooding-related performance degradation in GDEs used for CO_2 electrolysis. EDX provided qualitative insights into potassium distribution, confirming flooding severity in non-cracked GDEs and effective drainage through cracks. ICP-MS quantitatively assessed electrolyte retention, demonstrating that higher crack density correlated with reduced flooding effects.[85]

Electrode flooding remains a key challenge in fuel cells and electrolysers, with various techniques used to characterize water accumulation and transport. EIS identifies flooding-related transport resistances, while XTM provides real-time 3D visualization of water distribution. EDX and ICP-MS further reveal how structural modifications, such as cracks in the microporous layer, impact water retention.

1.4.5 Catalyst engineering

A different approach towards tuning hydrophobicity in the GDE is through modifications to the catalyst species, for example the engineering of hydrophobic needle structure of Cu[86].

One approach is the surface functionalisation of the catalyst: the surface of a Cu catalyst was modified with toluene molecules[87]. Through molecular dynamic (MD) simulations and DFT-based structure optimisation, the intermolecular spacing between the toluene molecules was calculated to be 5.1Å . This was believed to be the critical factor in creating a micro-channel between the catalyst surface and the bulk electrolyte to enable high CO_2 concentration and low electrolyte wetting. The use of polymer ligands grafted to the surface of Au NPs which was stated to promote water clustering and create a hydrophobic microenvironment that led to improvement in GDE performance[88].

1.5 Aim and Objectives

In the following, the aims and objectives of this research will be discussed.

1.5.1 Aims

The aim of this research is to understand the limits of selectivity and stability of heterogeneous electrocatalysts in gas diffusion electrodes for CO_2 electroreduction for multi-carbon products.

1.5.2 Objectives

(1) **Synthesize and Characterize Bimetallic Electrocatalysts:** Develop and optimize Au-Cu_2O bimetallic catalysts for gas diffusion electrodes, leveraging the synergistic effects observed between gold and copper oxide to enhance the selectivity towards ethylene, ethanol, and propanol production. Characterize the catalysts using a range of techniques, including scanning electron microscopy (SEM) and energy-dispersive X-ray spectroscopy

(EDXS), to understand the relationship between catalyst morphology, composition, and performance in CO_2 electroreduction. Test different deposition techniques of Au on Cu_2O to optimise CO selectivity.

(2) **Evaluate the Performance of Modified Gas Diffusion Electrodes:** Conduct comprehensive electrochemical testing of gas diffusion electrodes, modified with bimetallic catalysts and hydrophobic additives, in CO_2 electroreduction. Focus on measuring selectivity towards multi-carbon products, faradaic efficiency, and electrode stability over extended operational periods. Analyse the role of catalyst composition, electrode structure, and hydrophobicity in optimizing the performance and longevity of the electrodes.

(3) **Improve Electrode Hydrophobicity:** Incorporate hydrophobic materials, such as nanoporous carbon particles functionalized with polyfluoroaromatic compounds, into the gas diffusion electrodes to mitigate flooding and enhance CO_2 transport to the catalytic sites. Assess the durability of hydrophobicity under electrochemical conditions and its effect on the selectivity and stability of the CO_2 reduction process.

(4) **Investigate the Mechanisms of Enhanced Catalytic Selectivity:** Utilize the findings from catalytic performance evaluations to delve deeper into the mechanisms underlying the observed selectivity towards multi-carbon products. Study the interaction between gold and copper oxide in the bimetallic catalyst and the influence of hydrophobic additives on the microenvironment at the catalytic sites, contributing to a more nuanced understanding of CO_2 electroreduction pathways.

2

Fundamentals & Methods

In this Chapter, we will discuss the experimental setup as well as different techniques that were employed through the course of this thesis.

2.1.1 Equilibrium Electrochemistry

If there is an electrode and an electrolyte containing redox active species, then the electrode has a potential ϕ_m, as does the electrolyte, ϕ_s. Hence the difference between the ϕ_m and ϕ_s gives the potential difference $\Delta\phi_{m/s}$ across the electrode interface as shown in equation (2-1).

$$\Delta\phi_{m/s} = \phi_m - \phi_s \quad (2\text{-}1)$$

The equilibrium depends on the ratio of the activity of the oxidised and reduced species (α_{oxi} and α_{red}), which is proportional to the ratio between the concentrations $[oxi]$ and $[red]$. The equilibrium constant of the reaction is given in the following equation:

$$\mathrm{K} = \frac{\alpha_{oxi}}{\alpha_{red}} = \frac{[oxi]}{[red]} \quad (2\text{-}2)$$

The Gibbs free energy of a reaction describes the Gibbs free energy of a system, where R = gas constant, T = temperature (Kelvin), K = rate constant.

$$\Delta G = \Delta G^0 + RT \cdot \ln(K) \quad (2\text{-}3)$$

$$\Delta G = -z\mathrm{F}E \quad (2\text{-}4)$$

Nernst found that the equilibrium potential could be defined as follows:

$$\mathrm{E} = E^0 + \frac{RT}{zF} ln \frac{[O]}{[R]} \quad (2\text{-}5)$$

Measurement of the working potential requires the use of a third electrode to define the potential difference between the electrode and the electrolyte, rather than measuring the potential difference between the working electrode - electrolyte and counter electrode - electrolyte potentials. The reference electrode possesses a constant and defined potential against which the working electrode can be measured. The electrochemical scale uses the water reduction reaction under standard conditions (pressure H_2 = 1 bar, pH = 0, $\alpha(H^+)$ = 1).

2.1.2 Interfacial Electron Transfer

Before a redox reaction of a redox active species can take place at an electrode, several processes must take place. The redox species must diffuse from the bulk electrolyte to the surface, which is governed by mass transport. Potential chemical reactions such as protonisation, dimerisation or catalytic decomposition can then take place. The reaction is then adsorbed onto the electrode and the redox reaction can occur. A reverse pattern of events can then occur for the redox species post-electro redox event, where the species desorbs, becomes available for chemical reactions and diffuses back into the bulk. The electrochemical rate is

determined by the slowest step of the above processes, which is referred to as the rate-determining step.

The term mass transport limited is used to describe an electrochemical reaction where the rate determining step is the movement of species from the bulk to the surface or vice versa. When mass transport is faster than electron transfer, and electron transfer is the rate determining step, the reaction is described as electron transfer limited.

The current associated with the process is an indicator of the reaction rate and this can be estimated using the equation (2-6) where i = current density, k = rate constant, $\left[C_{surf}\right]$ = concentration of species at the surface, z = number of electrons transferred per redox reaction and F = Faraday's constant.

$$i = k\left[C_{surf}\right] \cdot zF \qquad (2\text{-}6)$$

This net current can be divided into its contributing oxidation and reduction currents, defined as the oxidation current and the reduction current. At equilibrium, the current contributions are equal and therefore the potential difference between the electrolyte and the electrode is 0 V. The potential difference of an electrochemical system in a cell when no external potential bias is applied is called the open circuit voltage.

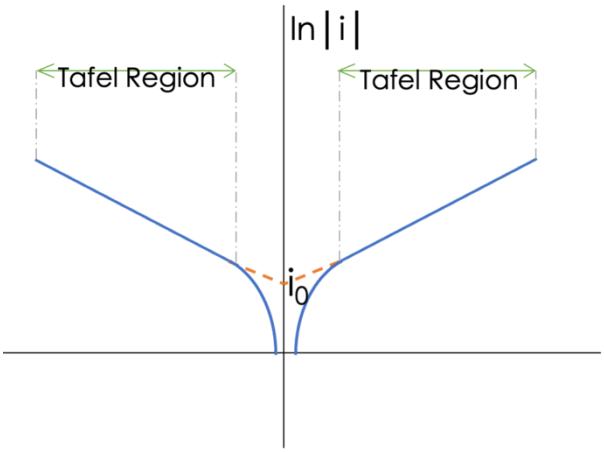

Figure 2-1 An example tafel plot, showing both oxidative and reductive tavel regions and the exchange current density i_0 when a = 0.5.

2.1.3 Butler-Volmer equation

The Butler-Volmer equation describes the relationship that can be derived between the natural logarithm of the current and the overpotential. Overpotential is the difference between the reduction potential and the potential at which the redox occurs. This derivation is found by taking the net current flow as given by:

$$i = FA(k_0[R]_0 - k_0[O]_0) \quad (2\text{-}7)$$

$$k_{red} = k^{\circ}\exp\left(\frac{-\alpha F\eta}{RT}\right) \quad (2\text{-}8)$$

$$k_{ox} = k^{\circ}\exp\left(\frac{(1-\alpha)F\eta}{RT}\right) \quad (2\text{-}9)$$

$$\eta = \frac{RT}{\alpha F}\ln i_0 - \frac{RT}{\alpha F}\ln i \quad (2\text{-}10)$$

where α = transfer coefficient and i_0 is the exchange current.

The Tafel plot is when the natural logarithm of the current is plotted against the overpotential, as shown in Figure 2-1. In the linear regions of the plot, only the cathodic or anodic process is responsible for the current because the overpotential is far from the equilibrium potential. The region between the two regions of the graph is where the current has contributions from both the anodic and cathodic current. By rearranging equation (2-10) above, the slope of the Tafel plot can be used to find the value of α.

2.1.4 Mass transport and diffusion layers

In Section 2.1.2, the kinetics of the reaction was discussed as being determined by the rate determining step, which could be mass transport or electron transfer in nature. In the case of rapid electron transfer, the study of mass transport effects provides insight into the reaction rate.

Different types of mass transport can occur and these include: diffusion, convection and migration.

Diffusion is the result of an increase in entropy, whereby areas of high particle concentration move to areas of low concentration to create a more homogeneous distribution. Furthermore, the rate of this process is determined by the difference between the high and low concentration at a given coordinate. This was mathematically defined by Fick for species "B" in the equation below:

$$\mathrm{j} = -D_B \frac{\partial [B]}{\partial x} \qquad (2\text{-}11)$$

where j = diffusion flux, [B] = concentration of B. D_B is a diffusion constant known as the diffusion coefficient, the value of which is specific to the identity of B.

Fick's second law of diffusion can be used to predict changes in the concentration of electro-active material near the surface of an electrode.[89]

$$\frac{\partial[B]}{\partial t} = D_B \left(\frac{\partial^2[B]}{\partial x^2}\right) \quad (2\text{-}12)$$

Convection is movement due to a mechanical force in a solution. One type of convection is due to thermal variation or density difference within the solution, both of which can be generated in situ as a result of the electrochemical reaction. The reaction may be exo- or endothermal and/or the redox product may have a different density to the reactant. Alternatively, convection can be externally controlled by gas bubbling, stirring or pumping. If this convection method follows a well-defined behaviour, then the flow can be described quantitatively, and mass transport can be predicted.

$$\frac{\partial[B]}{\partial t} = -v_x \left(\frac{\partial[B]}{\partial x}\right) \quad (2\text{-}13)$$

where v_x = velocity.

Migration is the term used to describe the movement of species due to electrostatic forces. Due to the presence of an electric field at the electrode/electrolyte interface, charged species in the interfacial region experience an electrostatic force that causes them to move either closer to or further away from the electrode/electrolyte interface.

$$j_m \propto -u[B]\frac{\partial \phi}{\partial x} \quad (2\text{-}14)$$

where j_m = migration flux, u = ionic mobility and the electric field, $\frac{\partial \phi}{\partial x}$.

2.1.5 Linear and cyclic voltammetry

Experimentally, lots of information can be obtained by perturbing an electrochemical system with an external bias. Voltametric methods use the application of a potential that is continuously changed in steps at a known rate and measure the current response of the system. This can be done in one direction, known as linear sweep voltammetry, starting at E_1 and ending at E_2 with a scan rate v_s and sweep time t.

In an electrochemical system with redox active species, current is measured when the potential sweep reaches a potential high enough to induce electron transfer. As the magnitude of E increases during the sweep, the oxidation rate constant, k_{ox}, increases and hence the current increases exponentially with potential. However, at a certain E, the current reaches a maximum and then decreases. This is due to the dependence of the current at this point on $[A_0]$, the surface concentration of the reactant, A_0, which is being consumed at a rate greater than that which can be replenished by mass transport from the bulk to the surface. The maximum current is called the peak current, i_p. The current after i_p is proportional to the mass transport of A_0 in the depletion zone around the electrode.

Regarding the potential position of E_p, for reversible reactions the potential position is independent of the sweep rate. Whereas for irreversible reactions the E_p shifts.

The magnitude of i_p increases with scan rate for both reversible and irreversible cases. If the scan rate is higher than there is less electrolysis over time, the depletion of A near the electrode is reduced, resulting in a thinner diffusion layer and a steeper concentration gradient. The higher flux results in a higher i_p.

In cyclic voltammetry, the potential is scanned in both directions, resulting in a triangular waveform of the potential. The reverse scan causes the potential to approach the equilibrium potential of the redox species and, due to the high concentration of product from the forward scan, the current increases in the opposite direction. The kinetics for the reverse scan redox become more favourable as the potential becomes more positive.

The position of the $E_{p,red}$ and $E_{p,ox}$ are separated by 59 mV at 25°C and are independent of the scan rate.

2.1.6 Chrono- Methods

Chronoampemetric electrolysis is carried out by applying a constant potential against a set time at which the current is measured. When the potential is increased to a value at which electrolysis occurs, a large current is detected over time due to the lack of concentration depletion. Depletion occurs over time.

In the absence of redox-active species when studying chargeable materials, an instantaneous large current spike is observed when a chronoamperometric potential is applied. This is due to the movement of ions in the solution responding to the shift in the electric field, which in turn causes a shift in the electric field in the electrode.

2.2 Product Analysis Techniques

2.2.1 Gas chromatography (GC)

Gas chromatography is a method of identifying gases and quantifying their concentration in a sample. GC consists of a column lined with a material called the stationary phase. As the

mobile phase moves through the column, it interacts differently with the stationary phase depending on its affinity for the material, so that different gases pass through the column at different times. A gas arrives at the detector at a certain time after the start of injection, known as the elution time. At the detector the amount of gas present produces a signal proportional to the size of the peak area. A calibration curve for the GC can be established by injecting samples of different known concentrations and plotting the resulting peak area against concentration. The slope of this calibration curve then allows an unknown gas concentration to be calculated from its peak area.

2.2.2 Gas chromatography for liquid products

Liquid products can also be analysed by gas chromatography, but the raw sample is in liquid rather than gas form. It is therefore vaporised in the gas chromatography equipment so that it is in the same state as the carrier gas and both the vaporised sample and the carrier gas can move together through the column as a mobile phase.

2.2.3 Ion chromatography (IC)

Ion chromatography uses the same physical technique as gas chromatography but separates and quantifies ions in solution. The mobile phase in ion chromatography is the sample containing ions or polar molecules and aqueous/organic media, which is pumped through a column containing the stationary phase. The different affinities of the ions for the stationary phase result in separation. The detector records the conductivity associated with the eluted sample to produce a quantifiable peak area. Similar to GC, a calibration curve can be generated. Due to the various techniques used to reduce the effects of pH and the result of dissolved carbon dioxide in the eluent, there is often a deviation in the baseline for peaks.

Therefore, it is usually more appropriate to apply a quadratic curve fit to the calibration curve data due to the above-mentioned effects that cause deviation from a linear trend.

2.3 Catalyst preparation

2.3.1 Copper microparticle synthesis

Cu_2O microparticles were synthesised by a hydrothermal method and chemical reduction of copper acetate (Sigma Aldrich, 99.8%) with glucose (anhydrous, Sigma Aldrich) as previously published.[90] The ratio of water (ml): ethanol (ml): ethylene glycol (ml) used was 10:50:20.

The microparticles were washed in ethanol and water before separation by centrifugation (6000rpm, 30min). The particles were then dried under Schlenk conditions at 80°C for 48 h.

A more detailed description of the synthesis is given below as the reaction conditions were found to impact particle size. In a contained round bottom flask, the solution did not have as much contact with air as in an open beaker. In a round bottom flask, evidence of Cu nanoparticles were observed. The sample exhibited a plasmon resonance peak associated with Cu nanoparticles when studied with UV-Vis spectroscopy. The aim of the synthesis was to produce Cu_2O microparticles, hence the synthesis conditions were altered to achieve this, as described below.

2 ml of DI water, 20 ml of ethylene glycol and 50 ml of ethanol were mixed with a stirrer bar in an open 150 ml beaker to form a solution. (Initially only 2 ml of water was added, so that the reagents (potassium hydroxide and glucose) could be added as aqueous solutions to minimise large concentration gradients of reagents). 1.0 g of copper acetate hydrate was added

to this solution. Stirring continued but no heat was used. It was found that the copper acetate could be slow to dissolve in this solution, hence the stirring could be left for up to an hour. A watch glass was used to cover the beaker during this time with the aim to minimise any evaporation. Once the copper acetate was fully dissolved, the watch glass was removed the solution was then heated to 70°C whilst stirring continued. Once the solution had reached 70°C, then 5 ml of 7M aqueous NaOH solution was added drop-wise. Then 3 ml of 2.22 M D-glucose aqueous solution was added. Both these solutions had previously been sonicated to encourage their total dissolution in water. The solution is then left to heat at 70°C whilst continuing to stir for 30 minutes. After 30 minutes, the hot plate is turned off and the reaction beaker is left to cool on top of the hot plate. After that the Cu_2O is washed as mentioned above.

2.3.2 Colloid imprinted carbon synthesis via templating

Carbon pitch was cryogenically ball milled for 30 min and cooled with dry ice. Colloidal silica (80 nm) was then dried in an oven at 80° for 12 h. The carbon pitch and dried silica were then ball milled together. The mixture was then heated at ramped intervals to imprint the carbon around the silica and to carbonise the carbon species within the mixture. The resulting mixture was removed by refluxing with 1M KOH to dissolve the silica. The solid imprinted carbon was then washed.

2.3.3 Functionalisation of nanoporous carbon particles with pentafluorophenyl moieties

Colloid imprinted carbon (CIC) was functionalised with pentafluoroaniline to form a monolayer of pentafluorophenyl carbon. 1.0 g CIC-85 powder (CIC powder with 85 nm pore size),

6.0 g pentafluoroaniline were mixed in 250 ml of acetonitrile under N_2 and then 3.9 mg amyl nitrite was added dropwise.

Glassware (round bottom flask(rbf), stirrer bar and bottom of condenser) was cleaned with piranha solution. The CIC and pentafluoroaniline were added to the rbf which was sealed with a septum. An outlet needle was inserted into the septum before inserting the gas flow of N_2. Then acetonitrile was added to the rbf. The reaction mixture was then sonicated to prevent agglomeration by sitting the base of the rbf in a sonicator. The amyl nitrate was then added dropwise with syringe through the septum.

A reflux system was then set-up, using a bubbler connected to the outlet to prevent any back suction when the system cools down after the reflux to maintain an oxygen and moisture-free environment. The reaction mixture was then refluxed for 24 hours under N_2 environment at 82°C.

After the reflux, the resulting solid is filtered off with vacuum. Polyethersulfone filter paper (Sartorius) of 0.2 µm. The filtered solid was washed four times with acetonitrile.

For the final washing, Soxhlet extraction was performed with acetonitrile. The solid was folded tightly into 24 cm filter paper (Whatman, Type 5) and tucked into a cellulose thimble that was then repeatedly washed with acetonitrile.

The powder was then dried in an oven in air at 50°C.The filter paper from the Soxhlet was sonicated in acetonitrile to remove any further solid from the paper.

BET measurements, performed by Lee Stevens at Nottingham University, were used to measure the difference in surface area per gram of the material pre and post functionalisation. The results were shown in the table below It was found that the BET specific area decreased by 10.4%. In prior work, the Birss group found that their CIC-85 underwent a specific area reduction of 12.6%.[91]

Table 2 Surface area characteristic of as-synthesised and functionalised CIC-85 powder.

Sample	BET specific area (m^2/g)
CIC-85	148.5
CIC-85-PhF$_5$	133.0

2.3.4 Ink preparation

The gas diffusion electrodes (GDE) were prepared by spraying catalyst ink onto the gas diffusion layer (H2315 I2 C6, Freudenberg). The catalyst ink was prepared by dispersing 10 mg cm^{-2} Cu_2O microparticles in 100 µL cm^{-2} isopropanol and 17 µL cm^{-2} (Nafion suspension, 5 wt%, Sigma Aldrich). The ink was sonicated for 20 min when the microparticles are added to isopropanol and for a further 15 min when the Nafion binder is added.

2.4 Catalyst Characterization

2.4.1 Scanning electron microscopy (SEM) and energy dispersive X-ray spectrometry (EDXS)

The SEM is a technique used to produce magnified images of a material. This is achieved by scanning a beam of electrons across the surface of a material and recording the emission of high energy backscattered electrons and low energy secondary electrons. By scanning and measuring the change in emitted electrons from a sample, the structure, morphology, composition and electronic information of a sample can be mapped onto an image.

Scanning electron microscopy is a technique that provides a higher resolution of a sample surface than an optical microscope because the wavelength of an electron accelerated below kV has a shorter wavelength than visible light. The Rayleigh criterion dictates a maximum resolution of

$$d_0 = 0.61\lambda/NA \qquad (2\text{-}15)$$

where d = minimum resolvable resolution, λ = wavelength of illumination, NA = *n* sin(α) is the numerical aperture[92]. Hence, the smaller the wavelength the smaller the minimum resolvable resolution will be. The wavelength of an electron accelerated at a high potential, e.g., 20 kV, is 9 picometres (although this is limited by spherical aberration).

The focused electron beam interacts with the sample. There are two types of electrons that can escape from the surface of the sample: backscattered electrons, which are high energy electrons, and secondary electrons, which are electrons with energies below ~ 20eV.

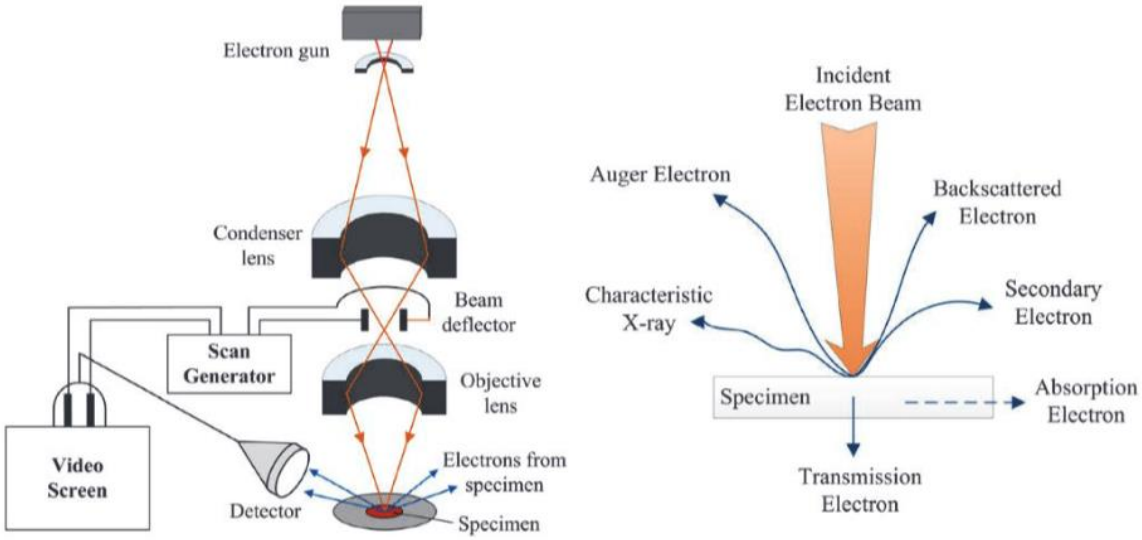

Figure 2-2. a) Scheme of SEM set-up b) Incident electron beam and its result on the sample.[93]

Backscattered Electron (BSE) is an elastic scattering event; therefore no energy is lost from the electron. The number of electrons backscattered increases with the average atomic number of the target, so an image produced using the BSE imaging mode will show the chemical contrast of the sample.[94]

Secondary electrons (SE) are produced by an inelastic event where the electron loses energy to valence electrons in the sample. Secondary electrons are low energy and must be generated close to the surface to escape. When using the SE imaging mode, changes in surface height due to topography are imaged as a raised surface due to a greater proportion of the electron beam interaction volume.

Chemical analysis can also be performed using SEM when incoming electrons remove a core electron from the atom, leaving a vacancy. The ionised atom can return to the ground state by emitting X-rays or Auger electrons. Since atomic energy levels are quantized, the X-ray energy can be used as a 'fingerprint' to detect different elemental ratios.[95]

2.4.2 Powder X-Ray Diffraction (PXRD)

X-ray diffraction uses the physical phenomenon of diffraction to produce a diffraction pattern that is unique to the crystal structure of a crystalline powder. X-rays interfere as they interact with the regular spacings between atoms, which are comparable in width to the wavelength of an x-ray.[96] In powder x-ray diffraction, specific lattice planes of the crystal produce corresponding cones of interference. The detector moves in an arc of 2θ relative to the powder and measures the intensity of the diffracted X-rays.[97] The intensity of the counts plotted against 2θ produces the diffraction pattern unique to the crystal structure of the powder. From the diffraction pattern, the peak position and peak intensities can be obtained, revealing the identity, phases and crystallite size of the crystalline powder.

2.4.3 Contact Angle Measurements

Contact angle measurements are a measure of the hydrophobicity of a surface by placing a drop of known volume on the surface of a material and using an infrared camera to take a photograph which is then analysed by software to calculate the left and right angles of the curve of the drop against the line of the surface. The angle depends on the hydrophobicity and roughness of the surface.[98] The more these characteristics of a material increase, the less of the droplet's surface area will touch the material, resulting in a more pronounced droplet 'standing off' the surface.

2.5 CO2 electrolysis set-up

2.5.1 Gas diffusion electrode cell design

The CO_2 electrolysis was conducted within a 3D printed acrylic cell as shown in Figure 2-3.

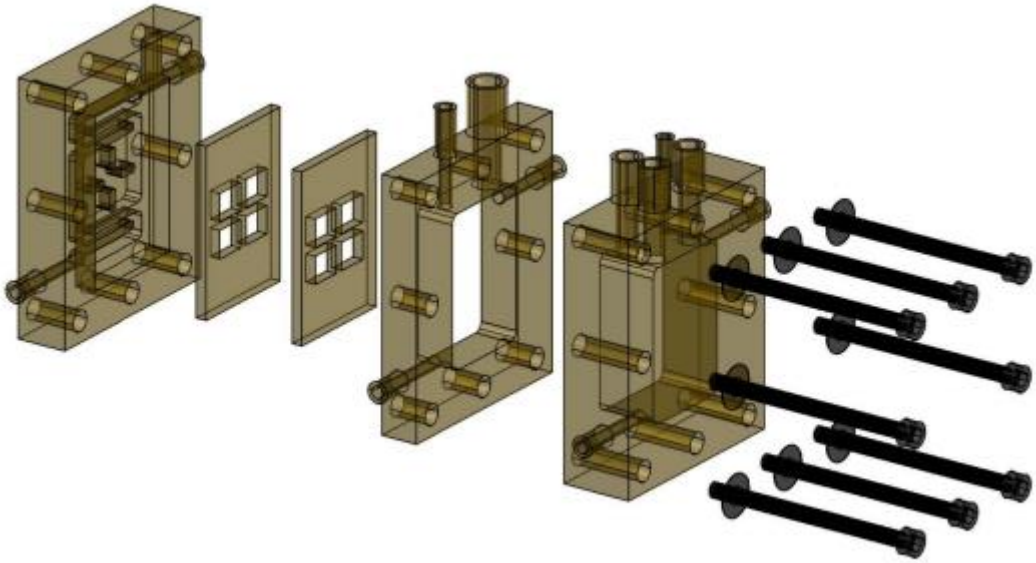

Figure 2-3 3D drawing of 3D printed acrylic pieces designed by Hang Xiang. [202]

2.5.2 CO_2 electrolysis reaction

The flow rate of CO_2 (BOC 99.99%) was controlled at 50 sccm by a digital flow meter (Bronkhorst EL-FLOW® Select Mass Flow Meter). 1M KOH and 5M KOH (Sigma Aldrich, 90% reagent grade) electrolyte was used for the catholyte and anolyte respectively. HgO / Hg (RE-61AP ,

BASI, 1M KOH) was used as the reference electrode and platinum plated titanium mesh with a dimension of 4 cm^2 was used as the anode. Before each eCO2RR, the cell parts were soaked in 0.5M HCl solution and then cleaned with DI water.

The anode and cathode chamber were separated by a cation exchange membrane (Fumapem F-950 , Fuel Cell Store) which was activated by putting the membrane sample in an aqueous 5 vol% H_2SO_4 solution at 80°C for at least 12 hours. Before rinsing with demineralised water.

All electrochemical reactions and measurements were performed using a potentiostat (Metrohm Autolab PGSTAT128N).

A peristaltic pump (120U/DM2, Watson Marlow) was used to circulate fresh catholyte from a reservoir to maintain local pH. The liquid product sample was removed from the reservoir. The flow rate was controlled at 10 ml min^{-1} during the reaction. The total catholyte volume was 35 ml. The anolyte was not circulated.

3

Characterization of Hierarchically Structured Cu_2O Microparticles with Gold Deposition

Ella Fidment, Eileen Yu, Elizabeth Gibson

The BET surface area measurements were performed by Lee Stevens.

Abstract

This chapter covers detailed characterization of Cu_2O microparticles for electrochemical CO_2 reduction reaction (eCO2RR), with an emphasis on modifying Cu_2O through gold deposition.

Nanocrystalline Cu_2O microparticles were synthesised as the catalytically active material for CO_2 electroreduction and deposited via spray onto carbon paper to create the gas diffusion electrode (GDE). The crystallite size of the Cu_2O was found to average at 7 nm using the Sherrer equation. Novel research was conducted with different deposition techniques (electro-, photo-) to create a bimetallic Au/Cu_2O GDE. Characterisation methods (XRD, SEM, EDX) have been employed to observe the influence of the deposition conditions on the bimetallic materials. The overpotential of the $AuCu_2O$ in CO_2 saturated 1M KOH electrolyte was observed to be reduced by ~50 mV with respect to Cu_2O.

3.1 Introduction

Copper oxide (Cu_2O) microparticles deposited onto gas diffusion electrodes were investigated herein for electrocatalytic CO_2 reduction, either as synthesized or modified with gold deposition. A structural and electrochemical analysis of the synthesized Cu_2O microparticles was first performed. Subsequently, several different gold deposition techniques (photodeposition, electrodeposition, galvanostatic exchange) were investigated to attempt to optimize the synthesis routine. The amount of product and selectivity of the catalyst were then quantified to obtain a better understanding of how such Cu/Au bimetallic catalysts could present a viable strategy for efficient and selective long-chain carbon product electrocatalysis.

3.2 Results and Discussion

Cuprous oxide microparticles were synthesized by a wet chemical synthesis method and deposited onto a gas diffusion electrode as discussed in Section 2.3. Briefly, microparticles were fabricated via a hydrothermal synthesis route whereby copper acetate was employed as the source of copper and glucose functioned as the reducing agent as presented in literature[90] and deposited onto a GDE via spray deposition. Subsequently, a structural characterization was first performed to ensure successful synthesis, and then the electrocatalytic performance for both Cu_2O and Au-modified Cu_2O catalysts was evaluated. Details on the synthesis of both Cu_2O and the Au-modified species are given in Section 3.4.

3.2.1 Cu_2O catalyst characterisation

The following section describes the benchmark characterisation of the Cu_2O electrocatalysts that will enable comparison for gold modified Cu_2O samples' characterisation in Section 3.2.2.2.

3.2.1.1 Structural characterization of Cu_2O.

Following the synthesis of cuprous oxide microparticles, powder x-ray diffraction (PXRD) measurements were performed. The resulting diffractogram is shown in **Error! Reference source not found.**.

Several distinct peaks are visible that describe the different crystal lattices of the Cu_2O microparticles (110, 111, 200, 220, 311). The diffraction pattern 2θ = 29.8°, 36.7°, 42.5°, 61.7° correspond to the (110), (111), (200) and (220) planes, respectively, for Cu_2O (ICDD file no. 96-900-7498). Only cuprite material was detected by the PXRD and no other Cu species, such as metallic or Cu(II) oxide was detected.

The full width at half maximum (FWHM) of the peaks were large and hence it was believed the Cu_2O particles could be nanocrystalline. To confirm this, the Scherrer equation was used to calculate crystallite size of the Cu_2O particles. The 3 most intense peaks were chosen, and the crystallite size was calculated via:

$$G_s = \frac{0.94 \times \lambda}{\beta \cos\theta} \quad (3\text{-}1)$$

where λ represents wavelength of X-ray radiation, G_s represents the grain size, θ is the angle of diffraction and β is the full width half maximum.23 The result of the calculation is given in Table 3-1 below.

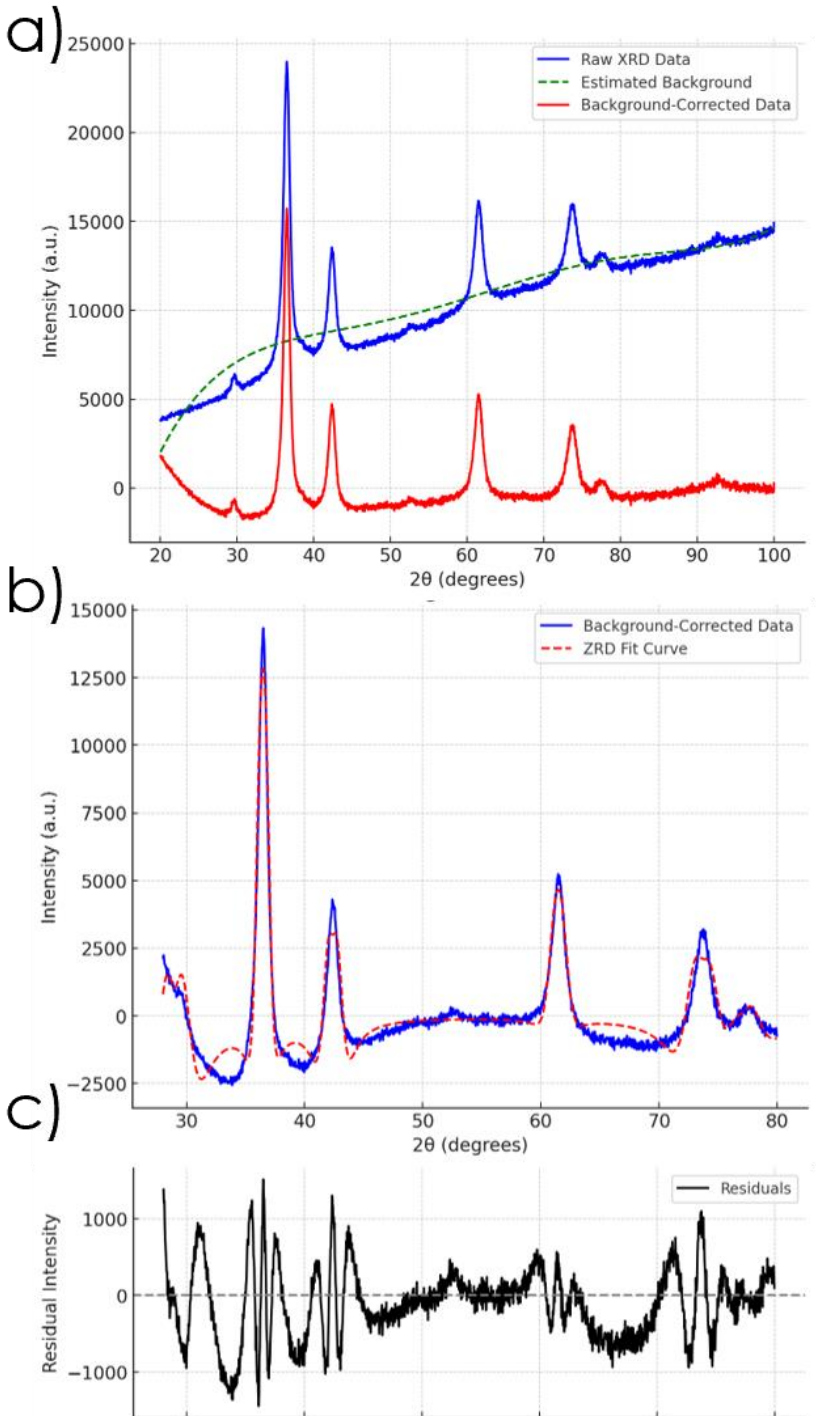

Figure 3-1a) The raw XRD data (blue line) with an estimated background (green dashed line) and the resulting background-corrected data (red line). (b) Background-corrected data (blue line) fitted with the XRD model curve (red dashed line), showing the alignment of the experimental peaks with the fitted model.(c) Residual plot indicating the difference between the background-corrected data and the model fit, highlighting deviations and noise in the fit.The residuals show some degree of periodicity, particularly around certain 2θ values.

Table 3-1: Peak properties of selected peaks of the PXRD measurement of Cu_2O microparticles. The respective diffractogram is shown in Figure 3-1. The FWHM standard used was the (111) peak of a silicon standard.

Peaks phases	Peak Position (°2θ)	FWHM of Cu_2O peaks °2θ	FWHM of Standard (as °2θ)	FWHM of Cu_2O standard (as °2θ)	Size (nm)
1 1 1	36.45	1.086	0.1335	0.9525	8.79
0 2 0	42.4	1.14	0.1335	1.006	8.47
0 2 2	61.44	1.47	0.1335	1.337	6.92

From calculations of the three peaks in Table 3-1, the crystallite size was estimated to range in size from 6.92 to 8.79 nm. This is within the range of the crystallite size of reported

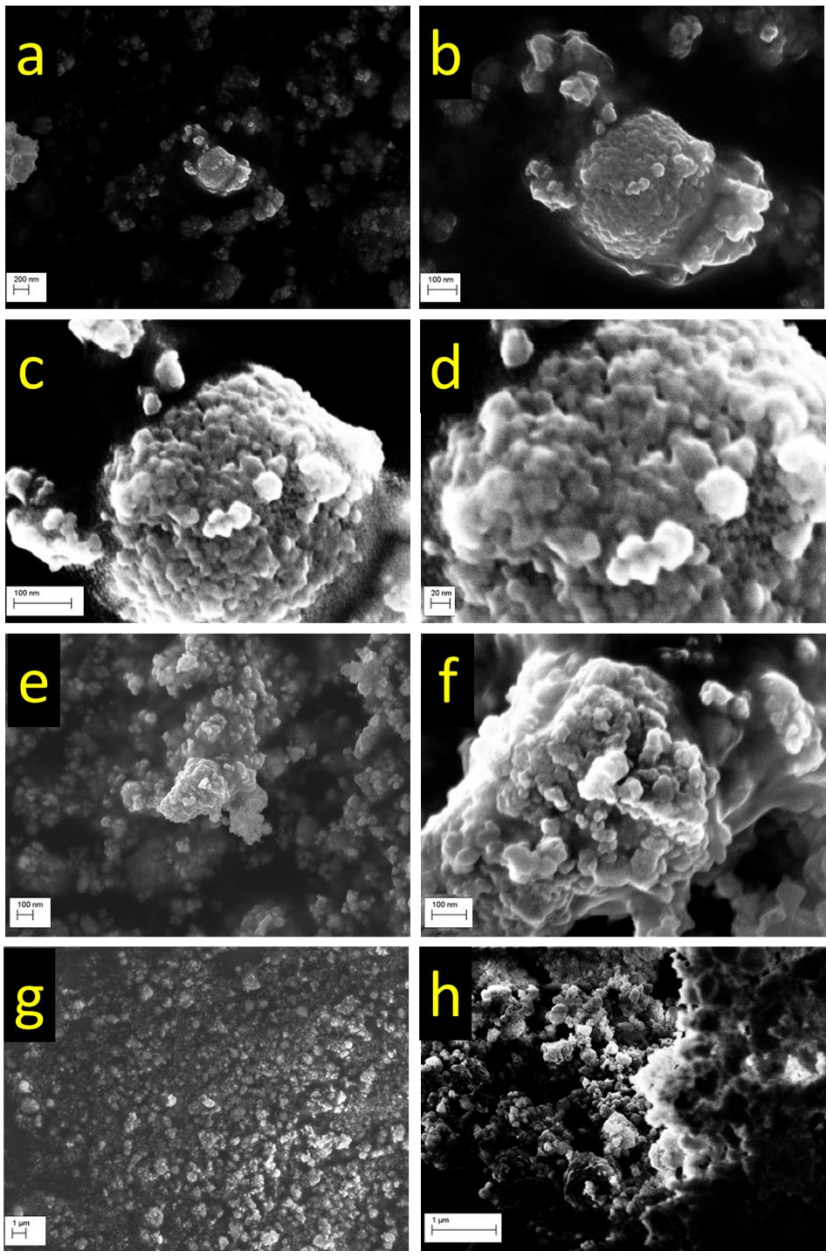

Figure 3-2. SEM images of Cu_2O powder at different magnifications. The degree of magnification is shown at the bottom left. All images are acquired with the InLens detector. (a) A single Cu_2O micro-particle. (b-d) The Cu_2O microparticle shown in (a) at increasing magnifications. Particle ensemble of Cu_2O microparticles. The structure of the particle becomes evident, indicating that the particle consists of an agglomeration of smaller particles. **(e-f)** Particle agglomerates on a larger scale and **(g-h)** particle ensemble of Cu_2O microparticles.

literature. [90] From this analysis, it suggests that the Cu_2O microparticles can be classed as nanocrystalline. [100] Previous literature states that nanocrystalline materials have a high

volume of grain boundaries compared to polycrystalline materials and hence the properties of a nanocrystalline material can vary from that of a polycrystalline material. [101]

To study the shape, size and morphology of the synthesised Cu_2O microparticles, scanning electron microscopy (SEM) was employed. Synthesised Cu_2O powder was loaded onto carbon tape and the results of the SEM study are shown in Figure 3-2. In Figure 3-2 a, in the centre of the SEM image is a single particle of Cu_2O. It is semi-spherical in shape and has a diameter of approximately 700 nm. At the highest magnification in Figure 3-2 d, the particle surface is observed to be porous and uneven. There are multiple holes visible on the surface of the particle all less than 20 nm in width. The SEM images in Figure 3-2 c-d illustrates that the 700 nm particle resembles smaller individual particles that have agglomerated to form the larger particle. Furthermore, distinct and grouped nanoparticles can be seen attached to the surface of the significantly larger microparticle, creating a rough and highly decorated particle. Figure 3-2 e and 3-2 f are SEM images of more amorphously shaped particles that also exhibit the signs of agglomeration. Furthermore, voids are visible within the particle, increasing overall surface area. In Figure 3-2g, a field of particles can be observed at a magnification on the

order of micrometres. In this image, the particle morphology is approximately consistent through all particles. In Figure 3-2h the SEM exhibits how particles cluster as a powder.

Note that it is difficult to extract an average particle size from SEM since only a few individual particles are studied. Additionally, there could be a size bias towards larger particles due to SEM magnification limitations. Hence, the particles were also studied under a light microscope(Figure 3-3) to assess maximum particle size on larger length scale compared to SEM

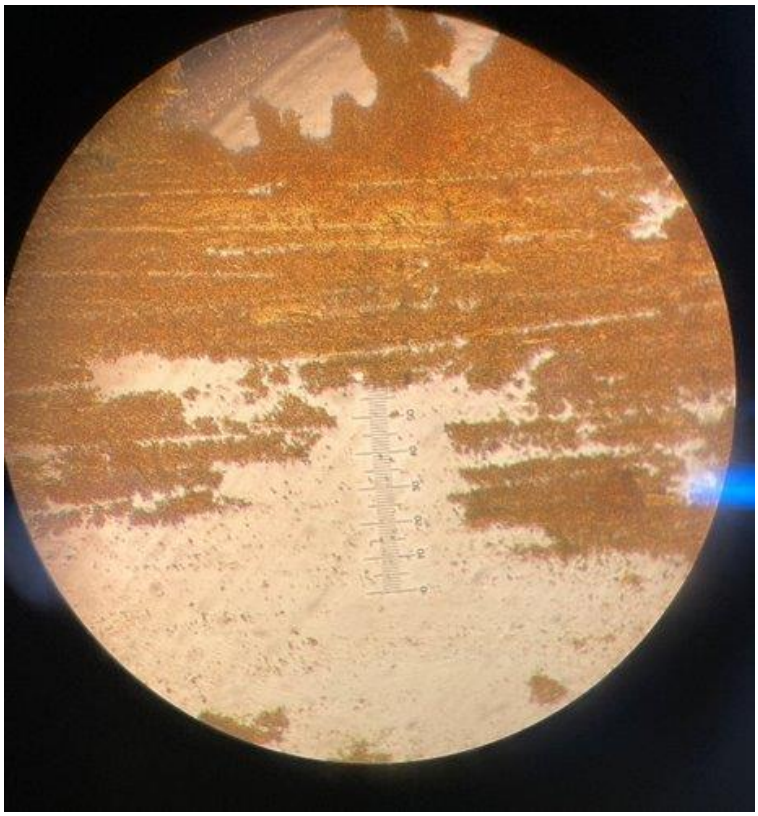

Figure 3-3. Image of Cu_2O powder performed with a light microscope. The scale bar in this image shows the micrometer scale in increments of 10 µm. While darker areas result from Cu_2O microparticles, brighter areas are caused by no particle coverage.

images in Figure 3-2 g. In Figure 3-3, ultimately, no particles larger than 10 micrometres were observed.

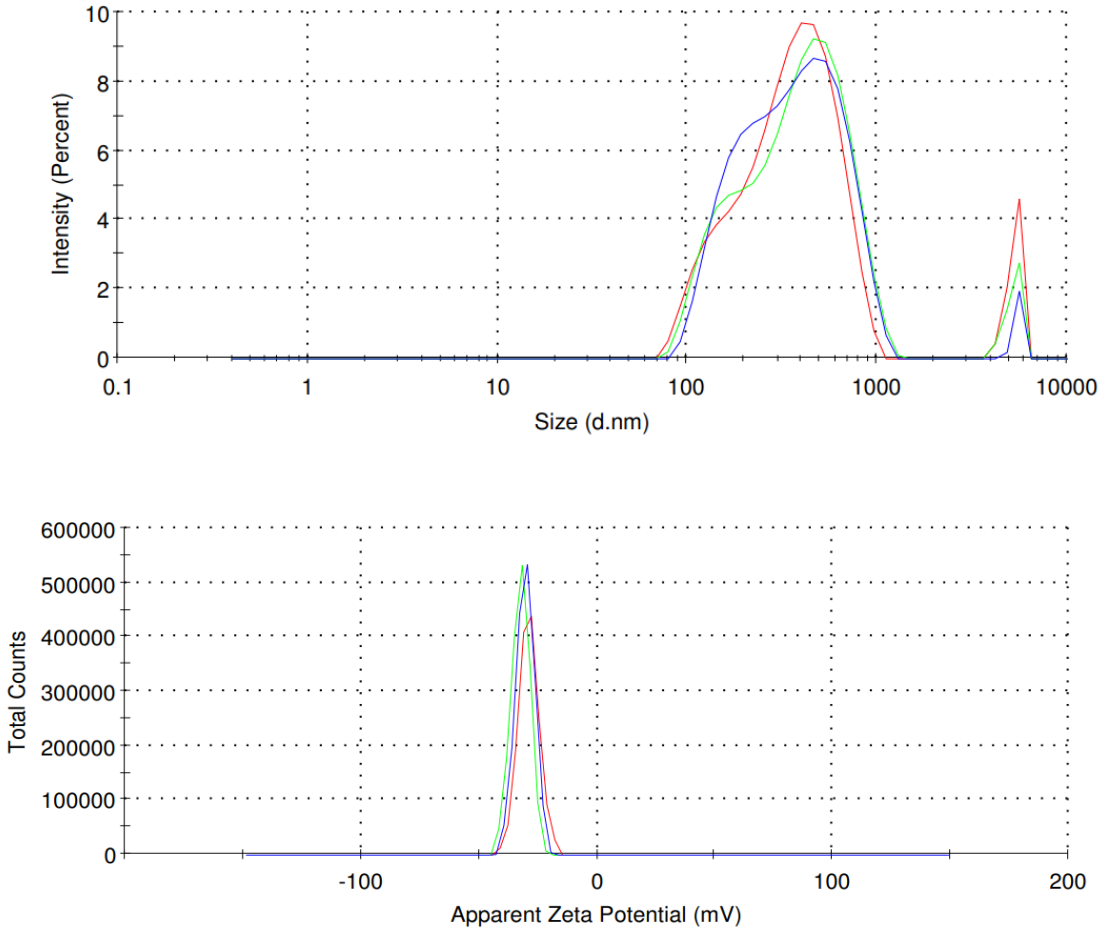

Figure 3-4. Dynamic light scattering (DLS) was used to calculate average particle density and zeta potential (mV) of Cu_2O in a water suspension. The red, green and blue line show the first, second and third run respectively of both the measurements. (a) Size distribution by intensity of Cu_2O microparticles measured in an suspension of water by dynamic light scattering (DLS). The statistical analysis is shown in the Table 3-2. (b) Zeta potential distribution of the Cu2O in water suspension.

Dynamic light scattering was used to determine a quantitative assessment of particle size. The measurements shown in Figure 3-4 revealed that there is not a continuous size distribution of particles, but two discrete peaks as shown in Figure 3-4a. In this figure, the peak with the greatest intensity that represents most of the particles shows a distribution of particle size from 70 nm to 1500 nm. Nanoparticles are classified as having a dimension between 1-100

nm whilst particles greater than 100 nm are classed as microparticles[102–104] and hence the classification of the Cu_2O material as microparticles in this study is in line with the findings of the DLS study. The peak with the smaller intensity shows that particle sizes of 2750 nm to 6500 nm were measured. No particles less than 70 nm were recorded; hence this suggests that a small percentage of the particles of Cu_2O are below 100 nm. Statistical analysis of the data, shown in Table 3-2, found that the average diameter of the particles of Peak 1 was 398.5 nm and is accountable for 98% of all particle intensity. Hence most of the particles are sub-micrometre particles. The average diameter of the particles within the size range of Peak 2 is 5500 nm, accounting for 2% of particle intensity. These particles were not observed when studying the Cu_2O material under the light microscope.

The surface area of the particles was measured by Brunauer-Emmett-Teller isoterms (BET). A BET surface of 217.7 m^2/g was measured, which is higher than values reported in literature of approximately 50 m^2/g.[90] Reason for this might be slightly different experimental conditions, e.g., the synthesis in this thesis was performed in contact with air, which could serve as an oxidizing agent. It is not clear in the literature report, whether the synthesis was performed in inert gas conditions or in contact with air, or whether solvents were degassed.

Zeta potential was also measured for the Cu_2O microparticles with the purpose of identifying potential electrostatic interaction between the Cu_2O surface and reactant salts used for further modification, such as subsequent gold deposition with chloroplatinic acid ($HAuCl_4$) that will be discussed in detail in Section 3.2.2. It was found that the zeta potential of the Cu_2O microparticles was approximately -30.4 mV, which is close to the range of literature reports of zeta potentials for cupric oxide nanoparticles (ranging from -20.6 to -24.6 mV).[105,106]

Overall, the goal was to create a copper-based material that would be appropriate for electrocatalytic CO_2 reduction (eCO2RR). Microparticles was chosen as the target size particle as previous literature has found that Cu nanoparticles show an increase in selectivity towards carbon monoxide and hydrogen and decrease in selectivity to hydrocarbons as their size decreases from 15 nm to 2 nm. [37] Instead, the research approach utilised microparticles assembled by nanoparticles with nanocrystalline character. This led to the formation of a multi-scale structure of Cu_2O material where both favourable aspects of the nano- and micro- structure are present for electrocatalysis.

Table 3-2. Particle size average and standard deviation calculated by dynamic light scattering. The statistical analysis was conducted of the raw data shown in Figure 3-4.

	Average diameter (nm)	**% intensity**	**Standard deviation of diameter (nm)**
Peak 1	398.5	97.9	220.8
Peak 2	5493	2.1	214.2

Cu(I) was the target oxidation state of copper material as previous research found that oxide-derived copper electrocatalytic material was found to outperform metallic-origin copper in eCO2RR. [41,107] The above characterisation has identified the synthesised material as pure Cu_2O in the form of nanocrystalline microparticles.

3.2.1.2 Electrochemical characterization of Cu_2O.

Next, an electrochemical study was performed to characterise the properties of Cu_2O further and understand the ability of the material to perform electrocatalytic CO_2 reduction.

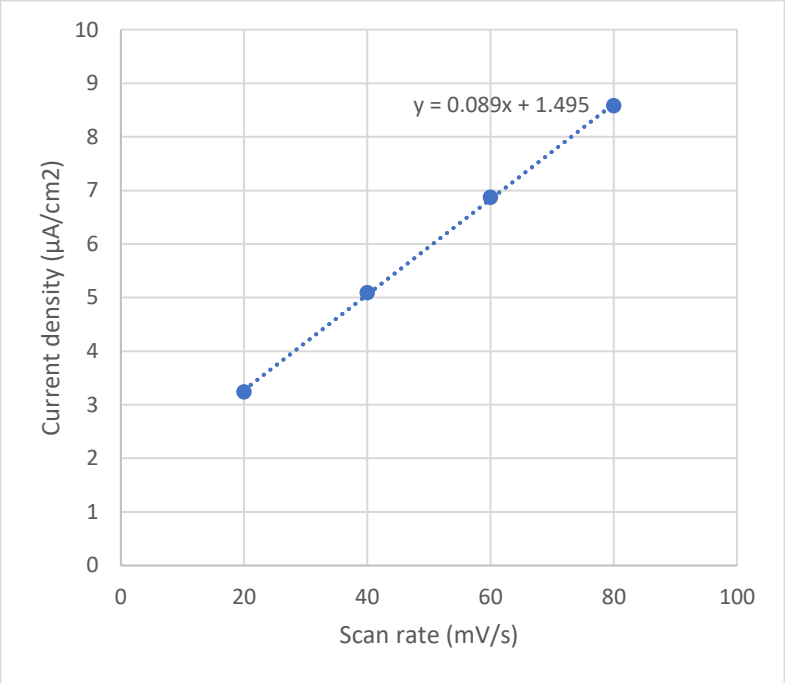

Figure 3-5 Determination of double-layer capacitance for Cu_2O GDE in 0.1M $HClO_4$, reference electrode: Ag/AgCl.

Firstly, the electrochemical surface area (ECSA) of the Cu_2O samples were calculated to be able to normalise their catalytic activity to ECSA. Double layer capacitance measurements were conducted by measuring the current density during CVs at different scan rates in 0.1M $HClO_4$ as shown in Figure 3-5 and Figure 3-6. Stainless steel was used to measure the capacitance of an ideal smooth surface: i.e., one that demonstrates the capacitance value of a perfectly smooth surface and finds the capacitance value with that specific electrolyte concentration.

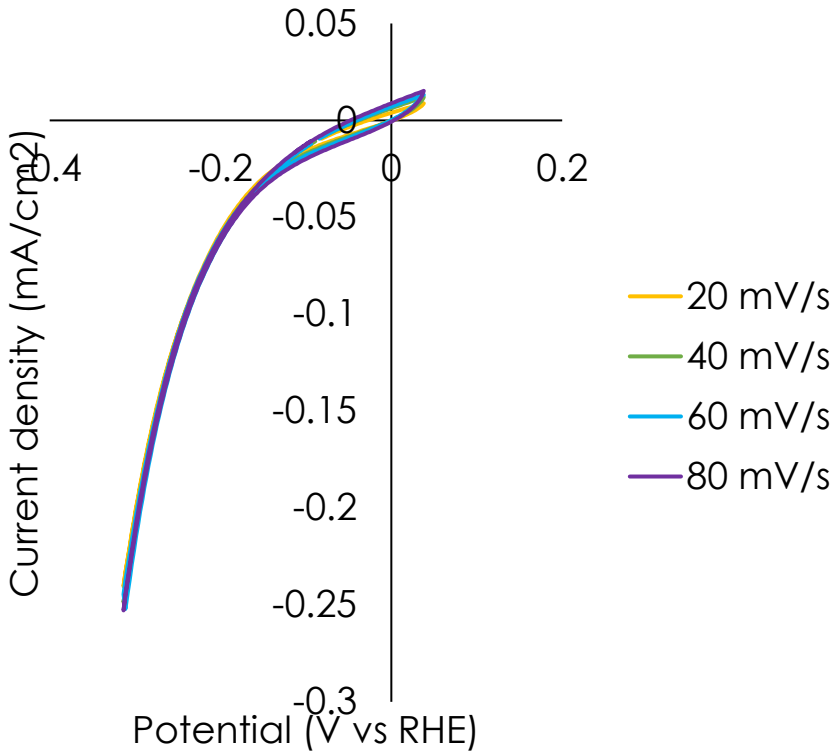

Figure 3-6 CVs for the determination of double-layer capacitance for Cu_2O GDE in 0.1M $HClO_4$, reference electrode: Ag/AgCl

Table 3-3 Calculation for Cu_2O sample by comparison to ideally smooth stainless steel

	Stainless steel	**Cu_2O**
Geometric area (cm^2)	2	2
Double layer capacitance	0.0235	0.089
Roughness factor	1	3.78
Actual surface area (cm^2)	2	7.56

0.1M $HClO_4$ was used to create a reducing environment under reductive potential to cause Cu_2O to reduce to metallic Cu. Cu_2O has low intrinsic conductivity[188], which can lead to non-ideal capacitive behaviour, which can lead to in accurate double layer capacitance measurements.[108,109] Hence the Cu_2O was converted to Cu to perform the ECSA measurements. However an issue with this electrochemical reduction is that the process of reducing Cu_2O to Cu could have changed its surface area. However, Cu_2O happens in-situ during CO_2 electroreduction in 1M KOH, hence it would have been more synonymous with experimental conditions to perform these ECSA measurements in 1M KOH. Using BET could have provided an alternative method for measuring surface area of the Cu_2O without having to reduce it.

The potential used extends into the HER window, demonstrated by the faradaic current in the region between -0.18 V vs. RHE and -0.38 V vs. RHE. Ideally the CV window should have been reduced to avoid the HER window as variation in ion concentration alter the dielectric properties and ionic mobility, affecting the Cdl measurement.[110]

To understand the stability of Cu_2O microparticles at various potentials, cyclic voltammetry measurements were performed either in nitrogen saturated 1M KOH electrolyte to investi

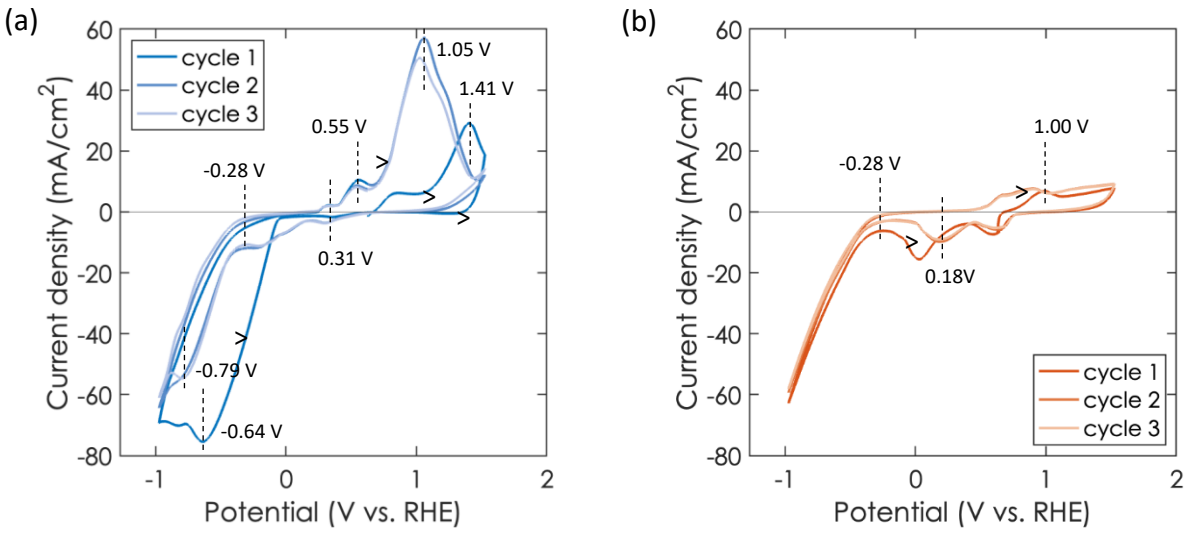

Figure 3-7 CV measurements of Cu2O microparticles. Three cycles were measured at a scan rate of 50 mV/s. (a) CV was performed in a nitrogen saturated 1M KOH aqueous electrolyte. (b) CV was performed in a CO2 saturated electrolyte.

gate redox events under inert conditions or in CO_2 saturated 1M KOH electrolyte to investigate redox events under conditions comparable to the electrocatalytic CO_2 reduction conditions. In Figure 3-7a, the starting voltage was 0.6 V vs. RHE and scanned in the positive direction as shown by the arrows. Cycle 1 exhibits peaks that vary from those in cycle 2 and 3. In cycle 2 and 3, one can clearly observe two anodic peaks at around +0.31 V vs. RHE and +0.55 V vs. RHE related to the oxidation of Cu(0)/Cu(I) and Cu(I)/Cu(II) and a significant anodic peak at 1.1V vs. RHE corresponding to $Cu(OH)_2$ formation. [111] There are cathodic peaks in cycle 1 at -0.64 V vs. RHE and -0.79 V vs. RHE in cycle 2 and 3 that could be attributed to the reduction of $Cu(OH)_2$. Also, the shift in potential of the peak

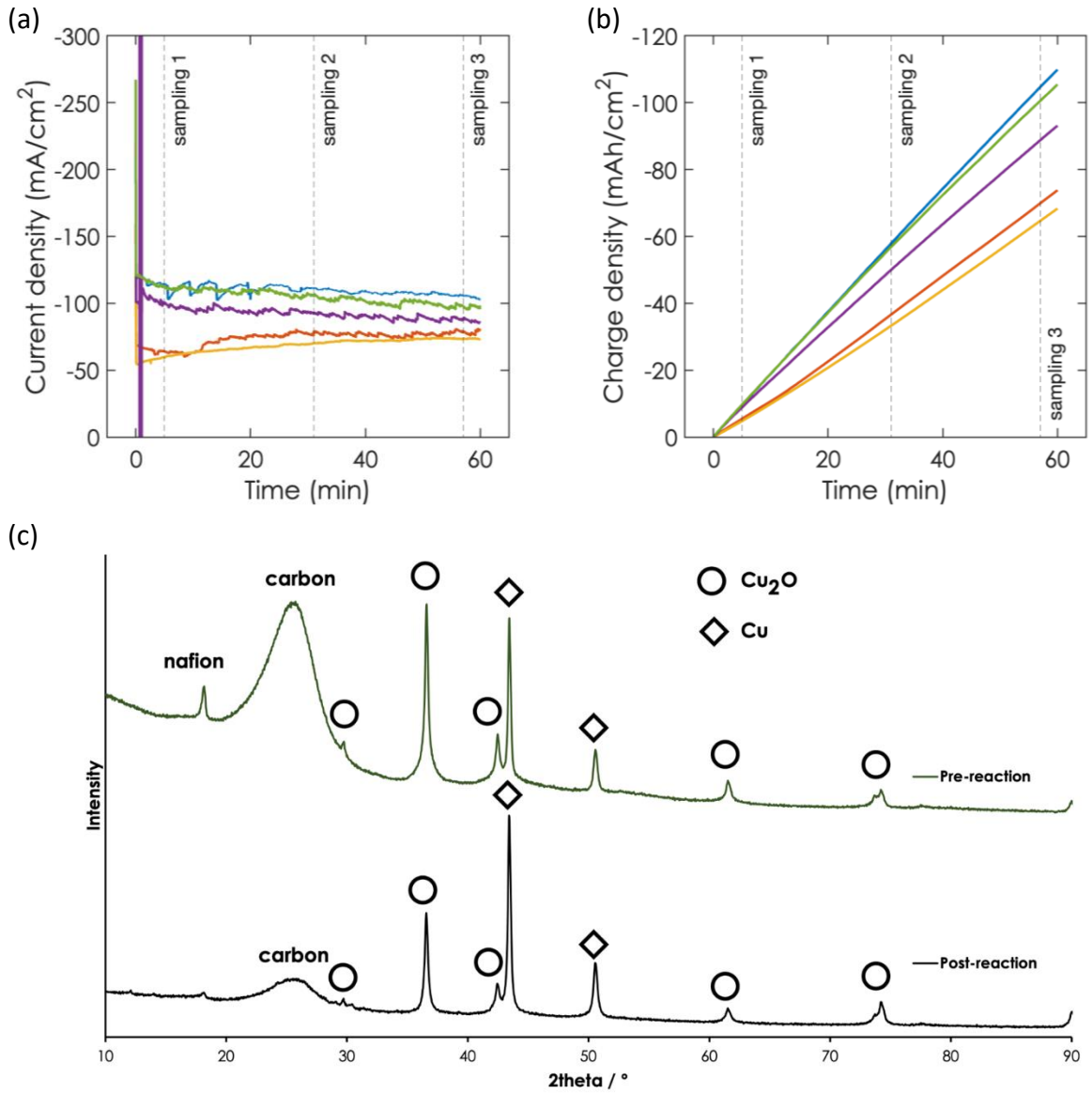

Figure 3-8. Chronoamperometric CO_2 reduction measurement at -1.17 V vs. RHE. (a) Current density of 6 samples during the 1-hour eCO2RR experiment. The geometric surface area of the samples was 2 cm^2. (b) Charge density of the samples during the 1-hour experiment. Sampling 1, 2 and 3 happened at 5, 31 and 57 min respectively. (c) XRD measurement of a sample before and after eCO2RR. The sample was synthesised before synthesis refinement as described in Section 2.3.1. Hence the synthesis resulted in a mixed Cu/Cu_2O sample as can be observed. In the post-reaction sample, the ratio of Cu has increased relative to Cu_2O. performed under analogous conditions as the measurement of Cu_2O samples shown in 3-7 but directly before and after a chronoamperometric CO_2 reduction measurement.

at 1.41 V vs. RHE of cycle 1 to 1.05 V vs. RHE in cycle 3 is observed in the same direction for the shift seen of the peak of 0.64V vs. RHE in cycle 1 to 0.79V in cycle 3. In Figure 3-7b, upon

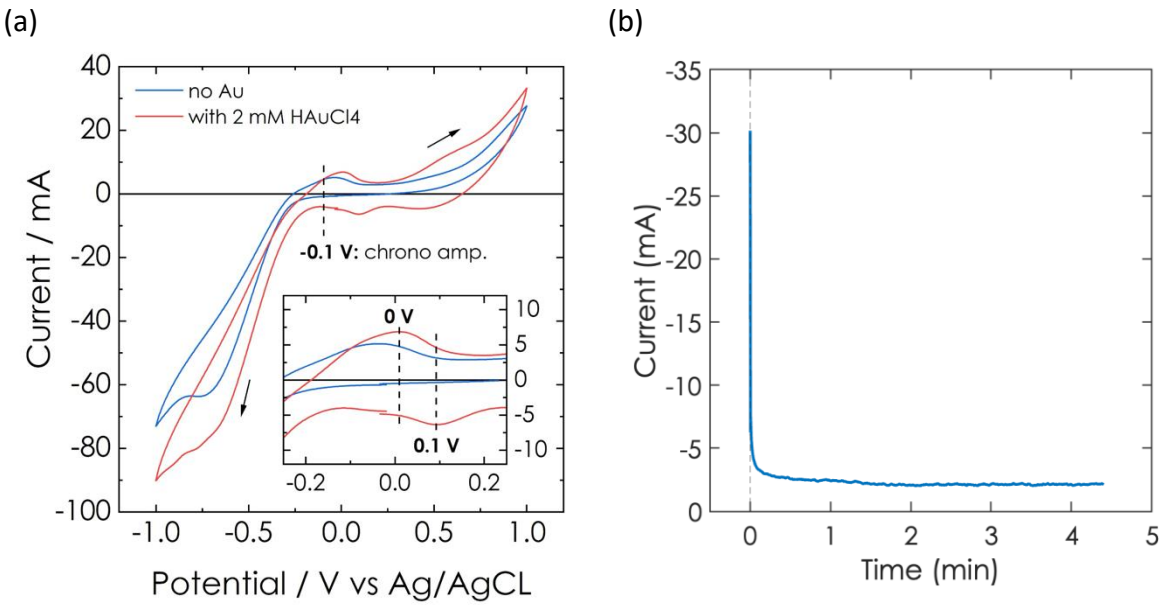

Figure 3-9. Electrodeposition of Au from $HAuCl_4$ onto Cu_2O microparticles on a gas diffusion membrane. (a) CV measurements of the Cu2O catalyst in an electrolyte with (red) or without (blue) $HAuCl_4$. In presence of $HAuCl_4$, an additional redox peak becomes visible (inset). (b) Electrodeposition of Au using a chrono amperometric measurement at a potential of -0.1 V vs. Ag/AgCl. After an initial current drop, an approximately steady state current response of -2.2 mA could be observed.

the addition of CO_2 there is absence of the anodic peak associated with $Cu(OH)_2$ and the associated cathodic peaks in Figure 3-7a which hence could be attributed to the reduction of $Cu(OH)_2$. Also, the CV shape remains the same during cycle 2 and 3 demonstrating stability of the material under these electrochemical conditions. The onset potential of the hydrogen evolution reaction in Figure 3-7a and b is -0.28 V vs. RHE and reaches the same magnitude of current density at 60 mA/cm^2. CO_2 purging will in 1M KOH will likely enable the reaction between hydroxide ions and aqueous CO_2, which will drop the pH. This change in pH was not measured and hence was not taken into account when plotting the CV in Figure 3-7b. The shift in pH could provide justification for the change in peak position.

To measure eCO2RR catalyst performance a steady-state potential was applied (-1.17 V vs. RHE) for 1 h across all samples that is more negative than the reduction potential of CO_2. -1.17 V vs RHE was chosen due to it being being an effective operating potential for achieving a large current density (~100 mA/cm^2) whilst generating a high faradaic efficiency for carbonaceous products, specifically C2 products. The respective current response is monitored against time and shown in Figure 3-8a, hence calling this measurement chronoamperometric. To obtain a reliable result, the measurement was performed with different samples 5 times. A slight variation of current density response can be observed, ranging between -50 and -120 mA/cm^2. This is in the range of reported current densities for Cu_2O. 35 Furthermore, small current spikes can be observed, that most likely result from product gas bubble evolution on the catalyst surface. Note that throughout the measurement, the current response remains approximately stable, which indicates a good catalyst stability. This also becomes evident when looking at the accumulated charge over time (see Figure 3-8b). An approximately linear increase in charge was observed, indicating a constant current.

3.2.2 Au-Cu_2O catalyst characterisation

In the following, the modification of the Cu_2O catalysts is discussed when functionalized with gold. Firstly, the different gold deposition techniques are discussed and then the investigation the gold modified catalysts, both structurally and electrochemically.

3.2.2.1 Gold deposition technique

In the next step, gold-deposited samples of Cu_2O microparticles were fabricated as described in the Methods section. The Cu_2O samples were modified further with the deposition of metallic gold onto the Cu_2O itself. Different techniques were used to apply gold to the sample,

such as galvanic replacement, photo-deposition and electrodeposition. The techniques utilise different driving forces (electrical, chemical and photo-) to cause a gold salt ($[AuCl_4]^-$) present in the electrolyte to precipitate metallic gold particles onto the surface of the Cu_2O electrode. The reaction is a 3-electron reduction of Au^{3+} as reported in the literature for depositing gold nanoparticles.[113] The reduction reaction is shown as follows:

$$[AuCl_4]^- + 3e^- \longrightarrow Au + 4Cl^- \qquad E^0 = 1.0\ V \qquad (3\text{-}2)$$

where E^0 is the respective standard potential of $HAuCl_4$.[114] The corresponding oxidation reaction depends on the deposition technique.

Galvanostatic replacement can produce versatile nanostructures by utilizing the oxidation reaction of the substrate catalyst.[115] In case of copper, the standard potentials range from -0.34 V in basic conditions and 0.20 V in acidic conditions to 0.34 and 0.52 V.[116–118] Respective reaction equations are given in the following:

$$Cu_2O + H_2O + 2e^- \longrightarrow 2Cu + 2OH^- \qquad E^0 = -0.36\ V \qquad (3\text{-}3)$$

$$Cu_2O + 2H^+ + 1/2\ O_2 \longrightarrow 2Cu^{2+} + 2OH^- \qquad E^0 = 0.20\ V \qquad (3\text{-}4)$$

$$Cu^{2+} + 2e^- \longrightarrow Cu \qquad E^0 = 0.34\ V \qquad (3\text{-}5)$$

$$Cu^+ + e^- \longrightarrow Cu \qquad E^0 = 0.52\ V \qquad (3\text{-}6)$$

Crucially, all standard potentials are more negative than the $[AuCl_4]^-/Au$ standard potential, which causes the formation of Au nanoparticles. Since the experiment was performed under slightly acidic conditions due to the addition of acidic $HAuCl_4$ and Cu_2O microparticles are

present, equation 3-4 occurs most likely. The evolved Cu^{2+} is present as aqueous ions the electrolyte. No blue colour was seen in the electrolyte. A description of the synthesis is given in Section 3.4.2.

Photodeposition utilizes light irradiation to produce excitons in a photoactive material, that in return can provide photogenerated electrons if photogenerated holes are quenched by a sacrificial electron donor.[119,120] Hole quenching has to occur on a faster time scale than exciton recombination (which is the process of recombination of photogenerated electrons with holes) since otherwise no photocurrent will be produced. Here, a 100 W Xe lamp was utilized as the light source, and methanol was used as the sacrificial electron donor to quench photogenerated holes. The pH of the solution was controlled by adding NH_4OH.

In case of electrodeposition, the reduction agent providing electrons is the potentiostat connected as part of the experimental set-up. To evaluate the redox potential of $HAuCl_4$ under respective reaction conditions with Cu_2O as the catalyst, an electrochemical study was conducted with cyclic voltammetry measurements, as shown in Figure 3-9a. When looking at the measurement without $HAuCl_4$, the typical CV shape of Cu_2O microparticles becomes evident, with a respective water reduction (HER) onset potential of ca. -0.3 V vs. Ag/AgCl (see Figure 3-9a). However, when adding $HAuCl_4$ to the solution, two additional peaks become evident at 0 and 0.1 V vs. Ag/AgCl, corresponding to a respective redox potential of 0.05 V vs. Ag/AgCl for the Au reduction reaction (see equation (3-2)). Hence, it can be deduced that Cu_2O was capable of the electrochemical reduction of $HAuCl_4$. Furthermore, a potential for the chronoamperometric (CA) electrodeposition of Au was chosen to be more negative than 0 V and more positive than the water reduction onset of 0.3 V. Thus, -0.1 V vs. Ag/AgCl was chosen as applied potential for CA and the corresponding electrodeposition experiment is shown in

Figure 3-9. An initial current of -30 mA is observed, that rapidly drops within the first 30 sec of the measurement and stabilizes at a current of ca. -2.2 mA. The first initial current drop likely occurs due to double layer capacitance (the rectangular shape at potentials where no catalytic reaction should occurs (e.g., between +0.2 and +0.3 V vs. Ag/AgCl) is caused by double layer charging) but more strongly due to formation of the diffusion layers of product and reactant – a behaviour described by the Cottrell equation. The steady state current that subsequently develops can be linked to the electrocatalytic reduction of $HAuCl_4$ and hence the amount $n_{Au}[mol]$ of Au deposited onto Cu_2O can be controlled via the duration of the CA experiment:

$$n_{Au}[mol] = \frac{\int I(t)\, dt}{z \cdot F} \qquad (3\text{-}7)$$

where the charge is obtained from integrating current I over measurement duration , F is the Faraday's constant, and z is the number of transferred electrons during the $HAuCl_4$ reduction reaction (3 electrons). A CA electrodeposition time was chosen so that 1 wt% of Au in respect to the Cu_2O GDE was deposited. The required time was 4.4 min.

3.2.2.2 Structural characterization of Au-Cu_2O.

To ensure successful deposition of Au onto the Cu_2O catalyst, a material character analysis was performed. PXRD of the samples were measured, as shown in Figure 3-10 for an exemplary sample that used galvanostatic exchange to deposit gold. The diffraction pattern 2θ = 29.8°, 36.7°, 42.5°, 61.7° correspond to the (110), (111), (200) and (220) planes, respectively, for Cu_2O (ICDD file no. 96-900-7498). This suggests that Cu_2O is present in the samples, as

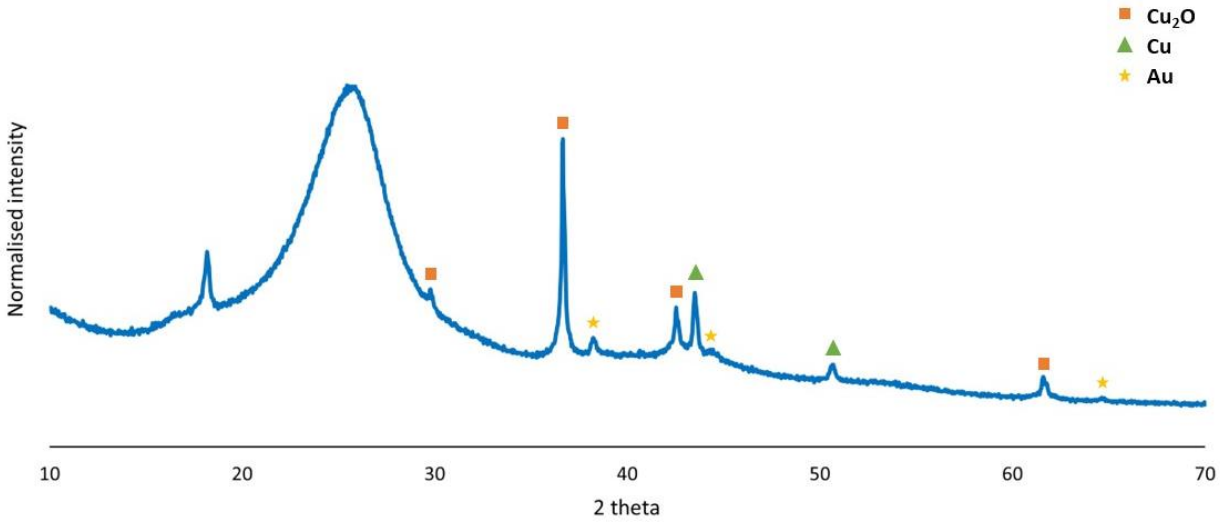

Figure 3-10. PXRD of Au-Cu_2O synthesised by galvanic exchange of Cu2O with $[AuCl_4]^-$. Peaks corresponding to Cu_2O, Cu, and Au are color-coded with orange, green, and yellow, respectively. Elemental copper is resulting from the redox reaction during galvanic exchange.

expected from the synthesis. Furthermore, the other peaks at 2θ = 38.2°, 44.3°, 64.7° correspond to the (111), (220) and (220) planes, respectively for Au (ICDD file no. 96-900-8464). This indicates that gold was indeed deposited onto the catalyst. The diffraction pattern at 2θ = 43.2° and 50.9° are attributed to the (1 1 1), (2 0 0) of the Cu structure (ICDD No. 96-901-2044). The peak at 2θ = 25.4° is the diffraction response from the carbon paper material and the peak at 2θ = 182° is due to the Nafion binder used in the catalyst ink. There are no peaks for CuO suggesting that Cu_2O was not oxidised to CuO in any detectible quantities by XRD.

From this analysis, it can be concluded that gold was deposited, and the Cu_2O catalyst was not chemically modified in significant quantities.

Next, SEM was used to study the morphology of Au-Cu_2O composite materials. In Figure 3-11, the SEM image shows that the structure is generally homogenous through the entire imaged section. EDX was simultaneously performed to understand the composition of the catalyst and to attempt to quantify the amount of deposited gold. EDX was measured in three different spots and the result of the study is shown in Table 3-4. The EDX shows the presence of copper to oxygen as approximately 2:1 which corresponds to the atomic ratio of Cu_2O. The ratio of Au to Cu was 5:95. The presence of carbon, oxygen, and fluorine observed in the EDX can be attributed to the presence of Nafion, (chemical formula, $C_7HF_{13}O_5S$. C_2F_4)[121] in the catalyst ink used to formulate the catalyst layer. However, sulfur is not detected in the EDX, possibly due to its small atomic ratio in the chemical formula. Chlorine is also detected in low

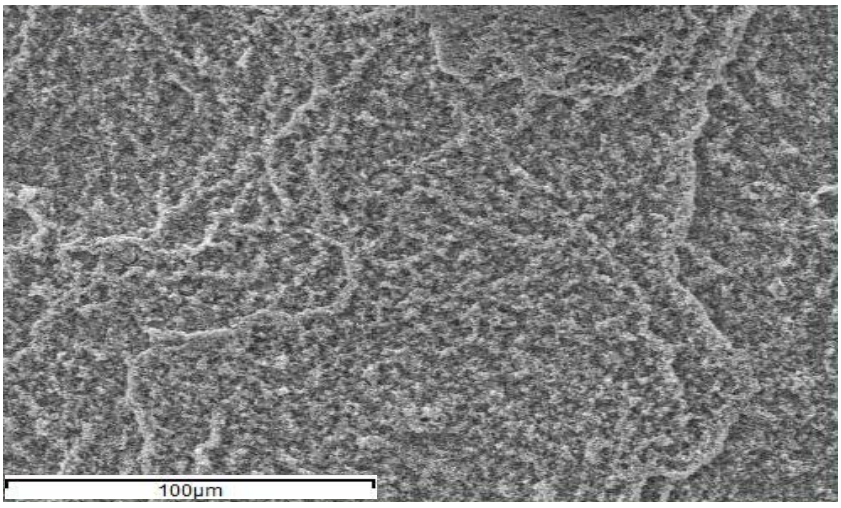

Figure 3-11 SEM image at 500X magnification of as-prepared photodeposited Au-Cu_2O samples. The measurement was performed with a secondary electron detector.

atomic percentage, however its variation across the 3 points studied with EDX correlates with

that of the Au, which is deposited from $HAuCl_4$. It suggests that both gold and Cl are both deposited in an approximate 2:1 ratio. However, the identity and involvement of chlorine in the sample is unknown.

Table 3-4. EDX results of photodeposited Au-Cu_2O. The average of 3 points on the sample is shown.

Element (shell)	**Mean Atomic %**	**Standard deviation**	**Standard deviation as a % of atomic %**
C (K)	21.78667	0.45	2%
O (K)	20.14	0.94	5%
F (K)	17.14333	0.75	4%
Cl (K)	0.783333	0.25	32%
Cu (K)	38.23333	0.69	2%
Au (M)	1.916667	0.72	38%

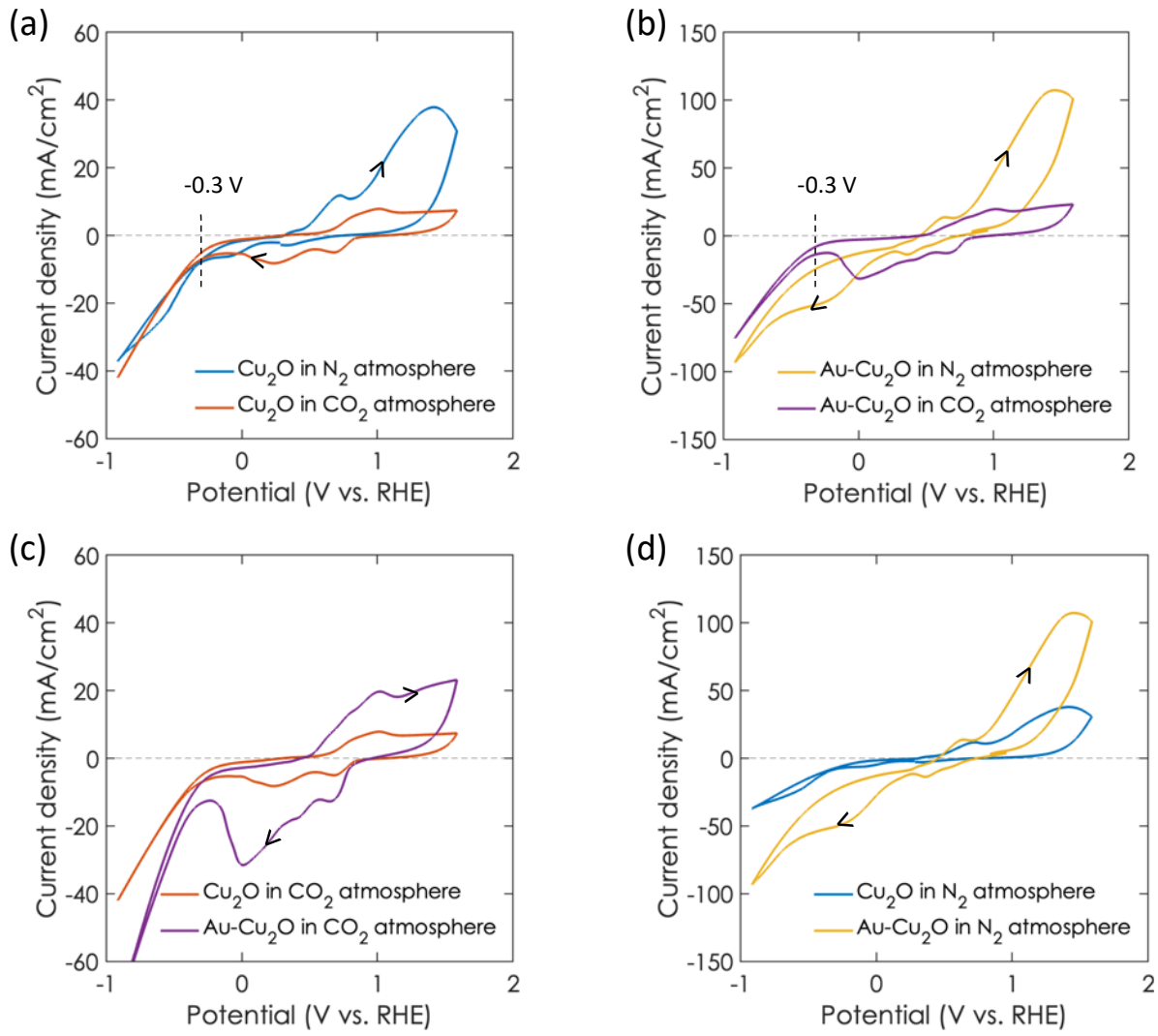

Figure 3-12. CV analysis of various catalyst samples. CV measurements are performed in 1 M KOH electrolyte at a scanrate of 50 mV/s. (a) Cu2O samples are measured in an electrolyte degassed with N_2 or CO_2. (b) $AuCu_2O$ samples are measured in an electrolyte degassed with N_2 or CO_2. (c) Comparison of Cu_2O and $AuCu_2O$ samples when measured in an CO_2 degassed electrolyte. (d) Comparison of Cu_2O and $AuCu_2O$ samples when measured in an N_2 degassed electrolyte.

We can conclude that gold was deposited onto the sample and that the Cu_2O catalyst is still present.

3.2.2.3 Electrochemical characterization of Au-Cu_2O

We proceed to perform an electrochemical analysis on the Au-Cu_2O samples. Cyclic voltammetry was performed in both N_2 and CO_2 saturated electrolytes to gain understanding of the electrochemical processes of gold modified Cu_2O samples within the 1M KOH electrolyte in the potential window of -1 to +1.6 V vs. RHE. It was important to ensure that the electrochemical signature of Cu_2O, which was discussed in Section 4.2.1.2, had not been modified during gold deposition. Results of the CV analysis are shown in Figure 3-12.

In Figure 3-12a, the CV scans of Cu_2O samples are shown, when measured in N_2 and CO_2 atmosphere. The resulting scan shape was comparable to the measurement discussed in Figure 4.5, with a clear water reduction current onset evident at a potential of approximately -0.3 V vs. RHE (note that small deviations occurred between peak shape and position compared to measurements shown in Figure 3-7, which were explained with slight deviations in the sample preparation routine). Note that this onset is similar for both respective measurements under N_2 and CO_2 atmosphere, underlining that most of the reductive current results from water reduction.

Next, CV measurements were performed under similar conditions with Au-Cu_2O fabricated via electrodeposition. Results are shown in Figure 3-12b. Importantly, both for N_2 and CO_2 saturated electrolyte the shape looks very similar compared to Cu_2O samples (Figure 3-12a), with an electrocatalytic reductive current onset at a potential of ca. -0.2 to -0.3 V vs. RHE. Furthermore, respective reduction peaks of Cu(II) to Cu(I) and Cu(I) to Cu(0) can be observed at 0.5 V vs. RHE and -0.1 V vs. RHE. Respective oxidation peaks of Cu(0) to Cu(I) and Cu(I) to Cu(II) are located at 0.75 V vs. RHE and 1.2 V vs. RHE. This underlines that the electrochemical signature of Au-Cu_2O samples does not deviate significantly from Cu_2O samples and hence

the catalytic modification in performance can be attributed to either a slightly different sample morphology or the impact of deposited Au nanoparticles modifying electrocatalytic performance.

To allow an easier comparison between the magnitudes of electrocatalytic reductive currents, measurements of Cu_2O and Au-Cu_2O were plotted in the same plot in a N_2 atmosphere (Figure 3-12c) and CO_2 atmosphere (Figure 3-12d). For both cases, a significantly larger current by a factor of ca. 2 can be observed more negative than the electrocatalytic reductive current onset. This might indicate onto an enhanced electrocatalytic performance and thus underline that Au indeed modifies the electrochemical performance. Note also that under CO_2 atmosphere, the reduction peaks are shifted slightly negative by around 0.1 to 0.2 V for the Au-Cu_2O sample when compared to the Cu_2O sample. Possible reasons include a slight deviation in local pH due to the larger electrocatalytic performance of the HER.

A calculation of the overpotential via the tafel analysis was challenging due to the multiple redox events present. The overpotential of the $AuCu_2O$ in CO_2 saturated 1M KOH electrolyte was observed to shift by ~50 mV with respect to Cu_2O.

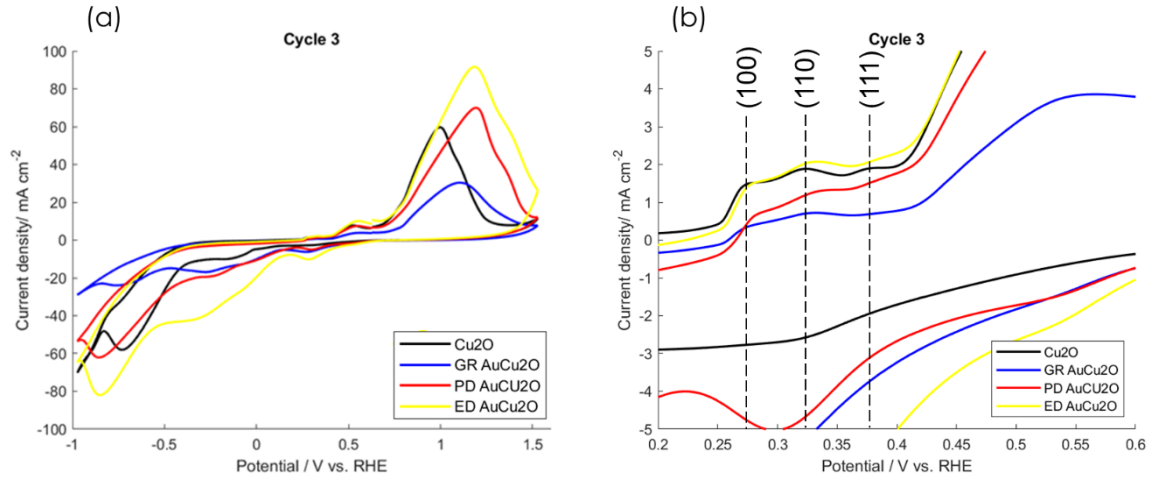

Figure 3-13 a) CV of N_2 saturated 1M KOH at 50 mV/s of Cu_2O and galvanic replacement (GR) $AuCu_2O$, photodeposited (PD) $AuCu_2O$ and electrodeposited (ED) $AuCu_2O$. The third cycle of the CV is shown here. B) magnified section of CV shown in a). Specifically showing OH_{ads} peaks in the region of 0.25 to 0.4 V vs. RHE.

Previous research found that the adsorption of hydroxyl ions on different Cu crystal planes resulted in individual, separate anodic peaks.[122] More recent work has used this electrochemical signal to quantify the ratio of (100), (110), (111) facets on the surface of Cu nanowires[123] and on the surface of electrochemically reduced CuO nanosheets[124] In this research, CVs were conducted on each Cu_2O and $AuCu_2O$ in N_2 saturated electrolyte of 1M KOH. Hence, the cathodic current reduces the Cu_2O to Cu. The OH_{ads} on the Cu surfaces of all the samples can be

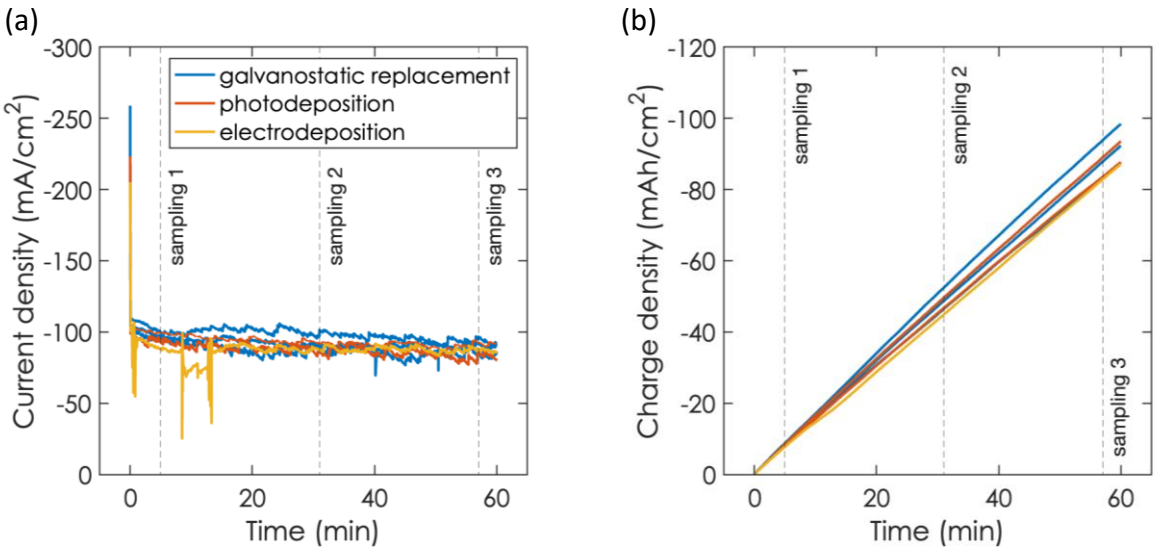

Figure 3-14 Chronoamperometry measurement of the different deposition techniques of Au-Cu_2O. a) Current density against time b) charge density against time

observed in Figure 3-13a). The peaks for the adsorption of OH were at ~0.27, ~0.33, ~0.38 V vs. RHE for (100), (110) and (111). The relative intensities of the OH_{ads} signals at (100), (110), and (111) were similar in terms of current density, indicating the polycrystalline surface characteristics of the Cu_2O microparticles. There was consideration as whether the deposition of Au would happen with a specificity to a certain facet that would result in the reduction of a peak intensity. However, there is no stark difference between peak intensity of the Cu_2O and $AuCu_2O$. This could be due to the low percentage of gold deposited. It would have been better to have done this CV within a more limited potential window, for example, maximum potential at 0.6 V vs. RHE to prevent bulk oxidation of Cu. Furthermore, the scan rate could have been altered to observe the peaks more clearly.

Next, a chronoamperometric experiment was performed with Au-Cu_2O under electrocatalytic CO_2 reduction conditions. In Figure 3-14a, the current density of the Au-Cu_2O is presented for

samples deposited via galvanostatic replacement, photodeposition, or electrodeposition, as discussed in Section 3.2.2.1. The current densities of all samples are consistent across the reaction duration of 1 h. When compared with the current densities of the Cu_2O samples, the current densities are similar in magnitude. Moreover, no significant difference can be observed for samples where gold was deposited via the different techniques. This becomes even more evident when looking at the utilised charge in Figure 3-14 b and indicates that the rate of faradaic reactions of Au-Cu_2O are similar to that of the Cu_2O samples, independent of gold deposition method. It further enables t directly compare the faradaic efficiencies and selectivity of the Cu_2O and Au-Cu_2O catalysts without attributing the differences to current density variation.

3.2.3 Characterisation of Galvanic Replacement $AuCu_2O$

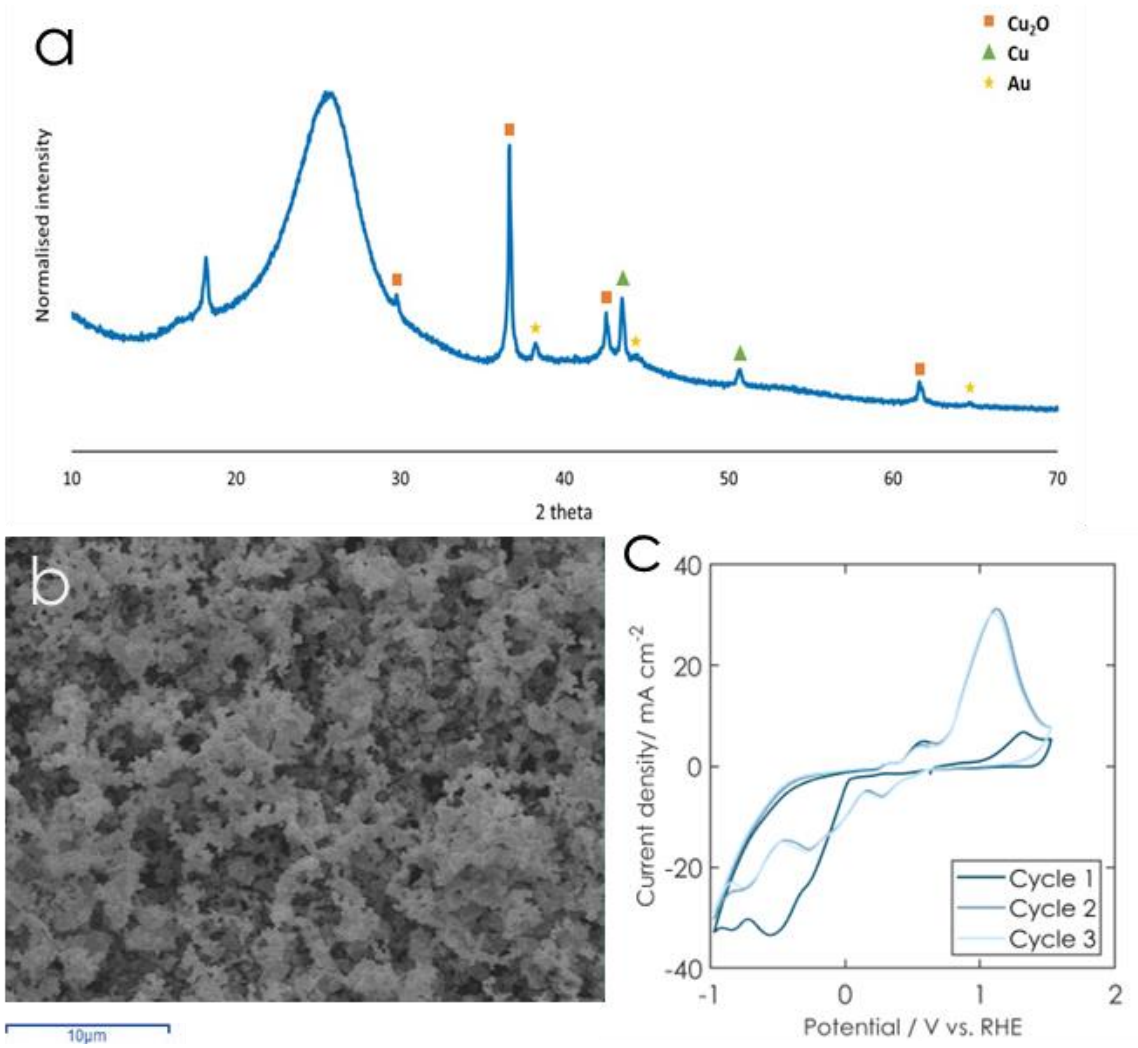

Figure 3-15 a) PXRD of Au-Cu_2O synthesised by galvanic exchange of Cu2O with $[AuCl_4]^-$. Peaks corresponding to Cu_2O, Cu, and Au are color-coded with orange, green, and yellow, respectively. Elemental copper is resulting from the redox reaction during galvanic exchange.b) SEM image of the surface of the of the GR $AuCu_2O$. c) CV of GR $AuCu_2O$ in N_2 environment in 1M KOH with a scan rate of 50 mV/s.

The PXRD as shown in Figure 3-15a) was discussed in Section 3.2.2.2. It shows the presence of gold as well as Cu_2O and Cu. However, the EDX results shown in Table 7 find no oxygen present, which would be expected if Cu_2O was present. The different findings in these two characterisation techniques could be due to the different penetration depths of PXRD and EDX.PXRD has penetration depths of micrometers to millimteres, whilst EDX is more surface

sensitive, with penetration depths of nanometers to micrometers. These findings suggest that the bulk of the electrocatalyst varies from the surface where galvanic replacement occurred and it is unlikely any Cu_2O remains.

Table 5 EDX of the GR $AuCu_2O$ sample

Element	Weight %	Atomic
F	2.87	22.40
Cu	2.84	6.63
Au	94.29	70.97

3.2.3.1 Comparison of GR $AuCu_2O$ and Cu_2O

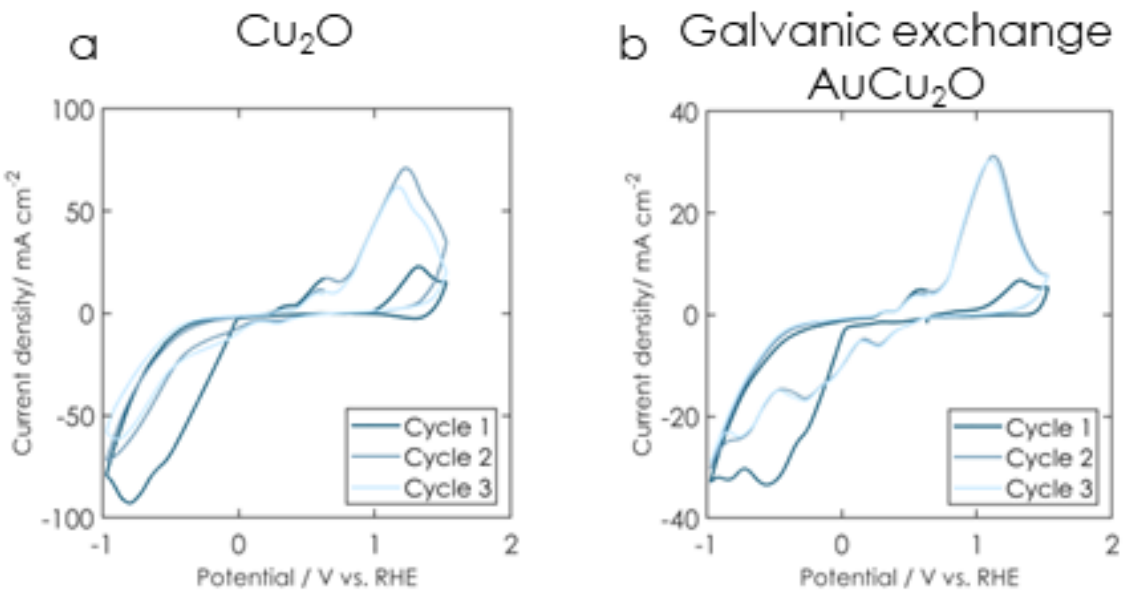

Figure 3-16 a) CV of Cu_2O in N_2 environment in 1M KOH with a scan rate of 50 mV/s.
b) CV of GR $AuCu_2O$ in N_2 environment in 1M KOH with a scan rate of 50 mV/s.

In Figure 3-16, the CVs of Cu_2O and GR Au Cu_2O are compared. Cu_2O sample has higher absolute current densities indicating greater redox activity. This could potentially be related to less Cu in the $AuCu_2O$ sample, if the redox activity is related to copper. The broad reduction peak around -0.6 to -0.8 V vs RHE is associated with the reduction of copper oxides to metallic

copper. The peak is shifted towards more positive potentials in the GR $AuCu_2O$ sample, indicating that the presence of gold modifies the electrochemical behaviour of the reduction.

In Table 6, the EDX of Cu_2O shows oxygen is present, however in an ideal, pure Cu_2O sample, you would expect a higher percentage of oxygen than what was found. This indicates an impure sample of mixed Cu and Cu_2O.

Table 6 EDX of the Cu_2O sample

Element	Weight %	Atomic %
O K	5.09	16.70
F K	2.55	7.05
Cu K	92.36	76.25

3.3 Conclusion

In this chapter, Cu_2O catalysts for electrochemical CO_2 reduction were investigated. Three different gold deposition methods were analysed: galvanostatic replacement, photodeposition, and electrodeposition. Structural characterization underlined that the methods lead to a homogeneous deposition of gold. The overpotential of the $AuCu_2O$ in CO_2 saturated 1M KOH electrolyte was observed to shift by ~50 mV with respect to Cu_2O. This was an indicator that $AuCu_2O$ would perform with high current density and hence these catalysts were taken forward to measure their product selectivity of which data is shown in the next chapter.

3.4 Experimental Methods

3.4.1 Cu_2O Catalyst Synthesis and Film Preparation

Cu_2O microparticles were synthesised by hydrolyzation and chemical reduction of copper acetate (Sigma Aldrich, 99.8%) with glucose (anhydrous, Sigma Aldrich) as previously published (Zhang et al., 2012). The ratio of water(mL):ethanol(mL) used was 10:70. The microparticles were washed in ethanol and water before being separated via centrifugation (6000 rpm, 30 min). The particles were then dried under Schlenk conditions at 80°C for 48 h.

3.4.2 Gas Diffusion Electrode preparation

The gas diffusion electrodes (GDE) were prepared by spraying catalyst ink on to the gas diffusion layer (H2315 I2 C6, Freudenberg). The catalyst ink was prepared by dispersing 10 mg cm-2 Cu_2O microparticles within 100 µL cm^{-2} of isopropanol and 17 µL cm^{-2} (Nafion suspension, 5 wt%, Sigma Aldrich). The ink is sonicated for 20 min upon the addition of the microparticles to isopropanol and then a further 15 min when the Nafion binder is added. The ink is then sprayed onto the commercial gas diffusion layer that is heated on a hotplate at 45°C.

3.4.3 Au Deposition on Cu_2O GDEs

Electrodeposition was chosen to reduce gold onto a Cu_2O-GDE by running chronoamperometry for a Cu_2O-GDE in a solution of $HAuCl_4$ to reduce Au^{3+} to metallic gold on the surface of the Cu_2O GDE. The electrochemical set-up was a 3-electrode cell, with Cu_2O GDE as working electrode, a Pt wire as counter electrode, and an Ag/AgCl reference electrode. The electrolyte was 2 mM $HAuCl_4$ in 1M KCl (aq). CV and CA measurements were performed with an Autolab potentiostat. Different optimizations were carried out to optimize the experiment: Different

counter electrode sizes were employed to prevent current limitations. An anion exchange membrane was employed with an adapted H-cell that had the ability to sandwich a membrane between the anolyte and catholyte.

Photodeposition was performed by submerging a prepared Cu_2O GDE in 2mM $HAuCl_4$ in a small beaker with a diameter of 4 cm^2. The volume of the 2 mM $HAuCl_4$ solution used was 13 ml. 0.200 ml of methanol was used as a sacrificial electron donor. The samples were then illuminated with 0.1% light intensity filtered 100 W xenon lamp (Newport) for 30 minutes. The sample was then washed with DI water and then dried in the oven at 70°C for 3 hours.

Galvanic exchange of gold and Cu_2O was performed by dissolving 0.175 g of $HAuCl_4$ in 50 ml of water to produce a solution of ~0.01 M $HAuCl_4$. Prepared Cu_2O gas diffusion electrodes as described in Section 3.4.2 were submerged in 10 ml of solution for 1, 3, 5 and 10 minutes respectively. The sample was then removed and gently submerged in water before being removed and placed in an oven to dry at 70°C for 3 hours.

4

Evaluation of catalytic selectivity for eCO2RR of Hierarchically Structured Cu_2O Microparticles with Gold Deposition

Ella Fidment, Eileen Yu, Elizabeth Gibson, Preetam Sharma

Abstract

The electrochemical conversion of carbon dioxide (CO_2) into value-added multi-carbon products represents a promising avenue for sustainable chemical synthesis. Key to advancing this technology is the development of catalysts capable of enhancing the production rate of higher-value compounds, typically multi-carbon molecules. This research found that Au-Cu_2O catalysts exhibit a superior production rate for oxygenate products, ethanol and propanol, with respect to Cu_2O. Conversely, Cu_2O catalysts demonstrate a higher production rate for ethylene, showcasing the intrinsic catalytic activity of copper oxide. This difference in production rates for ethylene and oxygenate products is believed to stem from the degree of *CO surface coverage, which previous studies1 have found that at low CO coverage the ethylene pathway is kinetically favoured and at high coverage the oxygenate pathway is favoured. Au is employed to enable facile *CO production, hence the Au-Cu_2O has high *CO coverage promoting the oxygenate pathway.

4.1 Introduction

The choice for the use of 1M KOH as the catholyte in the gas diffusion electrode flow cell for the catalyst testing was with the aim of reducing the activity for HER.16 It also reduces the onset potential difference between CO and C_2H_4.[69]

The work to deposit Au onto Cu_2O is inspired by the Indium-Cu_xO work researched by Hang Xiang, supervised by Eileen Yu.[127] Their work utilised electroless spontaneous precipitation of a cell set-up whereby the electrodeposition of $In(OH)_3$ onto the Cu_2O electrode was driven by the oxidation of the anode of indium. Indium was found to be selective towards formate by Hori[34.] Inspired by deposition onto Cu species, gold was chosen because of its selectivity towards carbon monoxide. However, a different deposition technique was required to deposit gold onto Cu_2O as it has a very high oxidation potential, hence the anode potential would not be able to drive the electroless spontaneous reaction as was the case with indium. Hence different reduction methods were explored with different anodes and gold in solution with different reducing agents.

4.2 Results and Discussion

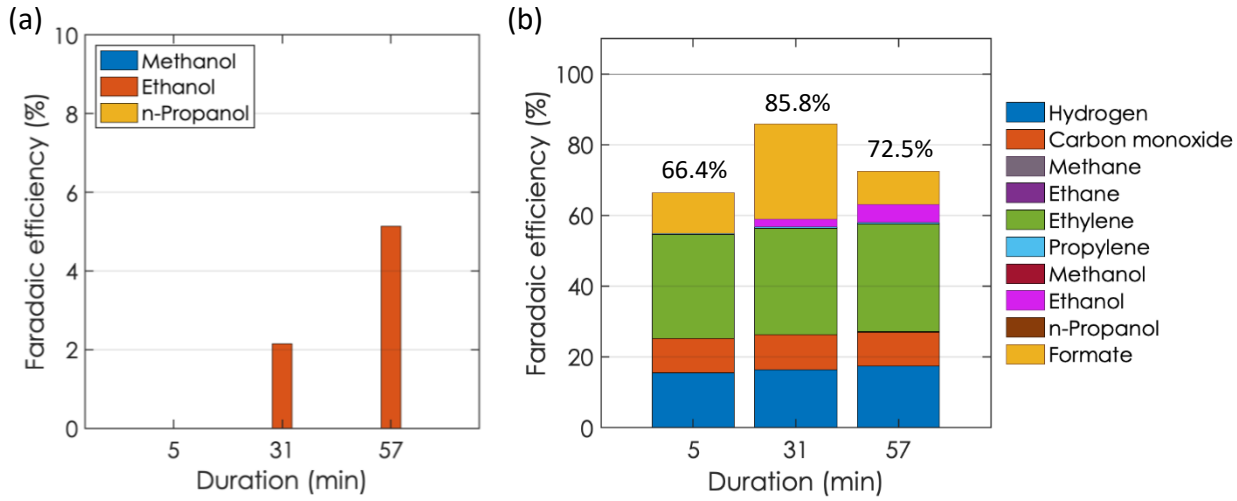

Figure 4-1 Faradaic efficiencies of Cu_2O samples. Sampling at 5, 31 and 57 min into the reaction, potential at -1.17 V vs. RHE, reference electrode RE-61AP, Pt mesh as the counter electrode, Nafion membrane (Fumapem F-950), the catholyte used was 1M KOH, the anolyte was 5M KOH. (a) Liquid product analysis for Cu2O GDE samples via LC. Only ethanol was detected for sampling times at 31 and 57 mins. (b) Overall faradaic efficiency of Cu2O sample with GC, IC and LC analysis products.

4.2.1 Evaluation of Cu_2O GDE catalyst for eCO2RR

Samples of Cu_2O gas diffusion electrodes were tested intially to establish the faradaic efficiencies of the products evolved. The deposition techniques and characterisation are discussed in detail in Chapter 4. To evaluate the catalyst performance towards different gaseous and liquid CO_2 reduction products, both evolved gases and electrolyte were sampled, and the amount of products was analysed by means of gas chromatography and ion chromatography. This sampling was performed at 5, 31, and 57 mins. The frequency of sampling times was determined by the most frequent intervals that could be used with the gas chromatography method which required time to run and for the column to cool down after a run. The details of product characterization are given in the Methods section and in Section 4.4. The resulting faradaic efficiency (FE) is shown in Figure 4-3.

A significant and consistent FE can be observed for hydrogen, carbon monoxide, ethylene and formate independent of duration of the experiment. This underlines that both hydrogen and carbon monoxide were evolved as well as the multi-carbon product, ethylene. Alternatively, much smaller FE are observed for both methane and propylene, sometimes neither of these products were detected at all. This result is to be expected, since these products require a longer reaction pathway.[128] No ethane was detected at any stage during the reaction.

When evaluating the standard deviation amongst the different products, it can be observed that the standard deviation of formate is significantly higher than any of the other products, indicating a larger experimental error. This could be due to the difference in methodology of analysis between liquid (IC and GC detection) and gas (GC detection) phase products. Liquid-phase products are dissolved in the electrolyte which is circulated between the cell and electrolyte reservoir via peristaltic pumps. A sample of electrolyte is taken at a duration of 5, 31 or 57 min from the reservoir and analysed. There is an assumption that the concentration of the liquid products is homogenous in the electrolyte due to mixing when the peristaltic pump circulates the electrolyte between the reservoir and electrochemical cell. However, the standard deviation of the faradaic efficiency of the formate would suggest that the concentration of formate is not equal throughout the electrolyte. As seen in Figure 4-4, the standard deviation of the formate decreases over longer durations. As the formate concentration accumulates in the electrolyte over the duration of the reaction and hence with higher formate concentration and longer duration of mixing, the homogeneity of the formate in the electrolyte improves over time.

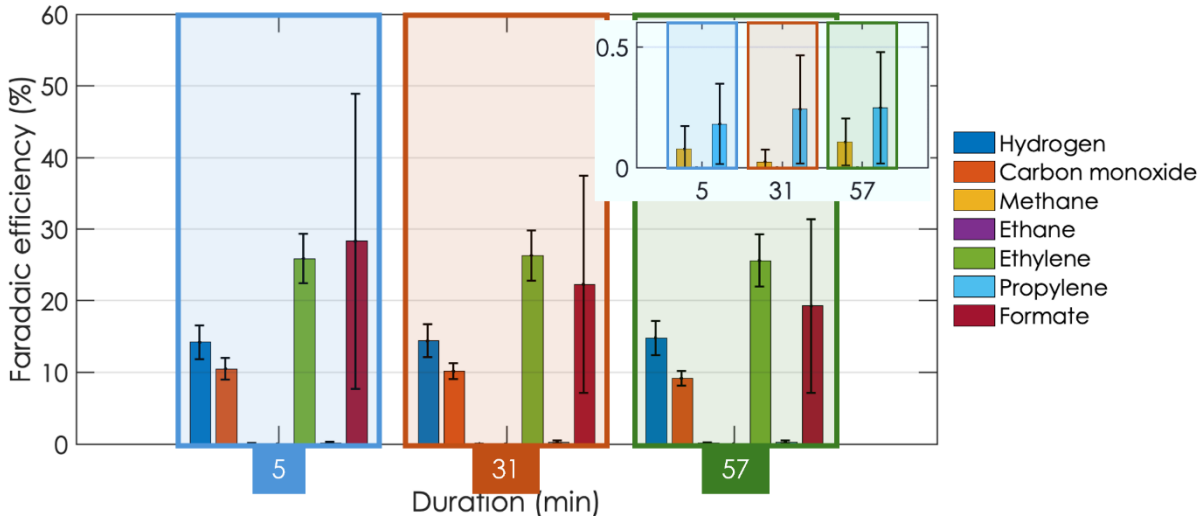

Figure 4-2. Partial faradaic efficiency of the electrochemical reduction experiment of Cu_2O gas diffusion electrodes. Gaseous products were measured by gas chromatography (hydrogen (H_2), carbon monoxide (CO), methane (CH_4), ethane (C_2H_6), ethylene (C_2H_4), propylene (C_3H_6)) and ionic products measured by ionic chromatography (formate (CHO_2^-)). The coloured bars show mean values and the error bars show standard deviation calculated from 5 samples. The inset shows a zoom of small faradaic values for the different sampling durations. The eCO2RR was conducted at at -1.17 V vs. RHE and 1M KOH was used as the catholyte.

The alcohol products (methanol, ethanol and n-propanol) were investigated with GC. Unfortunately, due to complications in the infrastructure it was difficult to perform enough measurements for an error calculation and hence only one experiment is shown in Figure 4-1a. Only ethanol was detected at sampling times of 31 and 57 min. Interestingly, longer eCO2RR durations produced a higher faradaic efficiency for ethanol production, which might either result from improving catalytic efficiency, or more likely from experimental limitations, such as detection limit and/or inhomogeneous mixing.

Figure 4-1b shows the total faradaic efficiency as calculated from all detection methods of a single Cu_2O sample. Ethanol increases in faradaic efficiency. No methanol or n-propanol was detected. The products do not add up to 100% faradaic efficiency as theoretically they should if all current measured during the chronoamperometric measurement is utilized for product

formation. Likely, the missing faradaic efficiency results from either errors in product analysis or possible side reactions such as Cu(I) reduction to metallic copper. The detection protocol for liquid products has the largest error as demonstrated by the large standard deviation of

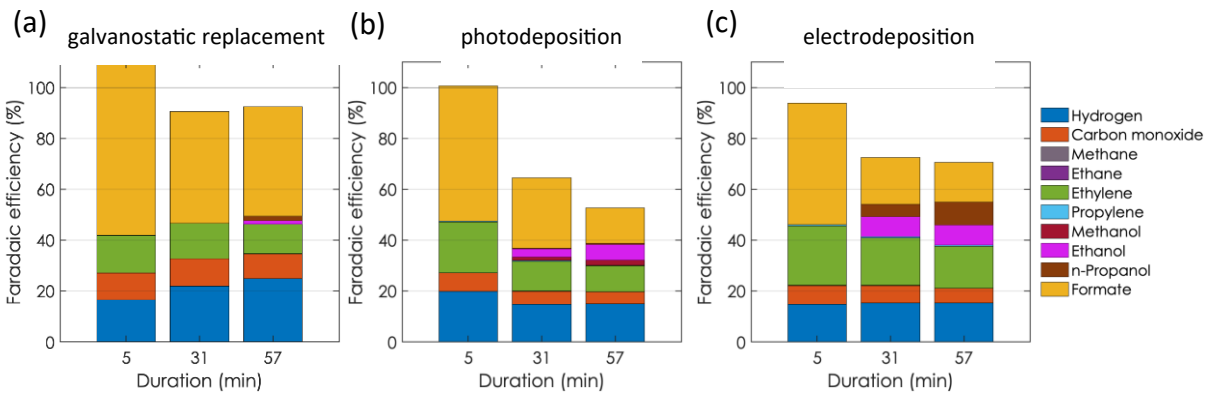

Figure 4-3. Stacked bar charts of faradaic efficiencies measured for Au-Cu_2O samples where gold was deposited via galvanostatic replacement (a), photodeposition (b), or electrodeposition (c).The eCO2RR was conducted at at -1.17 V vs. RHE and 1M KOH was used as the catholyte.

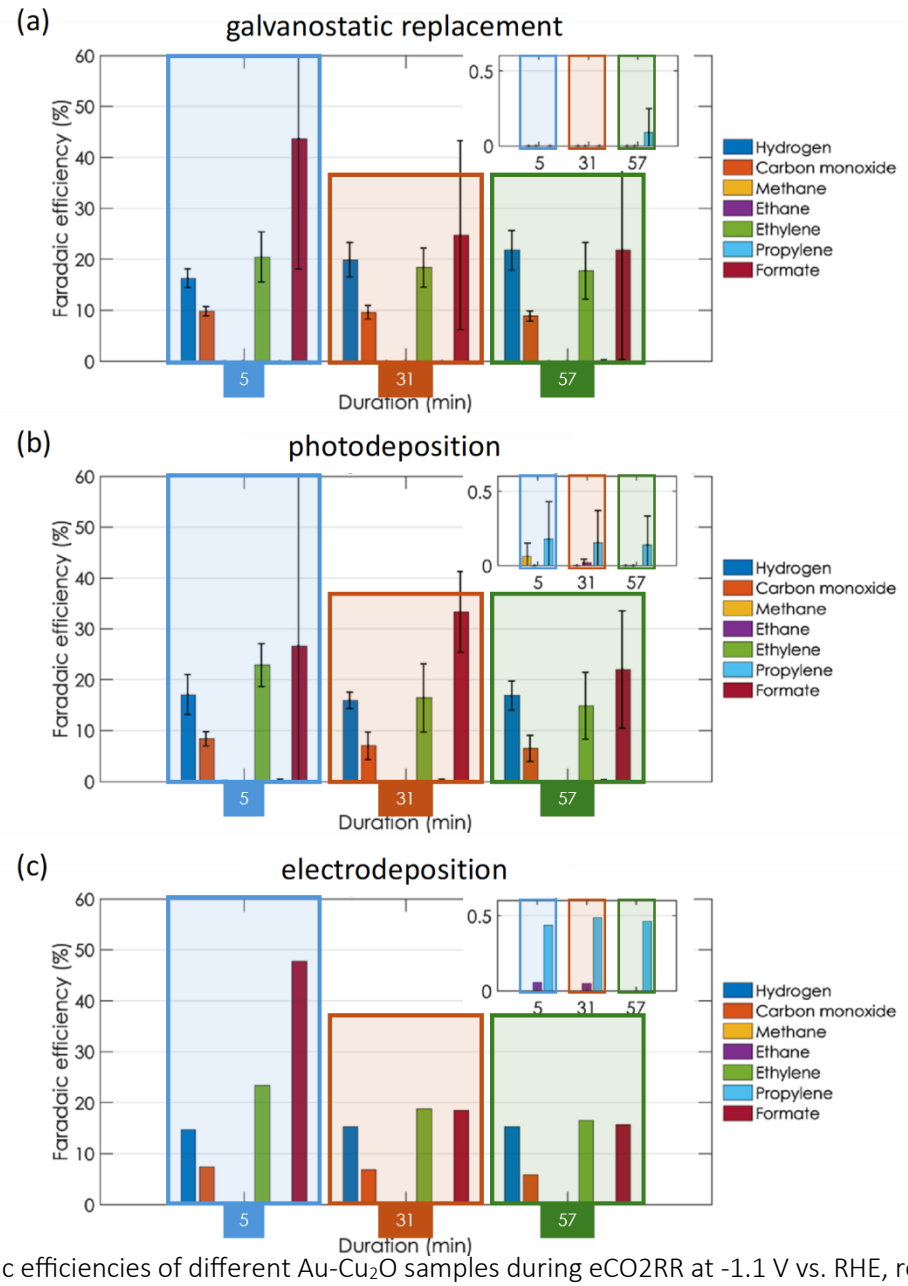

Figure 4-4 Faradaic efficiencies of different Au-Cu_2O samples during eCO2RR at -1.1 V vs. RHE, reference electrode used is RE-61AP, counter electrode was Pt mesh. Catholyte used was 1M KOH. Insets shows trace products i.e. those with less than 0.5% faradaic efficiencies. Gold was deposited via galvanic replacement (a), photo deposition (b), or electrodeposition (c). To ensure accurate results, for (a) and (b) the error bars show a standard deviation calculated from 5 measurements and the bars show the average result. The eCO2RR was conducted at at -1.17 V vs. RHE and 1M KOH was used as the catholyte.

the liquid-phase product. Hence, it is likely to account for the less than 100% faradaic efficiencies.

An improvement in set-up would be to encourage more mixing in the catholyte chamber and/or the electrolyte reservoir to observe whether more homogenous concentrations of liquid products can be achieved and hence lower the standard deviation between different samples. This could be achieved by a stirring bar in the reservoir chamber and/or catholyte chamber. Alternatively, the catholyte chamber could be redesigned with different geometries to create different flow dynamics to encourage mixing, such as the use of a turbulence flow promoter.[129]

4.2.2 Evaluation of $AuCu_2O$ GDE catalyst for eCO2RR

The product selectivity data is then used as benchmark to subsequently quantify the enhancement of gold as a cocatalyst. The faradaic efficiencies of respective gaseous and liquid products were calculated via GC and IC. To ensure accurate results, the measurement was repeated 5 times. Note that due to experimental limitations, GC of liquid products could only be performed on a smaller data set and is thus not shown here. Individual bars of the gaseous products of the Au-Cu_2O samples are shown for gold deposited via: galvanostatic replacement (Figure 4-4 a)), photodeposition (Figure 4-4b)), and electrodeposition (Figure 4-4c)). When

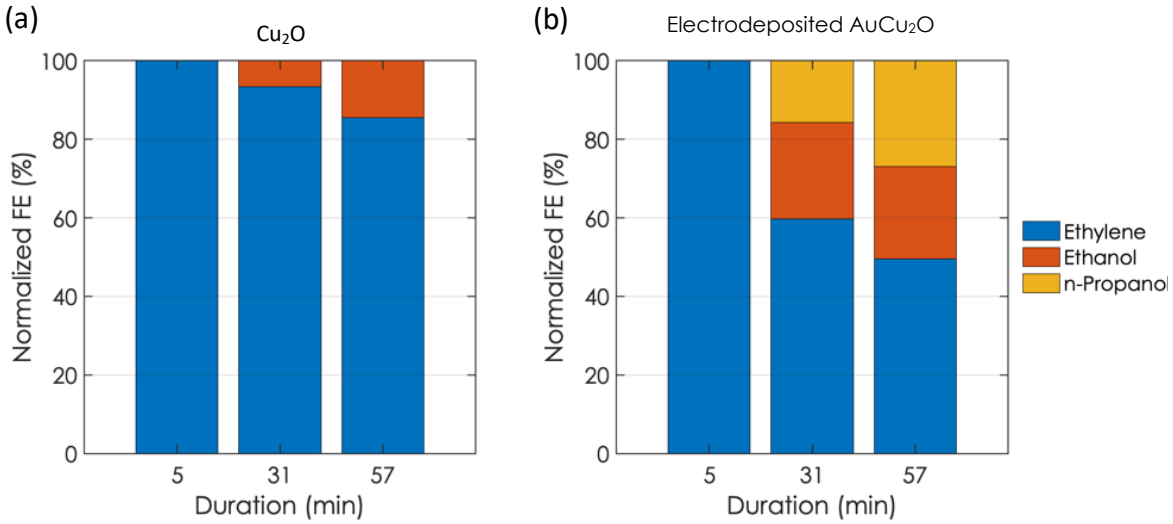

Figure 4-5. Normalised Faradaic Efficiency. Only products of the C2 pathway are shown (see red pathway in **Error! Reference source not found.**) and normalized to 100%. Two catalysts are shown, Cu_2O without (a) and with (b) electrodeposited gold. The eCO2RR was conducted at at -1.17 V vs. RHE and 1M KOH was used as the catholyte.

the faradaic efficiencies of Au-Cu_2O were compared with Cu_2O samples, several noticeable differences became evident. A significant decrease of faradaic efficiency of ethylene was observed, from 28% in the Cu_2O sample to 18% in the electrodeposited Au-Cu_2O sample. The amount of propylene detected increased from 0.25% in the Cu_2O sample to 0.5% in the Au-Cu_2O. The trace amounts of methane detected from the Cu_2O sample were not present in the Au-Cu_2O sample. Instead, trace amounts of ethane were detected in the electrodeposited Au-Cu_2O sample whereas no ethane was detected for the Cu_2O sample. The deviations indicate a product distribution towards longer chain carbon products. The most significant amounts of ethane was observed for the electrodeposited gold sample.

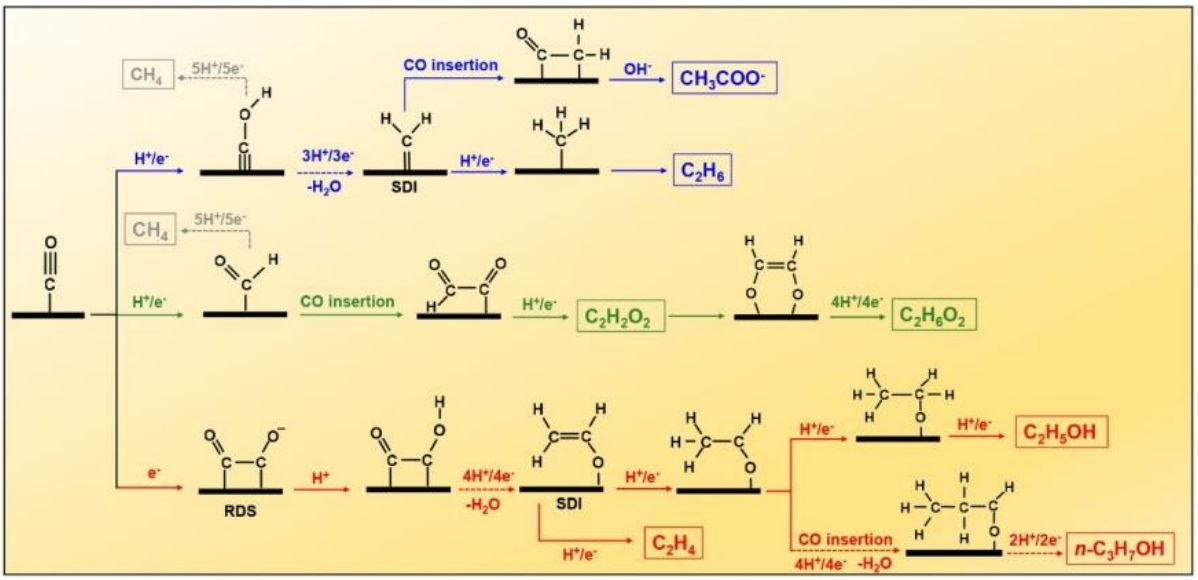

Figure 4-6 The C2+ pathways from a *CO adsorbed intermediate. The red pathway shows the steps to ethylene, ethanol and n-propanol. The rate determining step is the coupling of the *CO with another *CO.[201]

In Figure 4-3, the stacked bar chart shows the total faradaic efficiency. This includes liquid products measured via GC, that could be performed for these measurements. Notably, the largest amount of longer chain carbon products (ethanol, n-propanol) was observed for electrodeposited Au-Cu_2O samples, indicating that Au aids in the formation of longer chain products. In contrast, no n-propanol, a C3 oxygenate, was evolved via the Cu_2O sample. The n-propanol pathway is shown in Figure 4-6 (red) and involves the intermediate ethylene, which is produced in significant quantities both by Cu_2O and Au-Cu_2O catalysts.

Interestingly, methanol was only produced by the photodeposited Au-Cu_2O sample (see Figure 4-3b) with a faradaic efficiency of 1.5% and 2.0% after 31 min and 57 min, respectively. No methanol was produced by the Cu_2O sample or the electrodeposited Au-Cu_2O. This

indicates that the pathway for methanol may be unique to the photodeposited Au-Cu_2O, possibly due to the morphology or quantity of deposited gold. An increase in methanol production is also seen with Cu-Au alloy nanostructured catalysts when compared to metallic copper.[130]

To conclude, these results suggest that the presence of gold does enable CO insertion leading to a bifurcation of the reaction pathway. Also, for all Au-Cu_2O samples at 5 min sampling, there was no formation of ethanol or propanol. This indicates that this is not an instantaneous process upon the application of potential at the start of the chronoamperometry. A time-dependent process may be required, such as *CO coverage.

Figure 4-5 compares the normalised faradaic efficiencies of the Cu_2O sample and the $AuCu_2O$. It shows the different ratio of products from the n-propanol formation pathway (ethylene, ethanol, n-propanol) shown in Figure 4-6 (red pathway). The data is normalised to 100% to allow an easier comparison of product distribution and not product quantities. Cu_2O sample shows a 100% normalised FE to ethylene at 5 min, as does the Au-Cu_2O sample. At 31 min, ethanol was produced in the presence of Cu_2O electrocatalyst in an ethylene:alcohol ratio of 93:7, whereas the $AuCu_2O$ sample produced both ethanol and n-propanol in an ethylene:alcohol ratio of 3:2. At 57 min, the ratio of ethylene:alcohol for Au-Cu_2O changed to 1:1, demonstrating a high FE of the C2 and C3 alcohols (ethanol and n-propanol). In contrast, for the Cu_2O sample, the ratio of ethylene:alcohol was at 9:1 at 57 min, indicating a much higher preference to the ethylene pathway in the presence of Cu_2O. This experimental data supports the idea that *CO insertion becomes more favourable in the presence of Au in the sample.

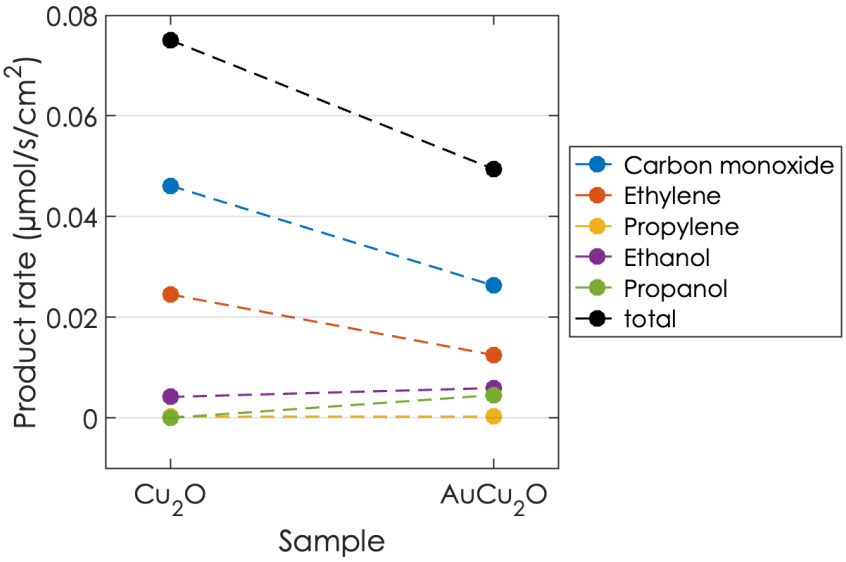

Figure 4-7 Production rate of products of CO2 reduction of Cu2O and Au-Cu2O sample (electrodeposited). The products are all those included in the red pathway of Figure 4-6, including the common intermediate carbon monoxide. The eCO2RR was conducted at at -1.17 V vs. RHE and 1M KOH was used as the catholyte.

DFT calculations suggest that higher CO coverage lowers the activation barrier for CO dimerization, which is considered the rate-determining step. [131] However, when the reaction pathway bifurcates towards ethylene or ethanol, higher CO coverage favours the formation of oxygenated products. Consequently, increased CO coverage on a catalyst surface reduces the faradaic efficiency of ethylene in favour of ethanol. [125]

This trend is reflected in the production rates of C_2+ products. As shown in Figure 4-7, Cu_2O exhibits a higher ethylene production rate than electrodeposited Au-Cu_2O, whereas Au-Cu_2O has a higher production rate of oxygenated products such as propanol and ethanol. These results align with previous findings that higher *CO coverage enhances selectivity toward oxygenated products over ethylene.

Further work could be conducted to confirm that higher *CO coverage is occurring on the Au-Cu_2O surface with respect to Cu_2O. For example, surface enhanced infrared absorption spectroscopy (SEIRAS) is sensitive to C-O containing adsorbates.[132] With this technique, *CO has been confirmed as a common intermediate.[133]

In Figure 4-7, the production rate of carbon monoxide of the Au-Cu_2O sample is lower than that of the Cu_2O. Despite the presence of Au which has a preference towards CO, the low production rate of carbon monoxide indicates that some carbon monoxide produced is utilised in the production of longer chain carbon products. This is consistent with the findings of Strasser et al.[134] who reported on selectivity differences found due to CO_2/CO co-feeds. However, they found an enhancement in ethylene production rate with the inclusion of CO gas in the gas feed. They concluded that there were separate catalyst sites for CO_2 and CO molecules, which could enable an increase in production of ethylene. This is inconsistent with the findings in this study. However, the previous study did not report the production of any oxygenated C2+ products. This could be due to the influence of the electrolyte used, (0.1M $KHCO_3$ at pH = 6.8) and the H-cell.

In this research, acetate was not tested for. Acetate is formed during CO electroreduction when hydroxide ions can react with intermediates,[134] as shown in the blue pathway in Figure 4-6. In the case of CO_2 electroreduction, the reaction between CO_2 and hydroxide ions minimises the concentration of hydroxide ions available to react and form acetate. However, for completeness it would have been useful to confirm that acetate was not present with ion chromatography.

4.2.3 Comparison of product selectivity of GR $AuCu_2O$ and Cu_2O

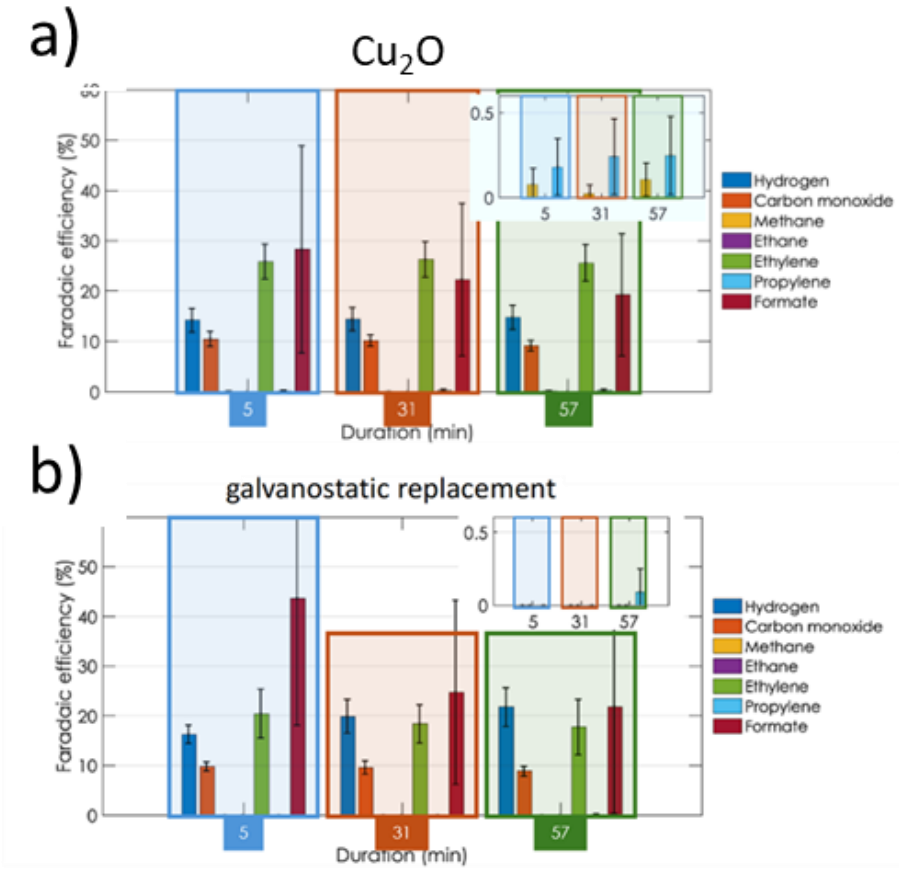

Figure 4-8 Comparison of faradaic efficiencies of a) Cu_2O and b) GR $AuCu_2O$

In Section 3.2.3.1 , the characterisation of Cu_2O and GR $AuCu_2O$ were discussed. EDX found the atomic percentage of gold to be 71% in the GR $AuCu_2O$ and 22.4% of Cu. Whereas in the Cu_2O sample, the atomic percentage of copper was 76% and the atomic percentage of oxygen was 16.7%. The faradaic efficiencies towards formate was higher in the GR $AuCu_2O$ than Cu_2O. As shown in Figure 4-6, the pathway to formate is via a CO insertion from a $*CH_2$ adsorbate. Hence as gold favours facile CO production, it is plausible that with high *CO concentration pathways with *CO insertion steps will in turn be favoured. However due to the reduced availability of copper due to the presence of gold, there is less ethylene produced as the activity

of *CO coupling will be lower. Hence why the faradaic efficiency for ethylene is greater for the sample of Cu_2O.

The faradaic efficiency for the parasitic reaction of hydrogen evolution (HER) is lower for the GR $AuCu_2O$ sample than the Cu_2O. This is likely again due to the higher content of gold and lower content of copper in the GR $AuCu_2O$. The lower hydrogen evolution on gold compared to copper is primarily due to its weak hydrogen adsorption energy, higher overpotential, and less favourable electronic structure for HER.[135]

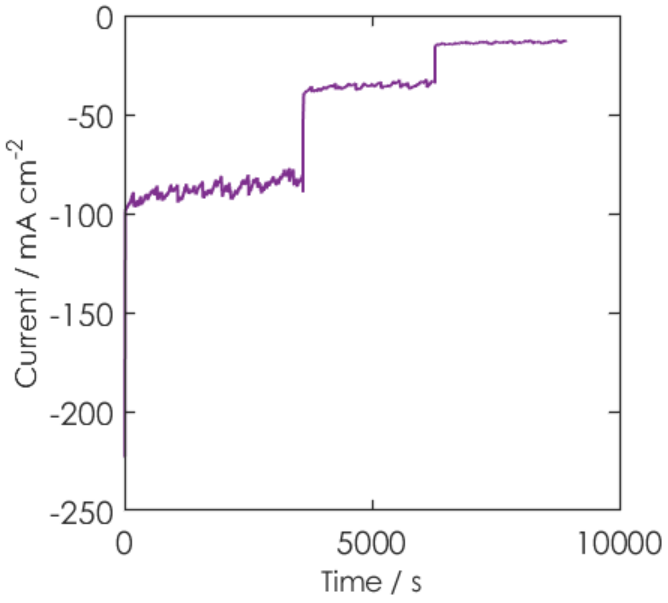

Figure 4-9 Chronoamperometry of a flooding sample of Cu_2O at -1.17 V vs. RHE in 1M KOH. The flooding events can be seen with the significant deviation in current.

The measurement shown in Figure 4-9 exemplifies flooding that was observed when running samples for longer than 1 h. A significant decrease in the magnitude of current was observed due to the loss of availability of the reactant CO_2 when pores within the catalyst layer became

flooded. Due to this observed instability in the gas diffusion electrodes, research was initiated to prevent the flooding of the gas diffusion electrodes.

4.3 Conclusion

The chapter discusses the evaluation of catalytic selectivity for the electrochemical CO_2 reduction reaction (eCO2RR) using hierarchically structured Cu_2O microparticles with gold deposition. The research found that Au-Cu_2O catalysts show superior production rates for oxygenate products like ethanol and propanol compared to Cu_2O alone, which is better at producing ethylene. This difference is attributed to the degree of *CO surface coverage, with Au facilitating higher *CO coverage and promoting the oxygenate pathway.

The chapter concludes with suggestions for further research to confirm these findings, highlighting the potential of bimetallic catalysts in improving the production rates of the eCO2RR towards valuable multi-carbon products.

4.4 Experimental & Methods

4.4.1 Cu_2O Catalyst Synthesis and Film Preparation

Cu_2O microparticles were synthesised by hydrolyzation and chemical reduction of copper acetate (Sigma Aldrich, 99.8%) with glucose (anhydrous, Sigma Aldrich) as previously published.[136] The ratio of water(mL):ethanol(mL) was 10:70. The microparticles were washed in ethanol and water before being separated via centrifugation (6000 rpm, 30 min). The particles were then dried under Schlenk conditions at 80°C for 48 h.

4.4.2 Gas Diffusion Cell Setup

The gas diffusion electrodes (GDE) were prepared by spraying catalyst ink on to the gas diffusion layer (H2315 I2 C6, Freudenberg). The catalyst ink was prepared by dispersing 10 mg cm^{-2} Cu_2O microparticles within 100 µL cm^{-2} of isopropanol and 17 µL cm^{-2} (Nafion suspension, 5 wt%, Sigma Aldrich). The ink was sonicated for 20 min upon the addition of the microparticles to isopropanol and then a further 15 min when the Nafion binder was added. The ink was then sprayed onto the commercial gas diffusion layer that was heated on a hotplate at 45°C.

4.4.3 Au Deposition on Cu_2O GDEs

Electrodeposition was chosen to reduce gold onto a Cu_2O-GDE by running chronoamperometry for a Cu_2O-GDE in a solution of $HAuCl_4$ to reduce Au^{3+} to metallic gold on the surface of the Cu_2O GDE. The electrochemical set-up was a 3-electrode cell, with Cu_2O GDE as working electrode, a Pt wire as counter electrode, and an Ag/AgCl reference electrode. The electrolyte was 2 mM $HAuCl_4$ in 1M KCl (aq). CV and CA measurements were performed with an Autolab potentiostat. Different optimizations were carried out to optimize the experiment: Different counter electrode sizes were employed to prevent current limitations. An anion exchange membrane was employed with an adapted H-cell that had the ability to sandwich a membrane between the anolyte and catholyte.

Photodeposition was performed with a 100 W xenon lamp with a 2 mM $HAuCl_4$ solution and with methanol as sacrificial electron donor. The pH was controlled via the addition of NH_4OH(aq), as reported in literature.

4.4.4 Product analysis

The products of the eCO2RR experiments were analysed via various techniques (GC and IC) as discussed in the Methods section. To calculate the faradaic efficiency, the average applied current during the electrocatalytic experiment was required. This was obtained by calculating the mean of current over the respective measurement time.

Gas Products (GC). Gaseous products (hydrogen (H_2), carbon monoxide (CO), methane (CH_4), ethane (C_2H_6), ethylene (C_2H_4), propylene (C_3H_6)) were investigated via gas chromatography (Shimadzu Nexis GC-2030, ShinCarbon Micropacked Column) that was connected to the gas side of the measurement cell. To quantify the product areas measured by the GC, a calibration gas mixture was measured prior to the experiments. The amount of a specific product in the gas stream $x_{p,GC}[ppm]$ can be calculated as follows:

$$x_{p,GC}[ppm] = \frac{a_{GC}}{a_{GC,STD}} \cdot c_{STD} \qquad (4\text{-}1)$$

where a_{GC} is the measured GC area of a specific product gas, $a_{GC,STD}$ is the measured GC area of the standard gas for that product, and c_{STD} is the concentration of product in the standard gas mixture. To calculate the product formation rate $R_{p,GC}$, the amount of product x_p had to multiplied by the GC injection gas flow rate F_{GC}:

$$R_{p,GC}\left[\frac{mol}{s}\right] = \frac{x_{p,GC} \cdot F_{GC}}{V_m} \cdot c_{STD} \qquad (4\text{-}2)$$

where V_m is the molar volume of gas at standard conditions ($V_m = 22.4\,l/mol$ at 0°C and 101.325 kPa). Utilizing Farad's equation, the product formation current $I_{p,GC}$ can be calculated:

$$I_{p,GC}[A] = R_{p,GC} \cdot z \cdot F \quad (4\text{-}3)$$

where F is Faraday's constant ($F = 96{,}485.332\ C/mol$). The amount of transferred electrons to reach the respective product during electrochemical reduction starting from CO_2 is given with z. This value was extracted from literature and is given in Table 4-1. With this, the partial faradaic efficiency of a product $FE_{p,GC}$ can be calculated by comparing $I_{p,GC}$ to the measured electrochemical current at the chosen potential I_{echem}:

$$FE_{p,GC}[\%] = \frac{I_{p,GC}}{I_{echem}} \quad (4\text{-}4)$$

This faradaic efficiency can be related to a specific product in the sampling gas stream and hence is not an overall faradaic efficiency of the experiment. To quantify all gaseous products, this calculation has to be performed for every individual product.

Table 4-1. Amount of transferred electrons z during eCO2RR to produce respective gaseous products from the reactant CO_2. Products from the gas phase were analysed via GC.

Product	**Amount of transferred electrons z**	**Reference**
Hydrogen (H_2)	2	[128]
Carbon monoxide (CO)	2	[128]
Methane (CH_4)	8	[137]
Ethane (C_2H_6)	14	[137]
Ethylene (C_2H_4)	12	[137]

Propylene (C_3H_6)	18	138

Liquid products Besides gaseous products, the eCO2RR experiment also produced liquid products that the electrolyte was sampled at different stages of the reaction for measurements. Products (methanol (CH_4OH), ethanol (C_2H_5OH), n-propanol (C_3H_7OH)) were investigated via gas chromatography (Shimadzu Nexis GC-2030, DB-Wax column). The details of this technique are discussed in the methods section. Importantly and in contrast to the GC analysis technique discussed above, this measurement did not provide a rate at a specific measurement time, but rather a product concentration that resulted from the accumulated product in the reactor after the measurement. Thus, when sampling, GC provided a product concentration $x_{p,GC\ lp}[ppm]$. With knowledge of the reactor volume V the molar amount of product $m_{p,GC\ lp}\ [mol]$ produced during the reaction can be calculated:

$$I_{p,GC\ lp}\ [A] = \frac{m_{p,LC}}{t} \cdot z \cdot F \qquad (4\text{-}6)$$

$$m_{p,GC\ lp}\ [mol] = \frac{x_{p,LC}}{1{,}000} \cdot \frac{1}{M_p} \cdot V \qquad (4\text{-}5)$$

where $M_p[g/mol]$ is the molar mass of the respective product. Note that this equation requires equal densities of solvent (i.e., water) and product, which is reasonable since the product concentration is very low.

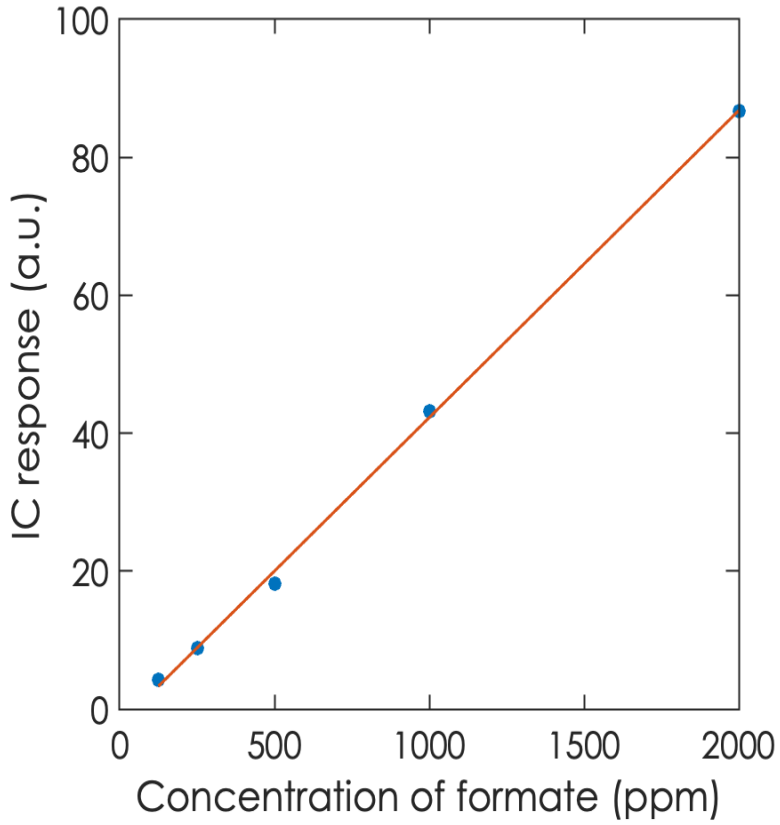

Figure 4-9. Calibration curve of the ion chromatograph for formate concentration measurements. Five test solutions (aqueous 1M NaOH with respective formate concentration, ranging from 125 to 2,000 ppm) were measured and a linear fit was performed on the IC response results, leading to a slope and respective IC calibration coefficient of 0.0445.

An average product formation current, $I_{p,GC\ lp}$ can now be calculated via the farad equation:

$$I_{p,GC\ lp}\ [A] = \frac{m_{p,LC}}{t} \cdot z \cdot F \qquad (4\text{-}7)$$

where t is the duration of the experiment. The amount of transferred electrons z per reduction reaction are extracted from literature and given in **Error! Reference source not found.** 4-1. This calculation requires a constant product formation, which is a reasonable assumption. Analogous to the analysis of the GC data, the average partial faradaic efficiency $FE_{p,GC\ lp}$ can be calculated from the average product formation current:

$$FE_{p,GC\ lp}\ [\%] = \frac{I_{p,GC\ lp}}{I_{echem}} \qquad (4\text{-}8)$$

Ionic products (IP) The liquid products were furthermore analysed with ion chromatography (Eco IC, Metrohm) to extract the concentration of formate (HCO_2^-) that was produced during the reaction. The details of this technique are discussed in the methods section. Analogous to the liquid products analysis, this technique operates in batch mode as sampling occurs at the end of the reaction.

The sensitivity of the ion chromatograph was measured by obtaining a calibration curve with stock solutions consisting of an aqueous 1M NaOH solution that contained different amounts of formate. The results of the calibration curve are shown in Figure 4-9 and yield a calibration factor $CF_{IC}[1/ppm]$.

Using this calibration coefficient, the molar amount of product $m_{p,IC}\ [mol]$ can be calculated from the IC value of the sample $x_{p,IC}$ as follows:

$$m_{p,IC}\ [mol]\ = \frac{x_{p,IC}}{CF_{IC}} \cdot \frac{1}{1{,}000} \cdot \frac{1}{M_p} \cdot V \qquad (4\text{-}9)$$

where M_p is the molar mass of formate. Analogous to GC measurements, the average product formation current $I_{p,IC}$ can be calculated as follows:

$$I_{p,IC}\ [A] = \frac{m_{p,IC}}{t} \cdot z \cdot F \qquad (4\text{-}10)$$

The amount of transferred electrons during the electrochemical reduction reaction are extracted from literature. The partial faradaic efficiency of formate production can be calculated via:

$$FE_{p,IC}\,[\%] = \frac{I_{p,IC}}{I_{echem}} \qquad (4\text{-}11)$$

Overall faradaic efficiency. To quantify the overall faradaic efficiency of the experiment, the sum of all partial faradaic efficiencies must be calculated:

$$FE[\%] = \sum_{p_{gas}} FE_{p_{gas},GC} + \sum_{p_{liquid}} FE_{p_{liquid},LC} + FE_{p_{formate},IC} \qquad (4\text{-}12)$$

All gaseous products quantified via GC are given with p_{gas} and all liquid products quantified via GC are given with p_{liquid}. Since there is only one product of IC analysis; the IC product is termed $p_{formate}$. Note that ideally if all electrons of the electrochemical experiment are utilized for CO_2 reduction product formation, the overall faradaic efficiency should reach 100%. Experimental limitations as well as unwanted side reactions (such as catalyst degradation) may reduce the overall faradaic efficiency to below 100%. This is discussed further in the results discussion of this chapter.

5

Using capacitance as a measure to investigate wettability of nanoporous carbon particles surface functionalised with polyfluoroaromatics for eCO2RR

Ella Fidment, Viola Birss, Eileen Yu, Elizabeth Gibson

Abstract

This research delves into the differential hydrophobicity performance of functionalized colloid imprinted carbon materials under varying electrochemical potentials. The focus is on their applications in analogous electrochemical carbon dioxide reduction reaction conditions (eCO2RR). Employing cyclic voltammetry and chronoamperometry, the study thoroughly evaluates these materials in different potential windows. The results reveal a distinct variation in hydrophobicity between CIC85 and PhF_5CIC85, specifically at positive potential windows near their open circuit potential (OCP). A key finding is the observed variation in the hydrophobicity of PhF_5CIC85, which exhibits notable changes in behaviour at different potentials, highlighting the material's dynamic response to electrochemical conditions. This study

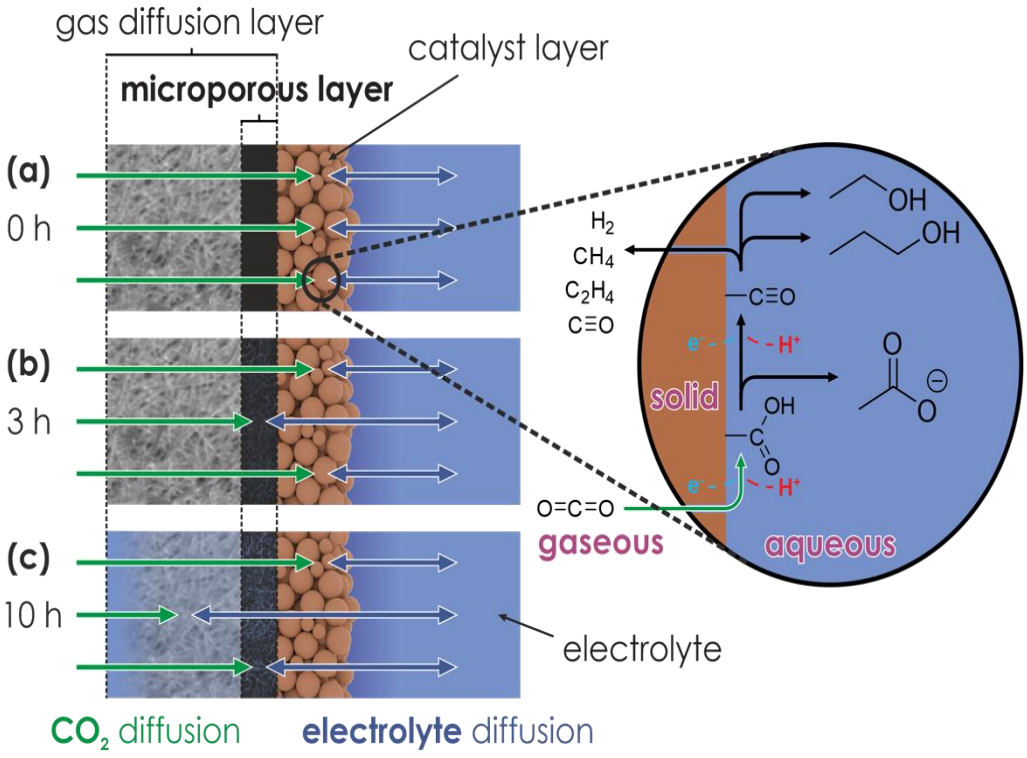

Figure 5-1. Concept of flooding affecting a gas diffusion electrode. The cathode consists of a gas diffusion layer, which allows the reaction gas CO_2 to diffuse to the active material, i.e., copper particles. At the same time the product gases diffuse through the layer and are subsequently detected via GC. Liquid products remain in the electrolyte (see inset). To prevent electrolyte to flooding the reactor and decreasing gas permittivity of the gas diffusion layer, a microporous layer is deposited in between this layer and the catalyst. (a) An efficient operation of the microporous layer prevents any flooding and no electrolyte reaches the gas diffusion layer. (b) A partial flooding causes a reduction in the CO_2 reaction gas flux, reducing the product yield. (c) Significant flooding prevents an efficient operation of the gas diffusion layer.

provides essential insights into the influence of electrochemical environments on the hydrophobic characteristics of fluorinated aromatic molecules bonded on nanoporous carbons, offering valuable implications for optimizing their performance in eCO2RR.

5.1 Introduction

A significant advance in the technology for eCO2RR was the use of a gas diffusion electrode (GDE) set-up at the cathode side of the electrolyser. A GDE is made up of 2 layers: the gas diffusion layer (GDL) and the catalyst layer (CL).[139] The gas diffusion layer is itself typically formed of two layers: a macroporous substrate (MPS) and a microporous layer (MPL). The role of the GDL is to transport reactant and product gases between the gas chamber and the catalyst layer, as well as conducting electrons to and from the catalyst layer.[68] Typically the MPS is made of conductive carbon fibre or titanium foam[140] and provides mechanical strength, conductivity and macropores for gas transport. There is a triple phase interface at the catalyst layer where the catalyst is the solid phase, the electrolyte is the liquid phase (providing a source of protons for the reaction), and the reactant CO_2 is the gaseous phase.[141,142]

The GDE's value is that it significantly improves the availability of CO_2 at triple phase reaction site as shown in Figure 5-1. Prior to the use of gas diffusion electrodes, H-cells were used for eCO2RR research. In a H-cell set-up, CO_2 would be dissolved in the electrolyte. However, CO_2 has poor solubility in aqueous solvents and at higher alkalinities it reacts with hydroxide ions to form carbonate species,[70] as shown below in Equation 1-3.

$$CO_{2\,(g)} \rightleftharpoons CO_{2\,(aq)} \quad (1)$$

$$CO_{2\,(aq)} + OH^-_{(aq)} \rightleftharpoons HCO^-_{3\,(aq)} \quad (2)$$

$$HCO^-_{3\,(aq)} + OH^-_{(aq)} \rightleftharpoons CO^{2-}_{3\,(aq)} + H_2O_l \quad (3)$$

Furthermore, gas diffusion electrodes improve CO_2 availability and mass transport to the triple phase interphase, as well as mass transport of the gaseous products. Overall, this helps increase reaction rate, leading to higher current densities.[143]

A stability issue of GDEs is the intrusion of electrolyte into the GDL due to electro-osmosis.[72] This detrimental process reduces the pore space available for CO_2 transport and hence, reduces the product selectivity of carbonaceous products relative to the hydrogen evolution reaction.[70] When pores of the microporous layer become blocked, CO_2 must diffuse through electrolyte to reach the catalyst layer. This increases the probability that CO_2 will react with OH^- to form carbonate or bicarbonate aqueous species. The solubility of these salts in aqueous electrolyte is low. Thus, in the eCO2RR gas diffusion conditions, water evaporates and these salts precipitate in the pores of the GDL. Due to their hygroscopic nature, they draw in electrolyte via capillary forces and increase electrolyte intrusion.[71] To counteract this detrimental effect, hydrophobic materials such as PTFE are sprayed onto carbon-based GDLs, but over time this degrades under the cathodic current. Furthermore, PTFE has unfavourably low conductivity and itself occupies pore space.[70] At present, this phenomena is affecting the stability of the GDL, reducing the selectivity of the reaction and hence there is opportunity to engineer solutions to prevent the flooding of the gas diffusion electrode.

Catastrophic flooding is common[144] and can happen within an hour of operation of the GDE. Water droplets, which form as a result of flooding, can be imaged with an optical microscope.[72]

Nafion is a cationic ionomer formed of perfluorovinyl ether groups terminated by sulfonate groups bonded to a PTFE backbone.[145] Nafion is the standard binder used in the catalyst layer and hence its use is widespread throughout the CO_2 electroreduction GDE research field with at least 39 papers published in the last 5 years.[146–148] However, beyond CO_2 electroreduction, Nafion is used in gas diffusion electrodes for proton-exchange membrane fuel cells (PEMFC),[149] sensors,[150] and catalysis of environmental pollutants.[151] Therefore, the number of literature published regarding Nafion and gas diffusion electrodes totals almost 1000 papers. Nafion can increase hydrophobicity of the catalyst layer due to the hydrophobic groups of the backbone chain[152] but has also been found to increase proton availability via a shuttle mechanism by the sulphonate groups.[153,154] Small variation in Nafion content in the catalyst has been found to alter selectivity of Ag catalyst from carbon monoxide to formate.[155] Whilst the optimal amount of Nafion was found to be dependent on the amount of catalyst loading and the GDL used, too much binder would block the pores of the GDL and reduce the availability of CO_2.[156] Using aprotic, organic solvents can alter the polymerisation and agglomeration of Nafion within the catalyst layer.[157] Alternatively, some groups have used Nafion as a separate film on the catalyst layer to create a hydrophobic covering that is capable of limiting HER and promoting CO_2 reduction to CO.[158] A key achievement in the research field was the spray-casting of Nafion over catalyst layer to extend the triple phase boundary to enable the reduction of CO_2 to ethylene at 45% faradaic efficiency with a current density of 1300 mA cm^2.[159] Recent modelling work has found that Nafion-coated electrodes possess a higher surface area charge density, which can help promote C_2H_4 production.[160]

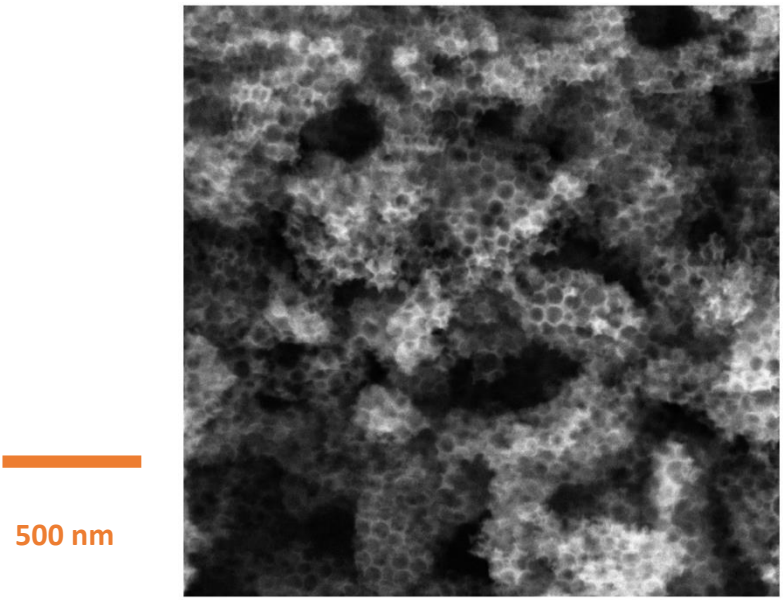

Figure 5-2 SEM image of the CIC-85 with secondary electron detector

In this work, the wettability of uniform nanoporous carbon particles was investigated electrochemically with the overall goal of using these particles within the catalyst layer of a gas diffusion electrode to increase the degree of hydrophobicity within the catalyst layer. Subsequently, the carbon particles were functionalised with a hydrophobic molecule to form a hydrophobic monolayer and their wettability was again measured electrochemically. Professor Viola Birss and her group developed a method for the synthesis and functionalisation of the colloid imprinted carbons(CICs).[161] Their work had previously demonstrated the CIC's use in fuel cells, where humidity plays a key role.[162,163]

In this chapter, the method typically used to calculate electrochemical surface area (ECSA) has been optimised for these materials, It enables a correlation of ECSA to the electrowettability of these materials, providing insight into their suitability for GDEs. The notable findings of this research was the difference in capacitance at high potential windows of the CIC85 and

the PhF_5CIC85, providing quantifiable surface area difference between two materials that are structurally the same but have different hydrophobicities. This quantifiable surface area also corresponds well to the measured BET area, enabling a calculation of percentage of surface area that was wetted. After the application of a chronoamperometric bias at 0.025 V vs. RHE, capacitance was measured at a lower potential window of 0.0-0.4 V vs. RHE. A substantial increase in capacitance was observed for the PhF_5CIC85, indicating a presumed decline in hydrophobicity due to electrowetting. Potential explanations for this behaviour were examined and are presented below.

5.2 Results and Discussions

5.2.1 Experimental Design

Colloid imprinted carbons (CICs) were synthesised via silica templating as described in Methods 2.3.2. Silica particles serve as a templating agent for the carbon pitch and subsequently are dissolved. Hence, the size of the silica dictates the nanopore size of the carbon material.

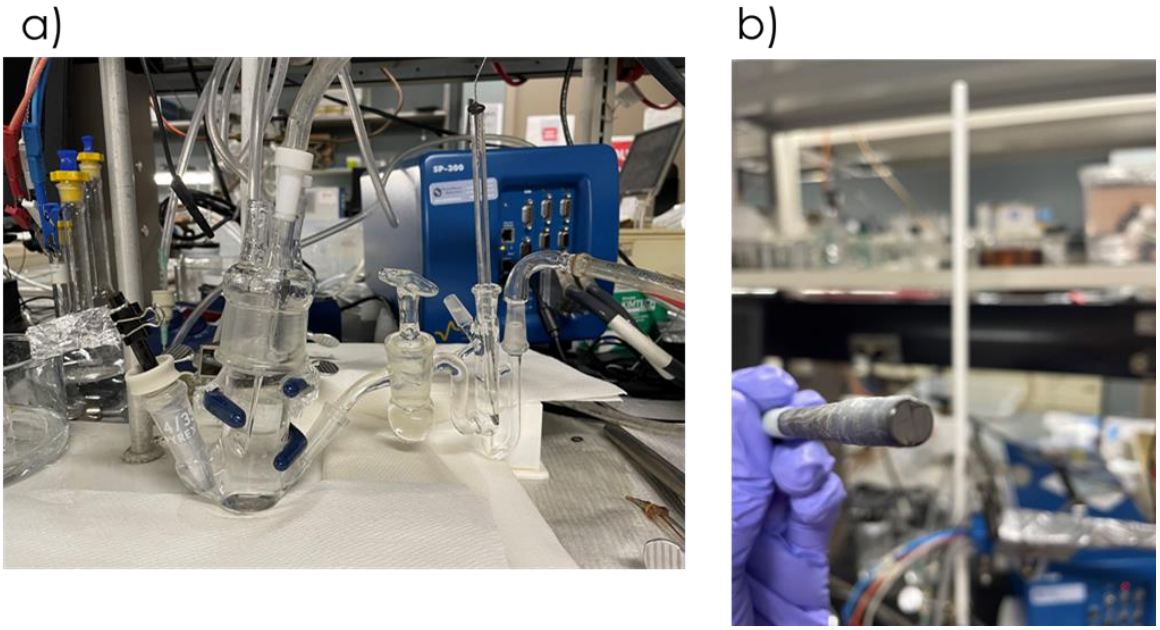

Figure 5-3 a) Glassware set-up, involving a cell with angled glass outlets close to the base of the cell, an RHE reference electrode set-up in 0.1M KOH B) angled view of the front of the glassy carbon electrode, post-polish with the shaft wrapped in paraffin film.

Silica particles with 85 nm diameter were used and the colloid imprinted carbon has corresponding nanopores of 85 nm and is referred to as CIC-85. The synthesis method produces particles of CICs with uniform pores of 85 nm as is evidenced in Figure 5-2.

The selection of a nanopore size of 85 nm of the CICs was deliberate, aiming to ensure a homogeneous functionalization of the nanopore surfaces. Previous research by the Birss group

has successfully synthesized CICs with smaller nanopores (down to specifically 22 nm) for applications in fuel cells.[164] However, it was observed that steric hindrance posed a challenge, impeding the access of reactant molecules for subsequent functionalization within the 22 nm pores. Consequently, with the objective of maximizing the inner surface area functionalization of these CICs, a nanopore size of 85 nm was purposefully chosen and synthesized. The functionalisation of the CIC85 occurred via in situ diazonium reduction reaction with pentafluorophenylaniline as described in Methods 2.3.3 to create a modified CIC material. Henceforth, it will be referred to as PhF_5-CIC85.

To enable the study of the hydrophobic properties of the CICs, an experimental set-up and electrochemical procedure was designed. A piece of glassware was designed and made to have 3 angled glass inlets for the working electrode, reference electrode and counter electrode. This was to enable the glassy carbon electrode and the CIC film to be angled almost vertically within the electrolyte. If any gas bubbles exist or are formed in-situ electrochemically, they will be able to leave a vertical surface more easily. Furthermore, it enables the reference electrode to sit extremely close to the working electrode to minimise the iR drop.

A simple experiment was devised by drop-casting ink containing CIC, Nafion and water onto a glassy carbon rod and measuring the capacitance within different potential windows both pre and post chronoamperometry. During eCO2RR experiments, the catalyst layer is deposited on commercial GDL via spray deposition. The morphology of the GDL is very rough and hence possesses a high electrochemical surface area that could also contribute to the measured capacitance in scanrate dependent CVs of the carbon particles. Hence, a smooth glassy carbon electrode surface was chosen to provide a smooth surface.

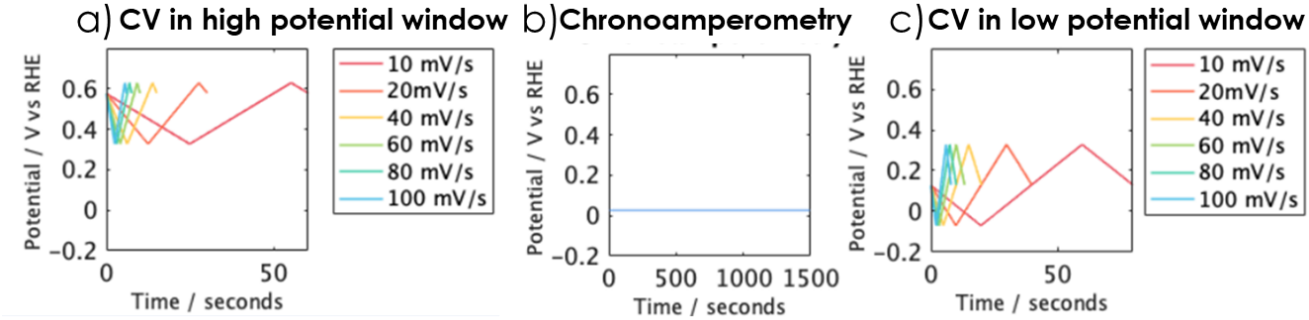

Figure 5-4 Potential versus time representation of the electrochemical testing for capacitance. A) The first measurement is a CV at different scan rates (10mV/s – 140 mV/s) in 0.1M KOH, with a Hg/HgO in 1M KOH reference electrode with a graphite counter electrode. The electrolyte was de-gassed with argon. The CV window was 0.4 – 0.7 V vs. RHE and the starting potential was 0.55 V vs. RHE. B) The second step was a chronoamperometry at 0.05 V vs. RHE applied for 1500 s. This was conducted to mimic more negative potentials used in eCO2RR, however without applying potential lower than 0 V vs. RHE to avoid the evolution of H_2 bubbles due to water splitting which could disrupt the measurements. C) Third and final measurement was CVs at different scan rates like step 1, however at a lower potential range (0.0-0.4V vs. RHE).

The shaft of the glassy carbon rod was wrapped in paraffin film and similar ECSA measurements were undertaken to verify that the shaft was not in contact with the electrolyte. A graphite counter electrode was chosen instead of a metal counter electrode to prevent the possibility of metal contamination on the working electrode.

The aim of the research was to study the performance of these materials under conditions identical, if not similar to eCO2RR conditions. Nafion was used as the binder within the film, as it typically is used during the catalyst layer for eCO2RR. The electrolyte chosen for these studies was 0.1M KOH because 1M KOH is used in the eCO2RR experiments referred to earlier in this thesis. A lower concentration of 0.1M KOH was used in this work due to the reactivity of high concentrations of KOH with glass over extended periods of time.[165]

Various parameters in the cyclic voltammetry measurements were adjusted to enhance the precision of capacitance measurements for the examined materials. Detailed guidance for this optimisation process was provided in the paper by Morales and Risch (2021).[166] For example, the "potential window" (i.e. the difference between the maximum and minimum potential applied during the cyclic voltammetry) was widened. This modification was undertaken to accommodate potential delays in the current response of the sample, particularly when high scan rates are employed due to the elevated resistance.

Secondly, the potential windows of the cyclic voltammetric and chronoamperometric measurements were dictated by the electrolyte stability window of 0.1 M KOH. To ensure all recorded current of the samples were from non-faradaic contributions only, all measurements were kept above 0 V vs. RHE. The potential was calculated from pH and respective standard potential of the reference electrode (Hg/HgO in 1M KOH, RE-61AP).

The electrochemical measurement protocol involved 3 separate electrochemical measurements as shown in Figure 5-4: CVs at multiple scan rates at a high potential window, chronoamperometric measurements, and CVs at multiple scan rates at a low potential window. Ultimately, the aim was to probe the capacitance behaviour at different potentials.

The first measurement was a cyclic voltammetry at a high potential window (0.4-0.7 V vs. RHE) at different scan rates (10 mV/s – 500 mV/s). This potential window was chosen as 0.7 V vs. RHE was situated in between the measured open circuit potential (OCP) of CIC85 film and the PhF_5CIC85 at 0.8 V vs. RHE and 0.6 V vs. RHE, respectively. Hence, this potential window was chosen as it was close to the OCP of both materials and at the same time not too

high to cause oxidation of water, while still balancing the requirement of a large potential window.

The next electrochemical procedure was a chronoamperometric measurement that simulated the application of more negative potentials for eCO2RR. The working potential applied to the bimetallic catalysts in Chapter 4 of this thesis was -1.17 V vs. RHE. However, the reduction of water occurs at 0 V vs. RHE. Hence, to avoid the evolution of hydrogen gas that could

Figure 5-5 (next page) a) CVs within the 0.4-0.7 V vs. RHE window for CIC85 material drop cast onto a glassy carbon electrode from a water-based ink with an additive of Nafion. The scan rate varies from 10 mV/s to 140 mV/s overall. The reference electrode was a mercury based RE-61AP and counter electrode was a graphite electrode. The electrolyte was degassed with argon and was 0.1 M KOH. B) The current value of the CVs displayed in a) of this figure were extracted at 0.52 V vs. RHE and their absolute value was plotted. Both the forward (blue) and backward (orange) sweep is shown. A linear equation is used to fit this data, where y = ax + c. The gradient is presented for both the forward and backward sweep. The R^2 values are shown to evaluate fit quality. C) The CVs of the PhF_5CIC85 material are shown here with the same experimental conditions as discussed for a). D) The current values were extracted at 0.52 V vs. RHE from Figure C). E) The calculated values of capacitance per mass are shown. Capacitance is calculated as an average of the forward and backward gradient values, shown as a in Figure b and d. The mass used was the total mass of the material used (CIC85 = 11.58 mg, PhF_5CIC85 = 11.73 mg) divided by the amount of catalyst ink pipetted onto the glassy carbon electrode (28 mL) as ratio of the total amount of catalyst ink (1.4 mL).

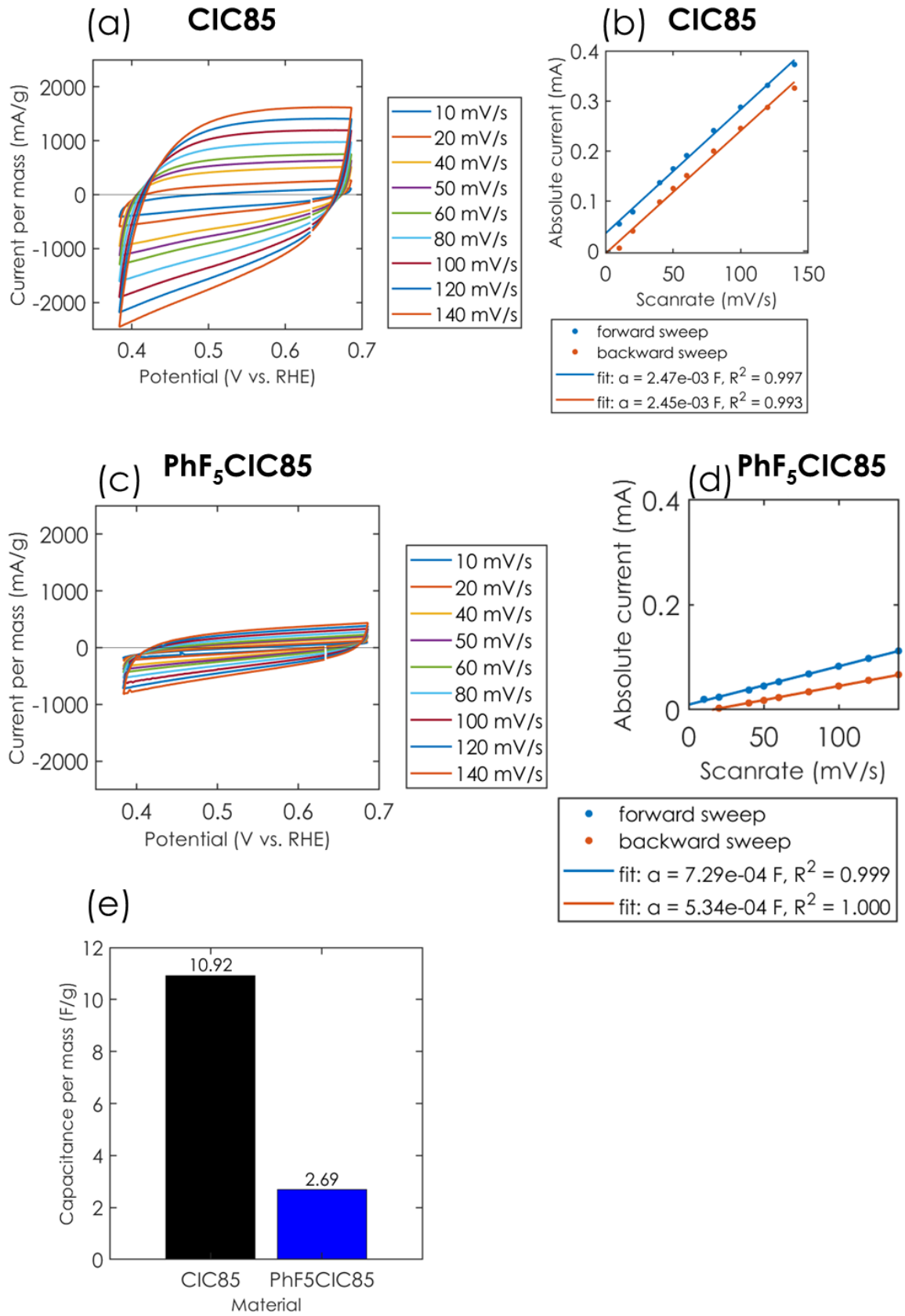

affect the capacitance measurements, the chronoamperometric procedure was ran at 0.025 V vs. RHE for 15 min.

The final measurement was another cyclic voltammetry at different scan rates (10 mV/s – 500 mV/s) at a low potential window (-0.4 V vs. RHE). The aim here was to remain within a similar potential window as the chronoamperometric measurement, while still being able to measure capacitance.

5.2.2 Capacitance measurements on CIC85 and PhF_5CIC85

CIC85 and PhF_5CIC85 show different capacitances in a positive potential window

In the positive potential window of 0.4 – 0.7 V vs. RHE, the current per mass was higher for CIC85 than PhF_5CIC85, as shown in Figure 5-6 a) and c). Figure 5-6 b) and d) shows the analysis and fitting of the electrochemical surface area from Figure 5-6 a) and c). The capacitance per mass of CIC85 is approximately 4 times greater than that of the PhF_5CIC85. This aligns with the expectation that despite the materials having similar surface areas as calculated from BET, PhF_5CIC85is more hydrophobic due to the monolayer of PhF5, which results in less wetting and lower measured electrochemical surface areas.

Figure 5-6 (next page) a) CVs in different potential windows (0.0-0.4 V vs. RHE and 0.4 – 0.7 V vs. RHE) for the same CIC85 sample are shown. The scanrates vary from 10mV/s top 140 mV/s. The 0.4-0.7 V vs. RHE window CVs were conducted first. Then a chronoamperometry measurement at 0.05V vs. RHE was done. Then the 0-0.4 V vs. RHE window CVs were performed. The current is divided by mass of the material deposited onto the glassy carbon electrode (11.58 mg divided by 28 µL of catalyst ink deposited from the overall volume of catalyst ink created 1.4 mL). B) CVs in different potentials windows for the PhF_5CIC85 material. C) Capacitance per mass in the 0.4-0.7 V vs. RHE and 0.0 – 0.4 V vs. RHE window. These values were calculated by extracting the current values at 0.52V vs. RHE and plotting them against their respective scanrates. The gradient of the linear fit represents the capacitance. This value was then divided by the mass of the material deposited onto the glassy carbon electrode. D) The capacitance per mass of the PhF_5CIC85.

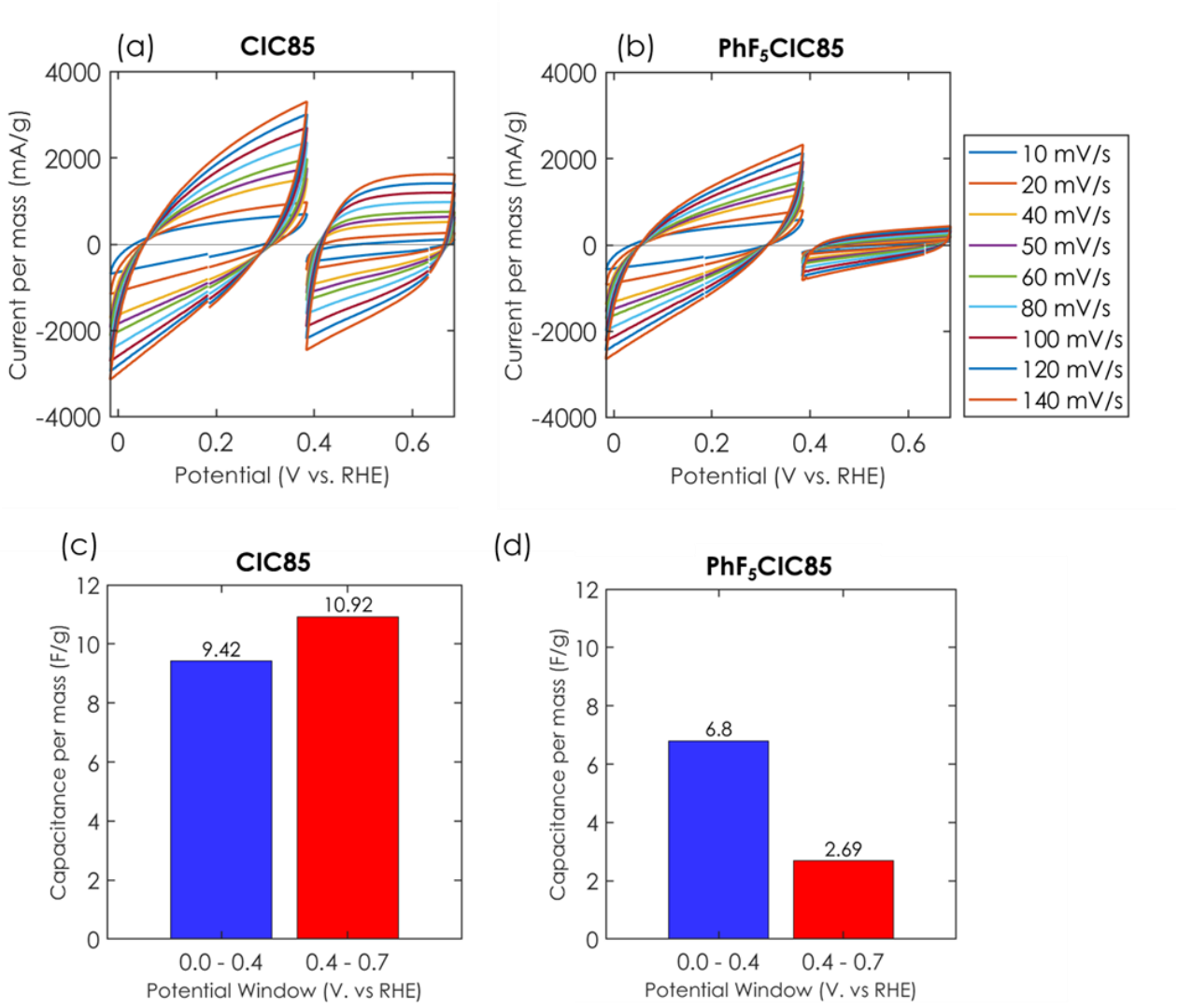

In lower potential windows, PhF_5CIC85 capacitance increases notably

In Figure 5-6 c) and d), the capacitance per mass is shown. Compared to CIC85, the capacitance per mass of PhF_5CIC85 sample doubles from 0.4-0.7 V vs. RHE to 0.0-0.4 V vs. RHE. The electrochemical surface area has thus doubled and it indicates a change in the sample in some respect. It could suggest that the hydrophobicity has decreased, or that the sample's morphology has changed through cracking of the sample film. This could be due to swelling and/or movement of Nafion when in contact with water and under potential bias.[167] If Nafion changes or moves, it could cause cracks in the film.

The capacitance per mass of CIC85 decreases from 10.92 to 9.42 F/g, which could represent real-term decrease in ECSA or alternatively could be due to the sample resistance increase at high scan rates, which cause deviation from the linear relationship between the scan rate and *capacitance magnitude.* The shape of the CVs in the 0.4-0.7 V vs. RHE window approach the shape of a rectangle with slightly curved corners at minima and maxima potential, whereas the shape of the CIC85 CVs in the 0.0-0.4 V vs. RHE window resembles a 'leaf'. The leaf shape is the result of the high scan rate leading to large resistance to ionic conductivity which has been previously modelled[168] and observed during electrical double layer experiments with other porous carbon materials.[169,170] This phenomenon is non-linear with scan rate as a greater effect happens at large scan rates.

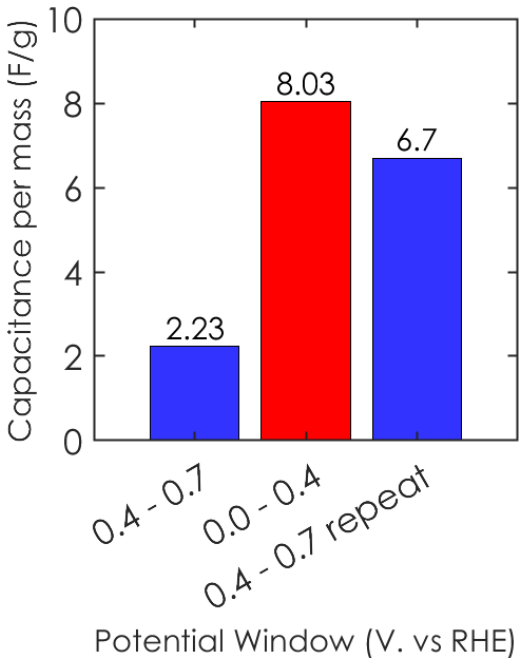

Figure 5-7 Capacitance per mass of PhF_5CIC85 sample. The capacitances were calculated by running CVs at different scan rates in 0.1M KOH in the different potential windows. The sample was tested in

0.4-0.7 window, 0.0-0.4 window and 0.4-0.7 window again. The blue represents the 0.4-0.7 window and the 0.0 – 0.4 window is represented in red.

The increase in capacitance for PhF_5CIC85 sample is irreversible

During measurements, when a sample underwent capacitance measurements in the 0.4-0.7 V vs. RHE window, the 0.0-0.4 V vs. RHE window, and finally the 0.4-0.7 vs. RHE window, the measured capacitance was high. This indicated that the process causing the increase in capacitance was irreversible. The capacitance measured in the 0.4-0.7 V vs. RHE repeat window was not as high as in the 0.0-0.4 V vs. RHE window. This could be due to a reduction in wetting at less biased (i.e., closer to the OCP) potentials with less electro-wetting force. This however, suggested that the process was partially irreversible. Alternatively, due to the resistance of the electrical double layer at fast scan rates, the currents generated in the less biased potential window could have been lower.

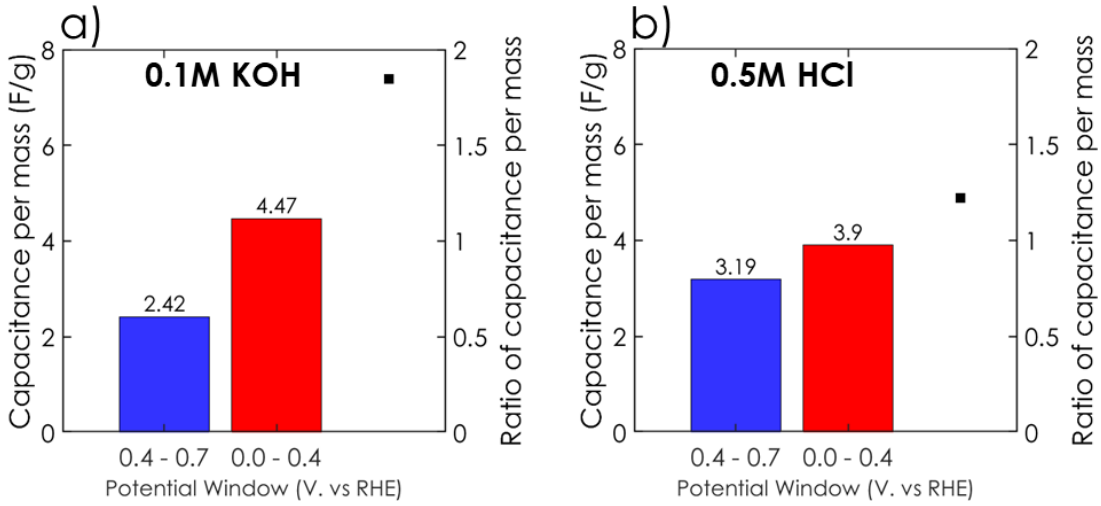

Figure 5-8 The capacitance per mass of PhF_5CIC85 sample in different electrolytes: a) 0.1 M KOH with RE-61AP reference electrode and graphite counter electrode. b) 0.5 M HCl with an Ag/AgCl reference

electrode and graphite counter electrode. Also shown on the secondary axis (right hand side) is the ratio of the 0.0-0.4/0.4-0.7 V vs. RHE window capacitance per mass.

In 0.5 M HCl, the capacitance of PhF_5CIC85 capacitance exhibits a comparatively smaller increase than in 0.1 M KOH

The capacitance of the PhF_5CIC85 sample was also trialled in 0.5 M HCl. From Figure 5-8, the capacitance of the PhF_5CIC85 sample in 0.5M was found to be higher in the 0.4 – 0.7 V vs. RHE window compared with the sample in 0.1M KOH electrolyte. However, the ratio of the 0.0 – 0.4 V vs. RHE window to the 0.4-0.7 V vs. RHE window is lower for the 0.5 M HCl sample compared to the 0.1M KOH electrolyte sample. The difference could arise from the different concentration of ions in solution: 0.5 M chloride ions and 0.1 M potassium ions. The concentration of potassium hydroxide of 0.1 M was chosen to be used as the standard because high concentrations of hydroxide solutions can react with glass over time.[165] A high concentration of HCl was used to reduce the ionic resistance of the electrochemical cell.

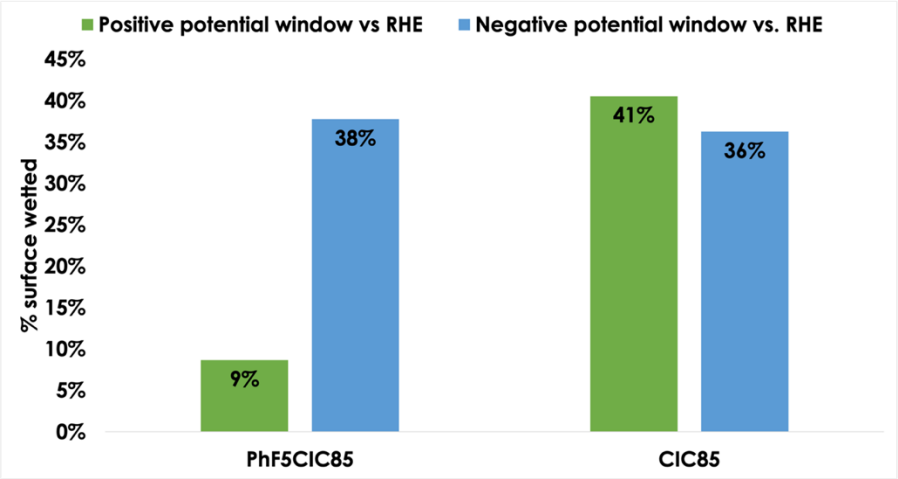

Figure 5-9 Percentage of surface wetted of the PhF_5CIC85 and CIC85 material as calculated by using surface area calculated from BET. The BET values are extracted from literature.[91]

To try to establish whether the capacitance measured by the technique outlined in this chapter produced data that was relevant to other physically quantified characteristics of the carbon material, a comparison was made between the surface area of the CIC85 and PhF_5CIC85 measured by Brunauer–Emmett–Teller (BET) theory. The surface area calculated by the capacitance experiments. It was found that the percentage of surface wetted of PhF_5CIC85 increased from 9% to 38% when going from the positive to negative potential window. Note that the percentage of CIC85 surface area remained constant from the positive to negative potential window.

5.2.3 Contact angle measurements

Contact angle measurements were trialled as a measure of hydrophobicity

After the capacitance measurements, work was conducted with other characterisation methods to attempt to measure the changes in hydrophobicity with alternative techniques to confirm our findings. Firstly, contact angle measurements were conducted to measure the

hydrophobicity of the drop-cast carbon discs. Water (5 mL) was dropped onto the disc and the contact angle was measured. In Figure 5-10, an image of the contact angle measurement is shown.

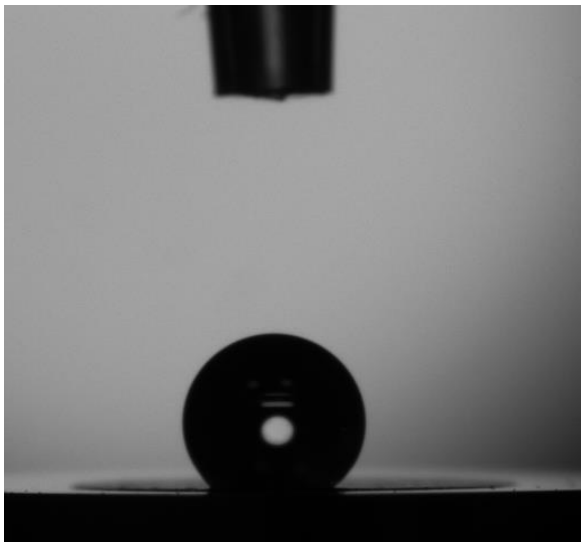

Figure 5-10 Droplet of water (5 µL) on the disc of a PhF_5CIC85 on a glassy carbon electrode. Contact angles are given in Table 5-1.

Table 5-1 Contact angle measurements of Figure 5-10.

	Left	Right	Average
Contact angle (degrees)	141.4	143.2	142.3

With the contact angle measurement, the contact angle of the water droplet to the PhF_5CIC85 disc surface is high (see contact angles in Table 5-1). Superhydrophobic surfaces are those with a water contact angle (WCA) greater than 150 degrees.[171] Hence the disc of PhF_5CIC85 has a WCA approaching that of a superhydrophobic surface. However, the above discussed hypotheses suggests that following the chronoamperometry and negative potential window

CVs, the hydrophobicity of the PhF_5CIC85 disc is lowered and should have a lower WCA after the electrochemical testing. However, as visible in Figure 5-11 the pressure of a water droplet sat on the surface of the PhF_5CIC85 disc post-electrochemical characterisation would make it crumble into pieces, which would then float around in the water. Ultimately the PhF_5CIC85 disc had experienced a number of harsh conditions of wetting, electrochemical bias cycling, 1M KOH electrolyte, and drying. Hence, it was not stable enough to be tested again. Alternatively, the electrochemical testing had caused physical changes in the film itself that resulted in the increase in capacitance and also caused the break-up of the film upon the application of water.

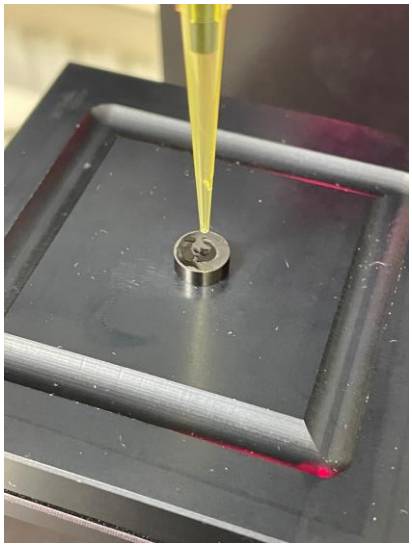

Figure 5-11 Image of PhF_5CIC85 disc on glassy carbon electrode broken under the force of placing a droplet of water on the surface.

Contact angle measurements were also conducted on CIC85 films as shown in Figure 5-12. The droplets on the film measured WCAs from 132° to 142.7°. The large variation in WCAs could be the result of variability in the film's morphology. Hence a profilometer was used to measured the variation in profile, as shown in Figure 5-13. The obtained profilometer data

results from one film measured at 3 different angles. The profilometer data shows that the height of the film is often highest at the edge of the film and that the profile of the film overall is spiky and jagged.

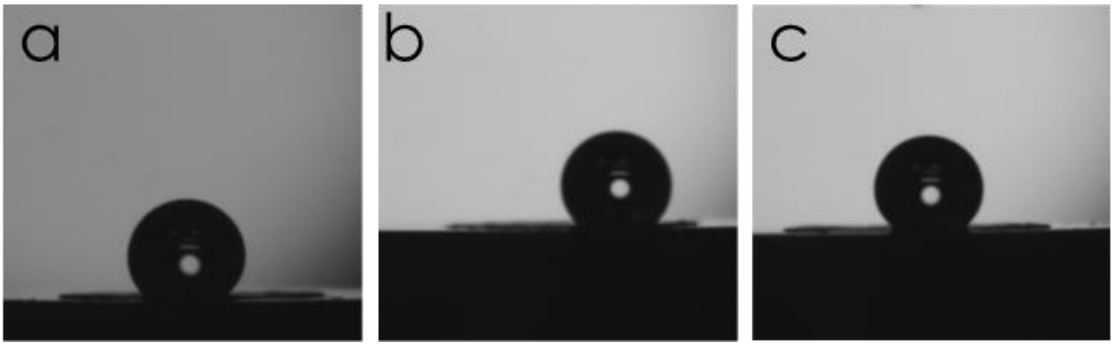

Figure 5-12 Contact angle images of 3 different 5 mL droplets of water on a CIC85 disc.

Table 5-2 Contact angle data of measurements displayed pictorially in Figure 5-12 on a CIC85 disc

	Left	**Right**	**Average**
Droplet 1	132.9	137.6	135.2
Droplet 2	138.7	139.2	141.8
Droplet 3	142.7	141.8	142.3

Considering that the maximum average value of WCA of the CIC85 film is 142.3°, which is equivalent to that of the PhF_5CIC85 film and close to the literature value of superhydrophobic surfaces, and that CIC85 is well-established as a hydrophilic material due to its terminal carbon-oxygen bonding suggests that the morphology and porosity of the CIC85 is contributing to its highly hydrophobic character towards a water droplet on its surface. Numerous studies have found that the combination of both nanometer and microscale scale roughness

contributes to the hydrophobicity of a material.[172] The micrometer roughness is shown by the profilometer in Figure 5-13, and the SEM images of CIC85 show that the 85 nm terminal holes in the carbon scaffold of the material cause the nanometer roughness. Hence, as a surface the CIC85 exhibits relatively low wettability when measured by a contact angle. However, as a film submerged in 1M KOH electrolyte and subject to electrochemical bias capacitance testing, the material exhibits poor hydrophobicity. It could be concluded that contact angle measurements are not a helpful measurement in elucidating the hydrophobic character of a film in aqueous electrolyte under potential bias.

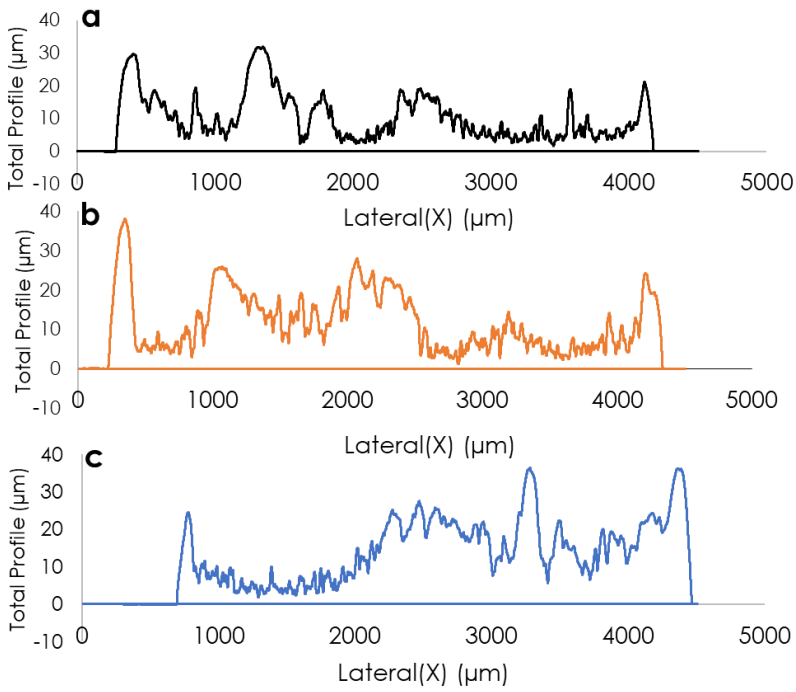

Figure 5-13 Profilometer data of CIC85 disc (cross-sections taken across 1 disc, rotated by 120° for each profile)

SEM imaging was employed to observe whether morphological changes to the PhF_5CIC85 occurred

A film of PhF_5CIC85 was studied under SEM, as shown in **Error! Reference source not found.**.

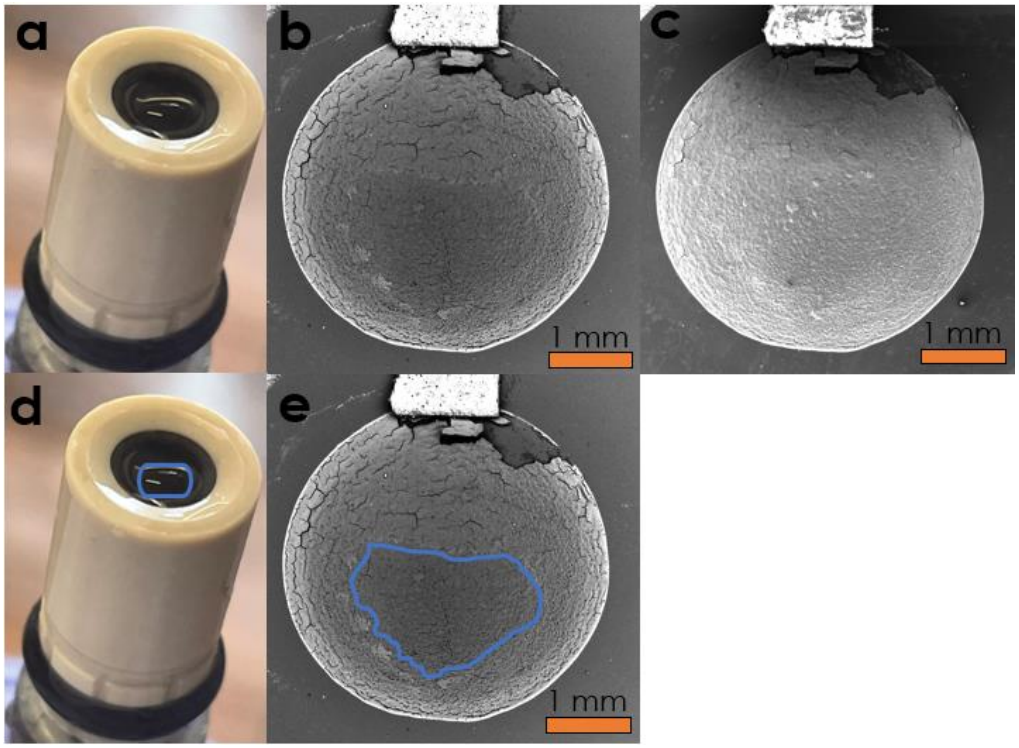

Figure 5-14 a) image of PhF_5CIC85 film on glassy carbon electrode in electrode holder b) SEM image of the PhF_5CIC85 disc post-electrochemical testing with a back scatter electron detector, with 5.0 kV accelerating voltage c) SEM image with secondary electrode detector d) same image as a) but the air bubble on the surface of the electrode is circled in blue, e) same image as b) however with a blue sketch where the air bubble sat during electrochemistry

In all previous work related to capacitance measurements, a 5 cm glassy carbon rod electrode was the electrode upon which all the films were drop-casted onto. In order for the films to be imaged in the SEM equipment, the glassy carbon rod was swapped for glassy carbon discs that were 0.5 cm in length and are electrically contacted within the electrode holder as seen in Figure 5-14a). The different architecture of the electrode (i.e. the rubber seal between the glassy carbon electrode and the plastic body of the holder and the plastic body itself) caused the electrolyte and air to behave differently to the surface of the PhF_5CIC85 film. Therefore, an air bubble formed on the surface of the electrode which could be seen in Figure 5-15a) and

is highlighted by a blue ring in in Figure 5-16 d) and in Figure 5-17e). The air bubble could not be replaced with electrolyte due to the highly hydrophobic character of the film and experiments were conducted regardless. But, overall, this provided an opportunity to measure SEM on a sample, which contained areas that had been in contact with electrolyte and undergone electrochemical testing, and a “clean” area in the centre of the film which had not. It was possible to image the surfaces of both areas and perform EDS.

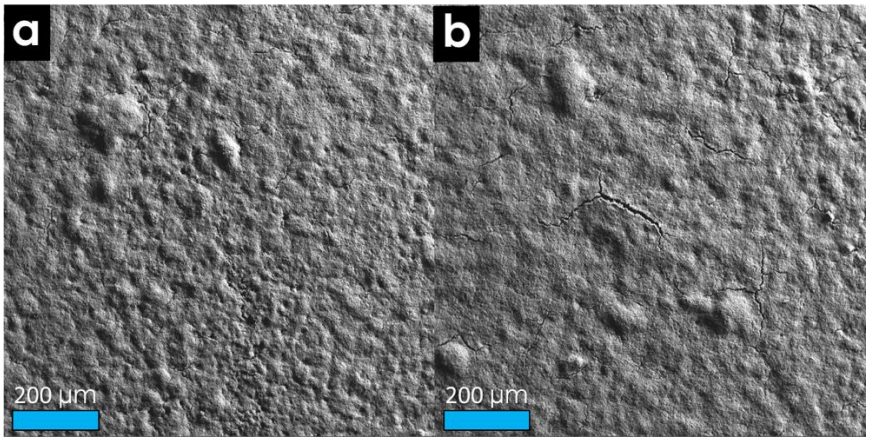

Figure 5-18 a) SEM image of a clean area of PhF_5ClC85 with back scatter detector, b) SEM image of an area with electrolyte contact with a back scatter detector

In Figure 5-19 b), the PhF_5ClC85 film is imaged with a back scatter electron detector. Therefore, the variation of brightness of the image is due to the different atomic number (Z) numbers of the elements present. The contrast between the elements presents elucidates the cracks present in the film. The white rectangle at the top of the image is tape that was used to help orient to the position of the clean area. Carbon has the smallest Z number of all the other known elements present in this sample and has therefore the lowest amount of scattering. Hence, it appears the darkest. The colour is largely darker in the centre, whilst the area around it is lighter, indicating heavier elements than carbon.

In Figure 5-20c) the same film is imaged with a secondary electron detector and hence the variation in brightness shows the topography of the sample. There is less variation in this image compared with Figure 5-21b), with the cracks appearing less pronounced.

Figure 5-18a) and Figure 5-18 b) show the "clean" area and the area of electrolyte contact of PhF_5CIC85, respectively. There are more visible cracks in the area with electrolyte contact, which could be generated in-situ during electrochemical conditions. However, no quantitative crack counting across multiple sites was undertaken due to time constraints with the SEM.

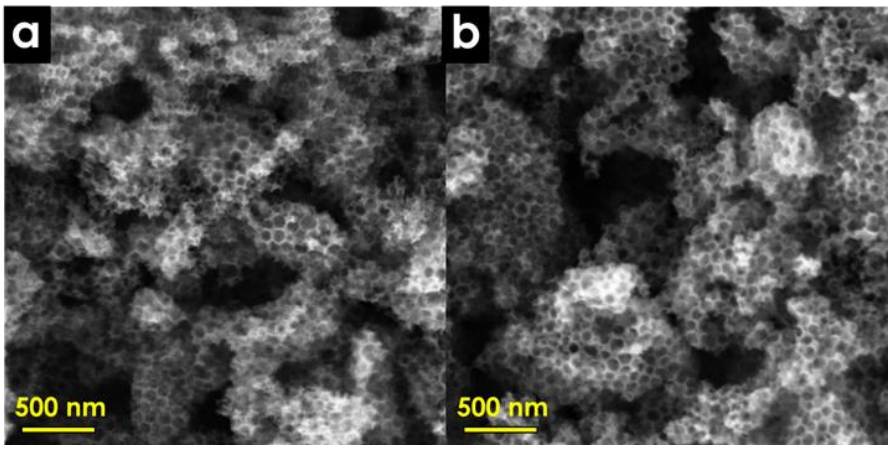

Figure 5-22 a) SEM image of a clean area of PhF_5CIC85. Image taken with a secondary with a secondary electron detector b) SEM image of an area of electrolyte contact. Image taken with a secondary electrode detector

In Figure 5-22 a) and b), SEM images on the order of scale of the 85 nm pores of the PhF_5CIC85 material were imaged to observe any morphological changes that could have happened on this magnitude of scale. From these images, it can be concluded that there is no visible difference.

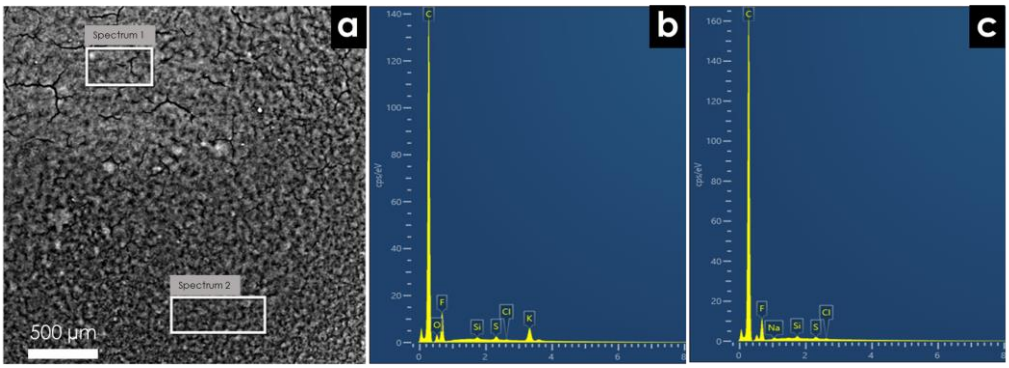

Figure 5-23 a) SEM on a boundary area where spectrum 1 of electrolyte area and spectrum 2 of clean area were taken for EDS were taken. B) spectrum 1 and c) spectrum 2

Table 5-3 Percentage of elements present in the spectrums of EDS as shown in Figure 5-23

Label	C	O	F	Na	Si	S	Cl	K	Total
Spectrum 1	81.80	4.88	11.31		0.14	0.28	0.06	1.53	100.00
Spectrum 2	88.38		10.86	0.24	0.22	0.22	0.09		100.00

In Figure 5-23 a), a SEM image of the boundary area is shown, where both the electrolyte contact area can be seen in the top left and the “clean” area can be seen in the bottom half. Similarly to Figure 5-18, more cracks can be observed in the electrolyte contact area. EDS was performed on the areas indicated and the spectrums are presented in Figure 5-23 b) and in Figure 5-23 c). In the area, which has come into contact with electrolyte, potassium and oxygen are present in the spectrum. Both elements can not be observed in the spectrum of the clean area. This indicates the presence of salts of KOH on the sample. The elements present due to Nafion, sulfur and fluorine are present in both samples. However potentially oxygen groups should have been observed in Spectrum 2 due to the presence of sulphonic groups

and the oxygen backbone. Silicon is present in small quantities due to the silica used during the synthesis process of the CIC.

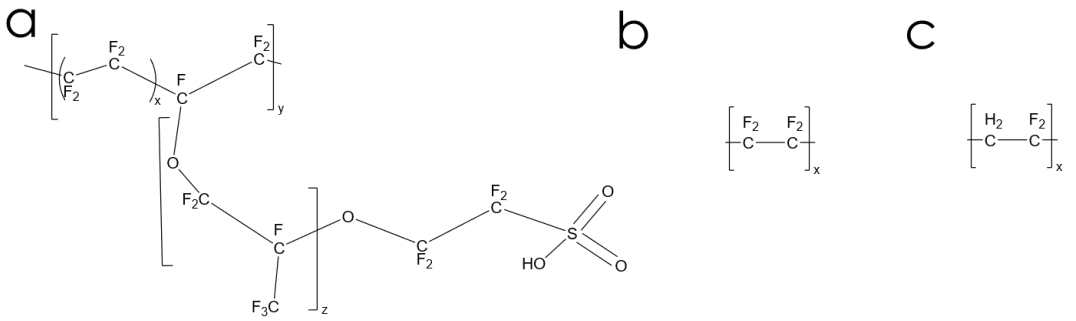

Figure 5-24 Drawing of the polymer structure of a) Nafion b) PTFE and c) PVDF

5.2.4 Hydrophobicity of different ionomers

With no significant signs for the dramatic change in hydrophobicity exhibited by the PhF_5CIC85 films when studied by SEM, research was done to investigate the performance of the film when the ionomer Nafion was replaced with a different ionomer. PTFE was selected not to be tested against Nafion, as PTFE does not dissolve in solution and requires temperatures of 300°C to melt. Instead, the synonymous polymer poly(vinyldene fluoride) (PVDF) was chosen, which is soluble in the organic solvent N,N-Dimethylacetamide (DMA). As in shown in Figure 5-24b) and c), instead of a repeated monomer of two CF_2 moieties, the PVDF monomer has one CH_2 and one CF_2. PVDF shows greater wettability than PTFE, but is less wettable than non-fluorinated compounds.[173] PVDF has fewer component monomers compared with Nafion, which contains perfluorether side chains ending with sulfonic acid groups.[121] Unlike PVDF or PTFE, Nafion is also capable of ion conduction, such as protons.[174] As a comparison,

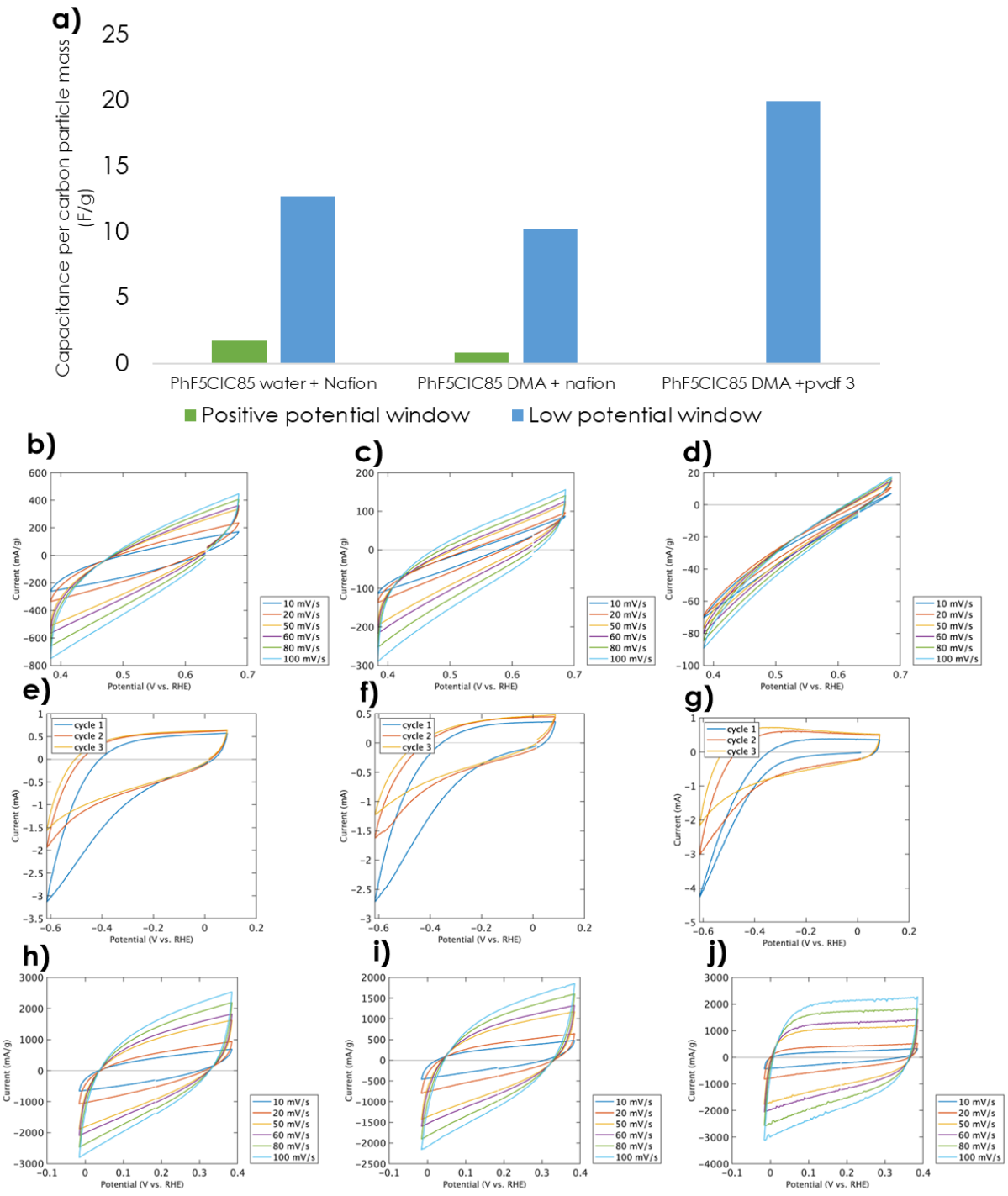

Figure 5-25 a) Capacitance per mass calculations of films made from a water based film with Nafion as a binder, DMA based film with Nafion as a binder and a DMA based film with PVDF as a binder. B, C and D show the respective samples in the positive potential window. E, F and G show the samples under negative potential windows and H, I and j show the low potential window CVs.

Nafion is also soluble in DMA. Hence, both ionomers can be compared within a film drop-cast from a solution.

In Figure 5-25 a), capacitance comparisons can be observed of PhF_5CIC85 with different binders: Nafion ionomers in water, Nafion ionomers in DMA, and PVDF in DMA. It was found that in the positive potential window the capacitance of the films decreases respectively. The respective CVs at different scan rates to calculate the capacitance are shown in Figure 5-25b-d). The CVd measured at a positive and negative potential window are shown Figure 5-25 e-g) and h-j), respectively. The capacitance (Figure 5-25 a)) was calculated from the negative potential range. A difference in capacitance of the samples, which both use Nafion but in different solvents (water and DMA), can be observed. However, the difference is not significantly and therefore there is no accounting for variation between samples for further measurements. An explanation for the observed variations could result from the use of different solvents, which could cause Nafion to arrange itself differently within the film. This is since Nafion has both hydrophilic parts of the backbone and terminal groups and also hydrophobic domains.[175]

When comparing PVDF and Nafion, Nafion has CF_2 moieties as well as perfloroether groups and sulfonic acid groups. In absence of the perfluoroether groups and sulfonic groups when PVDF is employed, one could expect to obtain a more hydrophobic film with lower capacitance. However, the opposite trend was observed in Figure 5-25 a), where PVDF and PhF_5CIC85 film had significantly higher capacitance than the Nafion sample. One explanation could result from the structure: In a beta crystalline structure, where fluorine and hydrogen atoms sit on opposite edges of a carbon backbone, a permanent dipole exists.[176] In the

presence of bias, the PVDF could exhibit piezoelectric effects that cause the film to crack and enable water to infiltrate throughout the film.

Despite this, the research provides evidence for the hypothesis that the ionomer plays a strong role in dictating the hydrophobicity and capacitance of the film. Furthermore, it raises questions about how ionomers react to potential bias under electrochemical conditions and how the ionomer arrange themselves within the film in response to the hydrophobic monolayer of PhF_5 on the carbon surface. Further investigation could be undertaken by studying the electrochemical impedance of these films and films of only the ionomer to study the conductivity of these ionomers in 1M KOH at different potentials.

5.2.5 Further discussion points

Recent research has demonstrated that a decrease in electrolyte concentration resulted in a highly asymmetric dependence of the apparent contact angle (CA), denoted as θ, on the applied potential (E) compared to the potential of zero charge (E_{pzc}).[177] When considering the position of the E_{pzc} of the CIC and PhF_5CIC85, the CIC85 was found to have a higher OCP than PhF_5CIC85 of ca. 0.8 V vs. RHE compared to ca. 0.6 V vs. RHE, respectively. Hence, when applying potential biases in the region of 0.0-0.4 V vs. RHE, the value of (E_{pzc} – E) is greater for the CIC85 than PhF_5CIC85. Whether this has any impact on the wetting would require further experiments in different potential ranges than were conducted in this research.

Furthermore, the increase seen by the Dryfe group of electrowetting with higher alkali metal ion concentration in electrolyte[177] would suggest that within the local electrolyte regime of a GDE where a significant increase in pH is observed due to the high concentration of hydroxide ions, a larger increase in electrowetting could be expected because of this.

This research was conducted based upon the assumption that the PhF_5 groups are hydrophobic and prevent wettability, however the wetting that we see at lower potentials could be due to a reduction in hydrophobicity of the PhF_5 group. C-F bonds exhibit hydrophobic properties due to the low polarizability of the C-F bond, since fluorine is small and the electron cloud is highly attracted.[178] Hence, this means that the C-F bond does not form temporary dipoles easily and therefore does not easily participate in van der Waals interactions with water. However, consideration should be taken to estimate how aromatic C-F bonds could change character when covalently bonded to a carbon electrode under potential bias. The effect of potential on functional groups bonded to electrodes has been researched in the field of organic catalysis[179] but the electro-inductive effect for electrowetting/hydrophobic surfaces has not been researched. The molecular synonym of this effect was first explored by Hammett in 1937, where electronic properties of a molecule can be altered with the substitution of an electron withdrawing group or electron donating group. Hence, when an electron donating group is substituted onto an aromatic ring para to a fluorine substituent, the C-F bond is lengthened. [180] Hence, potentially a synonymous effect of the electron donating nature of an electrode bonded in the para position to a C-F bond could have a similar effect. This could be the case for the C-F bonds in the PhF_5 group bonded to the CIC85. One could suggest that the hydrophobic functional group which is chemically bonded to the electrode could itself become electrowetted.

Further research in this area could be to test molecules that are actively designed to prevent electronic coupling between the carbon surface and the molecules. This could potentially be

achieved through the use of a linker group between PhF_5 and the carbon surface. The molecule would be similar to pentafluorophenyl aniline, but include a phenyl spacer group in between the pentafluorophenyl group and the aniline group with the aniline group attached at either the meta- or ortho- position. This would enable the diazonium reduction reaction to still take place as aryl groups form stable diazonium ions and hence the linker group must be an aryl group to enable surface functionalisation to happen via this reaction. If surface functionalisation is possible with this molecule, then with the phenyl linker group attached ortho- or meta to the carbon surface then delocalisation effects from the carbon would be disrupted. However, steric hindrances may cause issues if the ortho- position is used.

Further work could be dedicated to understanding the influence of Nafion on the hydrophobicity performance of the CIC85 and PhF_5CIC85 films. Nafion swells when it absorbs water[181] altering its mechanical properties. Nafion will also arrange itself differently in the presence of hydrophobic and hydrophilic particles.[182] Through the use of a scanning electrochemical microscope – atomic force microscope (SECM-ATM),[183] it could be possible to measure the mechanoelectrochemical properties of Nafion.

5.3 Conclusion

In this study, an electrochemical protocol encompassing cyclic voltammetry and chronoamperometry was successfully established to elucidate the electrowetting behaviour of CIC85 and PhF_5CIC85 materials. Employing structurally uniform carbon materials as the basis of this investigation, the research was able to distinctly attribute variations in capacitance to differential electrowetting properties of the materials governed by PhF_5 groups. Specifically, at positive potential windows, proximal to the open circuit potential (OCP) of both materials, a

marked contrast in electrowetting was evident. Here, CIC85 demonstrated significantly enhanced wetting in comparison to PhF_5CIC85.

The study's investigation into the PhF_5CIC85 material revealed critical insights into its electrowetting properties. Notably, PhF_5CIC85 exhibited a significant increase in capacitance in lower potential windows compared to the higher potential window and pre-chronoamperometry, suggesting a notable change in the material's properties, potentially due to decreased hydrophobicity or morphological alterations. The irreversible nature of this capacitance increase, as observed in cyclic voltammetry measurements, implies a permanent alteration in the material's surface characteristics under specific electrochemical conditions.

This research highlights the importance of investigating hydrophobicity at different potentials due to the impact of electrowetting. Furthermore, other characterisation techniques typically used to measure hydrophobicity of surfaces, such as contact angle measurements proved to be ineffective for this research.

The research opens avenues for further investigation, particularly in understanding the electro-inductive effects of molecules on electrodes properties, such as hydrophobicity and stability.

6

Application of nanoporous carbon particles surface functionalised with polyfluoroaromatics as hydrophobic additives for eCO2RR

Ella Fidment, Preetam Sharma, Viola Birss, Eileen Yu, Elizabeth Gibson

The research in Figure 6-4 and Figure 6-5 was performed by Preetam Sharma.

Abstract

To investigate the impact of porosity and hydrophobicity of the catalyst layer on the selectivity of CO_2 electroreduction on Ag particles, nanoporous carbon particles and hydrophobic nanoporous carbon particles were used as an additive in the catalyst layer. The results indicate that higher porosity and hydrophobicity increase the ratio of CO/H_2. However, due to the eCO2RR conditions, the hydrophobicity of the additives change under the influence of negative potential bias, leading to a decrease in the ratio of CO/H_2. This is consistent with the findings in Chapter 5, which suggest that the hydrophobicity of PhF_5CIC85 decreases under negative potential bias in 1M KOH.

6.1 Introduction

Additives in the catalyst layer of gas diffusion electrodes of CO_2 electroreduction have been used to improve gas transport, ionic conductivity, hydrophobicity[75] and other properties that are believed to enhance CO_2 electroreduction. For example, the use of polymers with intrinsic microporosity (PIMs) within the gas diffusion electrode has been studied. The use of a 0.01 mg/cm^2 PIM layer atop of the catalyst layer was found to increase the activity, selectivity and stability of a copper gas diffusion electrode for ethylene production.[184]

Engineering porosity within the catalyst layer has been researched with different approaches. Additive manufacturing was employed whereby a laser powder bed fusion machine was used to selectively melt Cu powder. Catalyst layers with porosity of from below 1 µm to 30 µm were synthesised with different pore network layouts. They found that the different types of pore networks had a large influence on product distribution.[185]

In contrast, research has been dedicated to investigating the impact of porosity in the gas diffusion layer. A fluoropolymer gas diffusion layer was developed from UV curing of monomers to form a homogenous porous perfluoropolyether.[186] Different curing conditions and monomer ratios enabled tuneable porosity of which the gas permeation was measured. This was then correlated with the faradaic efficiencies when copper nanoparticles were used as a catalyst layer, as shown in Figure 6-1. At low CO_2 permeance, there is a notable loss in CO faradaic efficiency when compared higher CO_2 permeance.

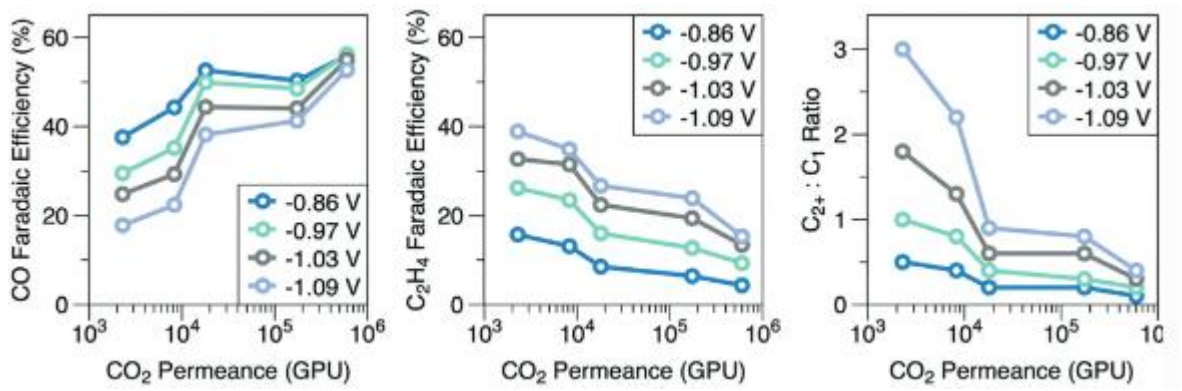

Figure 6-1 Permeance-performance relationship of PFPE. Data of CO2RR catalysed on copper nanoparticle catalyst layer, 1M $KHCO_3$ and a CO_2 inlet flow rate of 50 sccm. Adapted from Wicks et al.[186]

Porosity of the catalyst layer has mainly been investigated by engineering porosity of the catalyst material itself, such as the thermal shock synthesis of Cu_4Bi nanofoam,[187] Cu_2O nanoflowers[188] and ultrasound-assisted synthesis of Cu oxides.[189] Porosity of the catalyst materials are reduced by the addition of an ionomer. After ionomer infiltration, the pore volume of Ag foam synthesised via pulsed hydrogen bubble templation was found to reduce by 50% compared to the as-synthesised material.[190] However the use of the ionomer is believed to create a hydrophobic microenvironment within the electrode structure, improving mass transport and enabling higher current densities.

Modelling has been conducted studying how different parameters of the catalyst layer, such as hydrophobicity, loading, porosity and electrolyte flow rate, affect the performance of the gas diffusion electrode. They predicted that doubling the porosity of a wetted catalyst layer in a gas diffusion electrode can significantly improve the current density due to enhanced gas transport. Higher porosity reduces the mass transport limitations that typically inhibit reactant and product transport, thereby improving reaction kinetics and leading to higher current densities.[191]

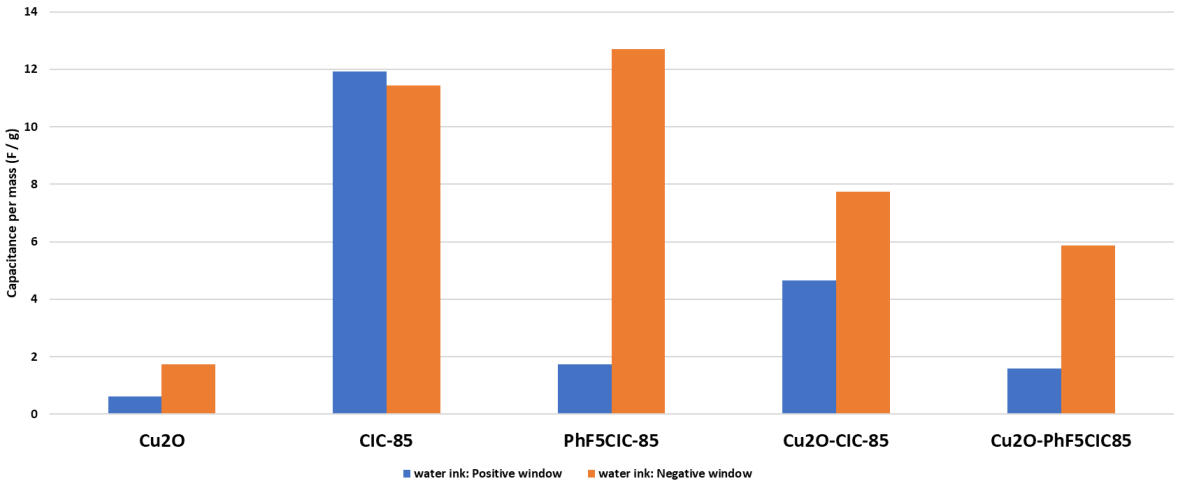

Figure 6-2 Capacitance per mass for Cu_2O, CIC85, PhF_5CIC85, Cu_2O CIC85 and Cu_2OPhF_5CIC85 samples. The samples either contained 11.28 mg of materials or 50:50 ratio of the materials (i.e. 5.6 mg of each material) in the catalyst ink. These inks were dropcast onto the glassy carbon electrode and underwent the CV. Positive window (0.4 – 0.7 V vs. RHE) and negative window (0.0 – 0.4 V vs RHE). The capacitances were calculated by conducting CVs within each potential window at scan rates between 10 mV/s to 140 mv/s, increasing in 10 mV/s intervals. In a set-up illustrated in Figure 5-3a), the material was drop cast onto a GCE. The reference electrode was a mecury based RE-61AP and the counter electrode was a graphite electrode. The electrolyte was always degassed with argon and the electrolyte was 0.1M KOH. The magnitude of current was extracted at 0.52 V vs RHE for the positive window and at 0.22 V vs RHE for the negative window. Capacitance was calculated, taking an average of the forward and backward scan direction of current.

6.2 Results and Discussions

6.2.1 Capacitance of Cu_2O and CIC85 / PhF_5CIC85 samples

Samples of CIC85 and Cu_2O show high capacitance in both potential windows, whereas samples of Cu_2O PhF_5CIC85 show high capacitance in low potential window

In Figure 6-2, the capacitance per mass of the Cu_2O was low when it was measured by CVs in the potential window 0.4 – 0.7 V vs. RHE. From the previous work done on Cu_2O, it was known that within the 0.4-0.7 V vs. RHE window there would be no redox events for the Cu_2O. The capacitance of Cu_2O was believed to be low due to its low conductivity as a metal oxide.[192] Post chronoamperometry at 0.025 V vs. RHE led to the reduction of Cu_2O to Cu. In the 0.0 – 0.4 V vs. RHE potential window, the capacitance of Cu_2O increased and was measured at almost 2 F/g.

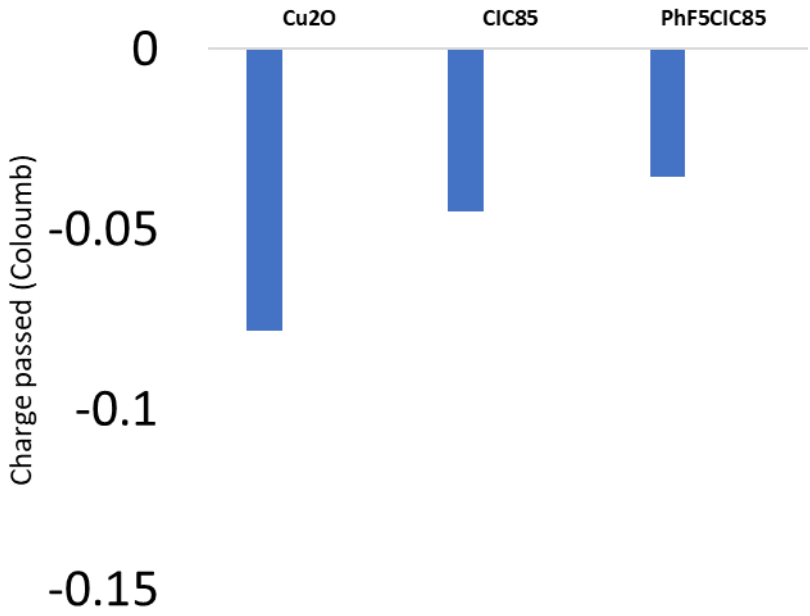

Figure 6-3 Charge passed during the chronoamperometric measurement at 0.025 V vs. RHE in 0.1 M KOH for 15 min.

When studying the capacitance of the composite samples ($Cu_2OCIC85$ and Cu_2OPhF_5CIC85), in the 0.4-0.7 V vs. RHE, the capacitance was much greater for the $Cu_2OCIC85$ compared with Cu_2OPhF_5CIC85. In the negative window on the other hand, the capacitance values of the two samples are similar.

Overall, it indicates a similar trend to the outcomes of the previous chapter's finding whereby PhF_5CIC85 sample is not able to maintain its hydrophobicity at low potential windows. In the presence of Cu_2O, PhF_5CIC85 also does not maintain the hydrophobicity in general for the sample.

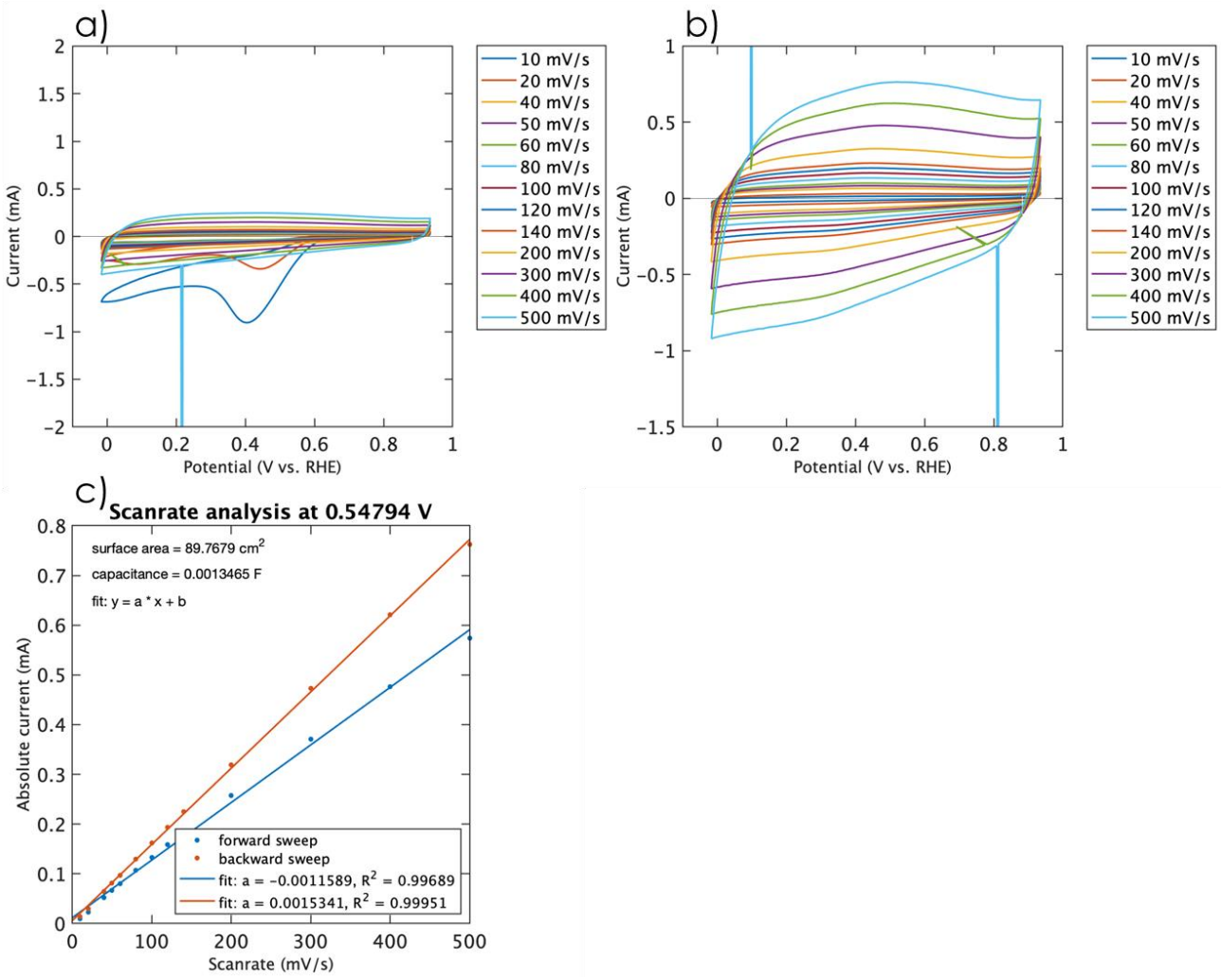

Figure 6-3 a) Scan rate dependent CVs of fresh commercial carbon paper B) scan rate dependent CVs of commercial carbon paper after a chronoamperometry measurement of 0.025 V vs. RHE for 15 min in 0.1 M KOH with RE-61AP reference electrode and a graphite counter electrode. C) scan rate analysis of current values shown in B

When looking at the overall charge passed in the chronoamperometry in **Error! Reference source not found.**, the Cu_2O sample has more charge passed than the CIC85 and PhF_5CIC85 sample. During the chronoamperometry at 0.025 V vs. RHE, the Cu_2O sample is reduced to Cu in a faradaic process. Hence, the number of electrons passed is related to the amount of Cu_2O available to be reduced. Whilst it is believed that no significant faradaic charge is passed for

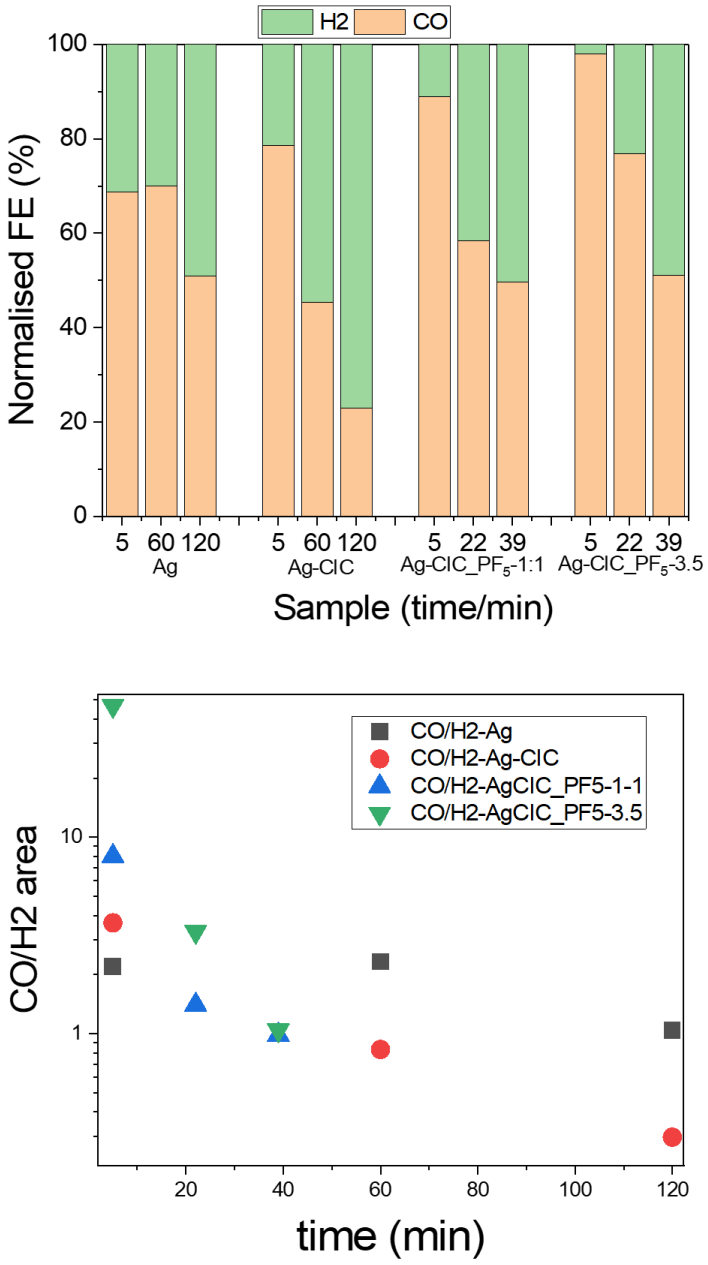

Figure 6-4 Normalised faradaic efficiencies of Ag, Ag-CIC, AgPhF$_5$CIC (1:1 ratio) and AgPhF$_5$CIC (3.5:1 ratio of Ag:PhF5 performed at -1.15 V vs. RHE in 1M KOH.

the CIC85 and PhF$_5$CIC85, only non-faradaic double layer charging occurs. Hence, less charge is attributed to this process for both the CIC85 and PhF$_5$CIC85.

In Figure 6-3 CVs of commercial carbon paper used for gas diffusion electrodes are shown. A significant redox peak can be observed at 0.4 V vs. RHE during the 10 and 20 mV/s scan rate CVs. This is likely due to the carbon paper oxidising during storage and hence the surface oxide groups are being reduced upon the anodic sweep.

In Figure 6-3 b) post chronoamperometry, the capacitance is higher than in Figure 6-4 a). The reduction peaks at ~ 0.45 V vs RHE in Figure 6-4 a) in the CVs with a scan rate of 10 mV /s and 20 mV/s are the result of reduction of surface oxides that have formed due to the commercial carbon paper being in contact with air prior to their use.[193,194]

6.2.2 Ag and PhF_5CIC85 samples trialled for eCO2RR

Ag catalyst with CIC and PhF5CIC additive trialled for eCO2RR at -1.15 V vs. RHE

Ag was employed as the catalytic material for these experiments because it is selective towards carbon monoxide and hydrogen only. Hence, the product evaluation is simpler. The eCO2RR measurements were performed at -1.15 V vs. RHE in 1M KOH and were performed until the gas diffusion electrode floods.

At 5 min, the Ag sample showed a normalised faradaic efficiency of carbon monoxide of ~70%. The Ag-CIC sample showed a normalised faradaic efficiency of carbon monoxide of ~80%. The Ag-CIC_PhF5-1:1 sample showed a faradaic efficiency of carbon monoxide of ~90%, whilst the higher ratio sample, Ag-CIC_PhF5-1:3.5, showed a faradaic efficiency of ~98%. At the beginning of the reaction, the inclusion of the CIC improves the faradaic efficiency of carbon monoxide. It is further improved in the presence of PhF_5CIC particles and increases with a higher ratio of the particles. This could be due to the enhancement of availability of CO_2

concentration at the surface of the catalyst particles because of the porous interconnected networks within the CICs. The further improvement of faradaic efficiency of carbon monoxide in the presence of the PhF_5CIC particles could be due to improved hydrophobic character of the catalyst layer, which leads to less hydrogen evolution that is in competition with CO_2 reduction.

However, within 22 min of the reaction duration, the faradaic efficiencies of carbon monoxide of the PhF_5CIC samples have significantly decreased. This suggests that the hydrophobic environment believed to be a result of the hydrophobic PhF_5CIC is not sustained throughout the reaction. This finding is in agreement with the findings of Chapter 5 that shows quantitatively that the hydrophobicity of the PhF_5CIC decreases under negative potential windows. This is observed in the eCO2RR conditions, where hydrophobicity is believed to be inversely correlated with the faradaic efficiency of carbon monoxide.

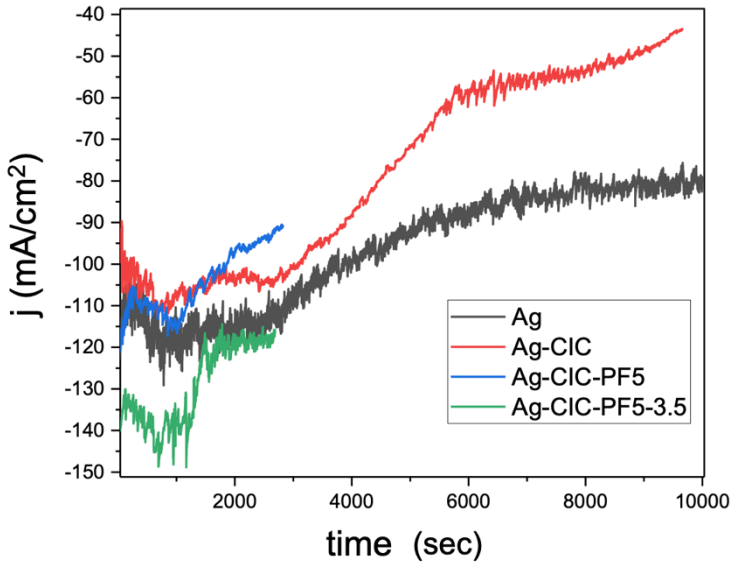

Figure 6-5 Current density of the samples: Ag, Ag-CIC, Ag-CIC-PF5 (1:1) and Ag-CIC-PF5-3.5 over time.

Further to the hydrophobicity loss, the PhF_5CIC samples was stable for only 3000 s. However, upon observation the catalyst layer appears to have poor adhesion to the carbon paper of the microporous layer.

Whilst both samples of Ag and Ag-CIC were able to run for 10000 s, at 120 min the AgCIC had a lower current density than the Ag sample and a lower CO/H_2 ratio. This is in contrast to the result at 5 min, where the Ag-CIC sample had a higher CO/H_2 ratio than the Ag sample. Hence, the AgCIC sample showed greater variation of product selectivity and current density. From initial CV testing of the CIC samples, faradaic current attributed to HER was observed for the CIC material. Thus, potentially the CIC could be a catalytic site for HER.

A critical consideration surrounding the contents of Nafion is that the ratio of Nafion to total material remained the same in each sample. However, the materials have different hydrophobic characters. If there is a tendency of Nafion to interact more strongly with hydrophilic materials, such as Ag particles, compared with hydrophobic particles, then the samples with

hydrophobic materials could have higher amounts of Nafion in the ink. This could change the amount of Nafion surrounding Ag particles in the catalyst layer. With differences in Nafion arrangements and/or Nafion interaction with Ag, different faradaic efficiencies have been observed in studies.[195] Further experiments could be conducted, whereby the Nafion amount stays constant with respect to the catalyst material only. This could test the hypothesis of whether the variation in Nafion could affect faradaic selectivity towards carbon monoxide.

6.3 Conclusion

This chapter examines the selectivity of gas diffusion electrodes composed of catalyst, Ag particles and additives in the catalyst layer, i.e. porous carbon particles and functionalised carbon particles. The results indicate that CIC and PhF_5CIC85 additive give high CO/H_2 selectivity at the beginning of the reaction. This could be due to their high porosity, which allows optimal mass transport of CO_2 to the catalyst sites. PhF_5CIC85 and Ag show the highest CO selectivity at 5 min into the reaction, indicating that increasing the hydrophobicity of the catalyst layer also improves the selectivity of CO over H_2. However, during the course of the reaction, the CO/H_2 ratio decreases for all samples with additives, indicating that the optimum conditions are not stable under eCO_2RR conditions. This is consistent with the findings in Chapter 5, which suggest that the hydrophobicity of PhF_5CIC85 decreases under negative potential bias in 1M KOH.

7

Conclusion

eCO2RR offers a route to decarbonise energy requirements for industries where chemical energy is typically used to provide energy, such as aviation and domestic heating. However, developing catalysts that afford selectivity towards multi-carbon products is still the focus of much research. With longer reduction pathways requiring more electrons, multi-carbon products are still hard to produce at significant rates. Furthermore, degradation of the gas diffusion electrode is an issue under the electrochemical conditions for CO_2 electroreduction. Flooding of the gas diffusion electrode reduces the availability of CO_2 to the ideal triple phase reaction centres and hence the selectivity towards carbonaceous products reduces and HER increases. The research in this thesis set out to investigate both these issues.

(1) Au decorated Cu_2O microparticles via electrodeposition were observed to produce higher faradaic efficiency of longer chain alcohols compared to Cu_2O microparticles, however the overall rate of production of carbonaceous products decreased. The rate of ethanol and propanol production increased by 2 and 4.5 nmol s^{-1} cm^{-2} respectively with the $AuCu_2O$ compared to Cu_2O. Overall the inclusion of gold in the catalytic layer resulted in higher *CO concentration which favoured high length carbon products.

Faradaic efficiency of hydrogen was marginally lower at 16% with $AuCu_2O$ with respect to Cu_2O.

(2) The hydrophobicity of nanoporous carbon particles functionalised with fluorophenyl molecules were measured with capacitance in different potential windows and compared to nanoporous carbons absent of functionalisation. It was found that the capacitance per mass was 2.69 F/g of PhF_5CIC with respect to a capacitance per mass of 10.92 F/g of CIC. When a more negative potential window was applied, the capacitance of PhF_5CIC per mass increased to 6.8 F/g for the PhF_5CIC, providing evidence for electrowetting of PhF_5CIC.

(3) PhF_5CIC was utilised as a hydrophobic additive in the catalyst layer with Ag particles and the ratio of CO/H_2 was measured. At 5 min, the ratio of CO/H_2 faradaic efficiency was 50, showing preference of CO_2 electroreduction with respect to HER. However, under longer electrochemical conditions, the CO/H_2 faradaic efficiency ratio lowered to 3 at 22 min, indicating electrolyte intrusion. This is in agreement with the capacitance studies conducted to measure hydrophobicity, whereby hydrophobicity of PhF_5CIC decreases significantly under electrochemical conditions.

The research thesis on CO_2 electroreduction in gas diffusion electrode setups presents significant findings regarding bimetallic selectivity and hydrophobicity. The conclusion drawn from Chapter 3 highlighted that adding Au to Cu_2O bimetallic catalysts enhances selectivity for CO_2 reduction. Chapter 4 further elaborated on this by showing that gold enables CO insertion, leading to a bifurcation of the reaction pathway and a preference for producing ethanol and

n-propanol over ethylene in Au-Cu_2O samples, indicating a time-dependent process for *CO coverage and the influence of CO dimerization on product distribution.

In terms of hydrophobicity, Chapter 5 discussed modifications to cyclic voltammetry to accommodate potential delays due to elevated resistance, highlighting the importance of electrolyte stability and non-faradaic contributions in measurements. Chapter 6 explored the use of nanoporous carbon particles functionalized with polyfluoroaromatics as hydrophobic substrates, indicating that these additives could enhance the availability of CO_2 at the catalyst surface and, initially, improve faradaic efficiency for carbon monoxide. However, the hydrophobic environment was not sustained throughout the reaction, suggesting a decrease in hydrophobicity under negative potential windows and affecting the faradaic efficiency and stability negatively.

Together, these findings underscore the importance of bimetallic catalyst composition and hydrophobic additives in improving the selectivity and efficiency of CO_2 electroreduction processes, with a note on the temporal and environmental stability of these enhancements.

8

Future outlook

This research targeted these obstacles through the use of a secondary metal on Cu_2O with selectivity towards carbon monoxide. Further work could be dedicated to in-situ characterisation of intermediates, such as surface enhanced infrared absorption spectroscopy (SEIRAS) is sensitive to C-O containing adsorbates. [132] With this technique, *CO has been confirmed as a common intermediate. [133] With SEIRAS, it would be expected that a higher concentration of *CO would be seen in $AuCu_2O$ when compared to Cu_2O.

One issue of the eCO2RR cell set-up is limits to detection of products that are produced at low rates and are diluted in the electrolyte. The electrolyte circulation through the set-up can be improved to increase the accuracy of formate. This could be achieved by using a smaller volume of catholyte circulating, hence it will be likely that homogeneity of analytes can be achieved over a shorter period of time. Alternatively, a stirrer bar could be used in the catholyte vessel that is connected to the electrochemical cell to ensure that is constantly mixed and has uniform homogeneity. A more interesting study would be to have a stirrer bar within the catholyte itself, which could affect the fluid pressure within the catholyte chamber and impact carbonate concentration, gas pressure, catalyst layer – diffusion medium interface position within the gas diffusion electrode.

Modelling of electrochemical reduction of CO_2 to CO in a gas diffusion electrode could be used to indicate physical parameters that could inform optimisation of the Au-Cu_2O catalyst layer (for example, parameters such as catalyst thickness and electrolyte flow rate). Wessling et al. provided a study of porous electrodes within GDE properties for CO_2 reduction.[196]

In this work, a mixture of multicarbon products were evolved through the use of a bimetallic catalyst. Research avenues examining altering the pathway favourability towards one product could be explored. For example, the use of organic molecules attached to copper surfaces which stabilise *CO atop intermediate, favouring the pathway to ethylene. [197]

With regards to stability work with the use of fluorophenyl functionalised nanoporous carbon particles as an additive for the catalyst layer, future work could serve to investigate the role of the Nafion in the hydrophobicity change that occurs during the gas diffusion electrode under electrochemical conditions. Using in-situ AFM mapping could be done on the location of Nafion to observe how that changes under electrochemical conditions, such as the work by Hiesgen et al.[198] One could observe how the Nafion self-assembles in different solvents of catalyst ink and how it arranges regarding the catalyst particles and additives, such as the study of Nafion structures due to solvent.[199] Solvents of different polarity, such as water or benzene, could result in different orientations of Nafion within the catalyst ink. If the additives used have different surface charge to the catalyst particles, they are likely to have a different interaction between the different Nafion groups. More specifically, the ester group in the backbone could hydrogen bond to any oxygen atoms on the surface of Cu_2O, whereas the C-F bonds of the Nafion are likely to sit more closely to the PhF_5 groups on carbon particles.

Overall, eCO2RR offers a desirable avenue for the generation of fuels and chemical feedstocks. With an increase in environmental tipping points observed within the last 5 years, the motivation to upscale eCO2RR has never been stronger. Issues remain however with selectivity. Improvements in catalyst design have often seen a larger span of products instead of higher efficiency towards one product, such as ethylene. Furthermore, stability continues to be an issue and further work is required on this area to reach 10,000+ hours required for commercial viability.[200]

9

References

1. Friedlingstein P, O'Sullivan M, Jones MW, Andrew RM, Bakker DCE, Hauck J, et al. Global Carbon Budget 2023. Earth Syst Sci Data [Internet]. 2023;15(12):5301–69. Available from: https://essd.copernicus.org/articles/15/5301/2023/

2. Greenhouse gases continued to increase rapidly in 2022 [Internet]. 2023. Available from: https://www.noaa.gov/news-release/greenhouse-gases-continued-to-increase-rapidly-in-2022

3. IPCC. Synthesis Report of the Sixth Assessment Report [Internet]. Vol. https://ww, IPCC Working Groups I & II. 2023. Available from: https://www.ipcc.ch/ar6-syr/%0Ahttps://www.ipcc.ch/assessment-report/ar6/

4. Beck EG. 180 years of atmospheric CO2 gas analysis by chemical methods. Energy and Environment. 2007;18(2):259–82.

5. Hanel RA, Conrath BJ, Kunde VG, Prabhakara C, Revah I, Salomonson V V., et al. The Nimbus 4 infrared spectroscopy experiment: 1. Calibrated thermal emission spectra. J Geophys Res. 1972;77(15):2629–41.

6. Ginley DS, Cahen D. Fundamentals of materials for energy and environmental sustainability. Fundamentals of Materials for Energy and Environmental Sustainability. 2011. 1–753 p.

7. Ritchie H, Rosado P. Electricity Mix. Our World in Data. 2020;

8. Department for Business, Energy & Industrial Strategy, Prime Minister's Office 10 Downing Street. UK enshrines new target in law to slash emissions by 78% by 2035 [Internet]. Available from: https://www.gov.uk/government/news/uk-enshrines-new-target-in-law-to-slash-emissions-by-78-by-2035

9. Department for Energy Security and Net Zero, Department for Business E& IS. Energy white paper: Powering our net zero future [Internet]. 2020. Available from: https://www.gov.uk/government/publications/energy-white-paper-powering-our-net-zero-future

10. Millen S, Page E. Transport and Environment Statistics 2021 Annual Report. Department for Transport. 2021;

11. Lin H, Clavreul J, Jeandaux C, Crawley J, Butnar I. Environmental life cycle assessment of heating systems in the UK: Comparative assessment of hybrid heat pumps vs. condensing gas boilers. Energy Build. 2021;240:110865.

12. Kurda R, Silvestre JD, de Brito J. Life cycle assessment of concrete made with high volume of recycled concrete aggregates and fly ash. Resour Conserv Recycl. 2018;139:407–17.

13. Ritchie H. Cars, planes, trains: where do CO2 emissions from transport come from? Our World in Data [Internet]. 2020; Available from: https://ourworldindata.org/co2-emissions-from-transport

14. Ansell PJ, Haran KS. Electrified Airplanes: A Path to Zero-Emission Air Travel. IEEE Electrification Magazine. 2020;8(2):18–26.

15. Daiyan R, Macgill I, Amal R. Opportunities and Challenges for Renewable Power-to-X. ACS Energy Lett. 2020;5(12):3843–7.

16. Schulz H. Short history and present trends of Fischer–Tropsch synthesis. Appl Catal A Gen. 1999;186(1–2):3–12.

17. Żuk P, Żuk P. National energy security or acceleration of transition? Energy policy after the war in Ukraine. Joule. 2022;6(4):709–12.

18. Gielen D, Boshell F, Saygin D, Bazilian MD, Wagner N, Gorini R. The role of renewable energy in the global energy transformation. Energy strategy reviews. 2019;24:38–50.

19. Engineering solutions for CO2 conversion. Weinheim: Wiley-VCH; 2021.

20. Ghaib K, Nitz K, Ben-Fares F. Chemical methanation of CO2: A review. ChemBioEng Reviews. 2016;3(6):266–75.

21. Daza YA, Kuhn JN. CO 2 conversion by reverse water gas shift catalysis: comparison of catalysts, mechanisms and their consequences for CO 2 conversion to liquid fuels. RSC Adv. 2016;6(55):49675–91.

22. le Saché E, Reina TR. Analysis of Dry Reforming as direct route for gas phase CO2 conversion. The past, the present and future of catalytic DRM technologies. Prog Energy Combust Sci. 2022;89.

23. James OO, Chowdhury B, Mesubi MA, Maity S. Reflections on the chemistry of the Fischer–Tropsch synthesis. RSC Adv. 2012;2(19):7347–66.

24. Peschel A. DRYREFTM & SYNSPIRETM Innovation for HyCO applications. In: Global Syngas Conference. 2020.

25. Synergized benefits of Linde DRYREFTM and BASF SYNSPIRE [Internet]. Available from: https://catalysts.basf.com/files/literature-library/DRYREF_SYNSPIRE_brochure_EN.pdf

26. Gao J, Choo Sze Shiong S, Liu Y. Reduction of CO2 to chemicals and Fuels: Thermocatalysis versus electrocatalysis. Chemical Engineering Journal. 2023;472.

27. Conversion of Carbon Dioxide into Hydrocarbons Vol. 1 Catalysis. 1st ed. 20. 2020. (Environmental chemistry for a sustainable world ; 40).

28. Zhang J, Li Z, Zhang Z, Feng K, Yan B. Can thermocatalytic transformations of captured CO2 reduce CO2 emissions? Appl Energy. 2021;281:116076.

29. Dhakshinamoorthy A, Navalon S, Corma A, Garcia H. Photocatalytic CO2 reduction by TiO2 and related titanium containing solids. Energy Environ Sci [Internet]. 2012;5(11):9217–33. Available from: http://dx.doi.org/10.1039/C2EE21948D

30. Kortlever R, Shen J, Schouten KJP, Calle-Vallejo F, Koper MTM. Catalysts and Reaction Pathways for the Electrochemical Reduction of Carbon Dioxide. Journal of Physical Chemistry Letters. 2015;6(20):4073–82.

31. Zhang YJ, Sethuraman V, Michalsky R, Peterson AA. Competition between CO2 reduction and H2 evolution on transition-metal electrocatalysts. ACS Catal. 2014;4(10):3742–8.

32. Tackett BM, Gomez E, Chen JG. Net reduction of CO2 via its thermocatalytic and electrocatalytic transformation reactions in standard and hybrid processes. Nat Catal. 2019;2(5):381–6.

33. Lai W, Qiao Y, Zhang J, Lin Z, Huang H. Design strategies for markedly enhancing energy efficiency in the electrocatalytic CO2 reduction reaction. Energy Environ Sci. 2022;15(9):3603–29.

34. Hori Y, Wakebe H, Tsukamoto T, Koga O. Electrocatalytic process of CO selectivity in electrochemical reduction of CO2 at metal electrodes in aqueous media. Electrochim Acta. 1994;39(11–12):1833–9.

35. Peterson AA, Abild-Pedersen F, Studt F, Rossmeisl J, Nørskov JK. How copper catalyzes the electroreduction of carbon dioxide into hydrocarbon fuels. Energy Environ Sci. 2010;3(9):1311–5.

36. Dutta A, Rahaman M, Luedi NC, Mohos M, Broekmann P. Morphology Matters: Tuning the Product Distribution of CO2 Electroreduction on Oxide-Derived Cu Foam Catalysts. ACS Catal. 2016 Jun 3;6(6):3804–14.

37. Reske R, Mistry H, Behafarid F, Roldan Cuenya B, Strasser P. Particle size effects in the catalytic electroreduction of CO2 on Cu nanoparticles. J Am Chem Soc. 2014;136(19):6978–86.

38. Feng X, Jiang K, Fan S, Kanan MW. A direct grain-boundary-activity correlation for CO electroreduction on Cu nanoparticles. ACS Cent Sci. 2016;

39. Yang C, Shen H, Guan A, Liu J, Li T, Ji Y, et al. Fast cooling induced grain-boundary-rich copper oxide for electrocatalytic carbon dioxide reduction to ethanol. J Colloid Interface Sci. 2020;

40. Mistry H, Reske R, Strasser P, Cuenya BR. Size-dependent reactivity of gold-copper bimetallic nanoparticles during CO2 electroreduction. Catal Today. 2017;288:30–6.

41. Ren D, Deng Y, Handoko AD, Chen CS, Malkhandi S, Yeo BS. Selective Electrochemical Reduction of Carbon Dioxide to Ethylene and Ethanol on Copper(I) oxide catalysts. ACS Catal. 2015;5(5):2814–21.

42. Li CW, Ciston J, Kanan MW. Electroreduction of carbon monoxide to liquid fuel on oxide-derived nanocrystalline copper. Nature. 2014;508(7497):504–7.

43. Li CW, Kanan MW. CO2 Reduction at Low Overpotential on Cu Electrodes Resulting from the Reduction of Thick Cu2O Films. J Am Chem Soc [Internet]. 2012 May 2;134(17):7231–4. Available from: https://doi.org/10.1021/ja3010978

44. Stephens IEL, Bondarenko AS, Grønbjerg U, Rossmeisl J, Chorkendorff I. Understanding the electrocatalysis of oxygen reduction on platinum and its alloys. Energy Environ Sci. 2012;5(5):6744–62.

45. Hammer B, Morikawa Y, Nørskov JK. CO chemisorption at metal surfaces and overlayers. Phys Rev Lett. 1996;76(12):2141.

46. Manthiram K, Beberwyck BJ, Alivisatos AP. Enhanced electrochemical methanation of carbon dioxide with a dispersible nanoscale copper catalyst. J Am Chem Soc. 2014;136(38):13319–25.

47. Loiudice A, Lobaccaro P, Kamali EA, Thao T, Huang BH, Ager JW, et al. Tailoring copper nanocrystals towards C2 products in electrochemical CO2 reduction. Angewandte Chemie International Edition. 2016;55(19):5789–92.

48. Hori Y, Wakebe H, Tsukamoto T, Koga O. Adsorption of CO accompanied with simultaneous charge transfer on copper single crystal electrodes related with electrochemical reduction of CO2 to hydrocarbons. Surf Sci. 1995;335:258–63.

49. Takahashi I, Koga O, Hoshi N, Hori Y. Electrochemical reduction of CO2 at copper single crystal Cu (S)-[n (111)×(111)] and Cu (S)-[n (110)×(100)] electrodes. Journal of Electroanalytical Chemistry. 2002;533(1–2):135–43.

50. Hori Y, Takahashi I, Koga O, Hoshi N. Selective formation of C2 compounds from electrochemical reduction of CO2 at a series of copper single crystal electrodes. J Phys Chem B. 2002;106(1):15–7.

51. Li Y, Sun Q. Recent Advances in Breaking Scaling Relations for Effective Electrochemical Conversion of CO2. Adv Energy Mater. 2016;6(17).

52. Hanselman S, Koper MTM, Calle-Vallejo F. Computational Comparison of Late Transition Metal (100) Surfaces for the Electrocatalytic Reduction of CO to C2Species. ACS Energy Lett. 2018;3(5):1062–7.

53. Feaster JT, Shi C, Cave ER, Hatsukade T, Abram DN, Kuhl KP, et al. Understanding selectivity for the electrochemical reduction of carbon dioxide to formic acid and carbon monoxide on metal electrodes. ACS Catal. 2017;7(7):4822–7.

54. Liu X, Xiao J, Peng H, Hong X, Chan K, Nørskov JK. Understanding trends in electrochemical carbon dioxide reduction rates. Nat Commun. 2017;8(1):15438.

55. Vasileff A, Xu C, Jiao Y, Zheng Y, Qiao SZ. Surface and Interface Engineering in Copper-Based Bimetallic Materials for Selective CO2 Electroreduction. Chem. 2018;4(8):1809–31.

56. Cave ER, Montoya JH, Kuhl KP, Abram DN, Hatsukade T, Shi C, et al. Electrochemical CO2 reduction on Au surfaces: Mechanistic aspects regarding the formation of major and minor products. Physical Chemistry Chemical Physics. 2017;19(24):15856–63.

57. Zhu W, Tackett BM, Chen JG, Jiao F. Bimetallic Electrocatalysts for CO2 Reduction. Top Curr Chem. 2018;376(6).

58. Zhou JH, Lan DW, Yang SS, Guo Y, Yuan K, Dai LX, et al. Thin-walled hollow Au-Cu nanostructures with high efficiency in electrochemical reduction of CO2 to CO. Inorg Chem Front. 2018;5(7):1524–32.

59. Birhanu MK, Tsai MC, Chen CT, Kahsay AW, Zeleke TS, Ibrahim KB, et al. Electrocatalytic reduction of carbon dioxide on gold–copper bimetallic nanoparticles: Effects of surface composition on selectivity. Electrochim Acta [Internet]. 2020;356:136756. Available from: https://doi.org/10.1016/j.electacta.2020.136756

60. Ma X, Shen Y, Yao S, Shu M, Si R, An C. Self-Supported Nanoporous Au3Cu Electrode with Enriched Gold on Surface for Efficient Electrochemical Reduction of CO2. Chemistry–A European Journal. 2020;26(18):4143–9.

61. Liu K, Ma M, Wu L, Valenti M, Cardenas-Morcoso D, Hofmann JP, et al. Electronic effects determine the selectivity of planar Au–Cu bimetallic thin films for electrochemical CO2 reduction. ACS Appl Mater Interfaces. 2019;11(18):16546–55.

62. Chang F, Wang C, Wu X, Liu Y, Wei J, Bai Z, et al. Strained Lattice Gold-Copper Alloy Nanoparticles for Efficient Carbon Dioxide Electroreduction. Materials. 2022;15(14).

63. Kuang S, Su Y, Li M, Liu H, Chuai H, Chen X, et al. Asymmetrical electrohydrogenation of CO2 to ethanol with copper–gold heterojunctions. Proceedings of the National Academy of Sciences. 2023;120(4):e2214175120.

64. Rakhsha A, Eslami R, Yang X, Noor N, Ismail FM, Abdellah AM, et al. Tandem gold/copper catalysis and morphological tuning via wrinkling to boost CO2 electroreduction into C2+ products. Nano Energy. 2025;133:110457.

65. Gao J, Ren D, Guo X, Zakeeruddin SM, Grätzel M. Sequential catalysis enables enhanced C-C coupling towards multi-carbon alkenes and alcohols in carbon dioxide reduction: A study on bifunctional Cu/Au electrocatalysts. Faraday Discuss. 2019;215:282–96.

66. Rettenmaier C, Herzog A, Casari D, Rüscher M, Jeon HS, Kordus D, et al. Operando insights into correlating CO coverage and Cu–Au alloying with the selectivity of Au NP-decorated Cu 2 O nanocubes during the electrocatalytic CO 2 reduction. EES catalysis. 2024;2(1):311–23.

67. Monzó J, Malewski Y, Kortlever R, Vidal-Iglesias FJ, Solla-Gullón J, Koper MTM, et al. Enhanced electrocatalytic activity of Au@Cu core@shell nanoparticles towards CO2 reduction. J Mater Chem A Mater. 2015;3(47):23690–8.

68. Nguyen TN, Dinh CT. Gas diffusion electrode design for electrochemical carbon dioxide reduction. Chem Soc Rev. 2020;49(21):7488–504.

69. Dinh CT, Burdyny T, Kibria G, Seifitokaldani A, Gabardo CM, Pelayo García De Arquer F, et al. CO2 electroreduction to ethylene via hydroxide-mediated copper catalysis at an abrupt interface. Science (1979). 2018;360(6390):783–7.

70. Hernandez-Aldave S, Andreoli E. Fundamentals of gas diffusion electrodes and electrolysers for carbon dioxide utilisation: Challenges and opportunities. Catalysts. 2020;10(6):1–34.

71. Li M, Idros MN, Wu Y, Burdyny T, Garg S, Zhao XS, et al. The role of electrode wettability in electrochemical reduction of carbon dioxide. J Mater Chem A Mater. 2021;9(35):19369–409.

72. Zhang T, Li Z, Lyu X, Raj J, Zhang G, Kim H, et al. The conventional gas diffusion electrode may not be resistant to flooding during CO2/CO reduction. J Electrochem Soc. 2022;169(10):104506.

73. Shi R, Guo J, Zhang X, Waterhouse GIN, Han Z, Zhao Y, et al. Efficient wettability-controlled electroreduction of CO2 to CO at Au/C interfaces. Nat Commun. 2020;11(1).

74. Xing Z, Hu L, Ripatti DS, Hu X, Feng X. Enhancing carbon dioxide gas-diffusion electrolysis by creating a hydrophobic catalyst microenvironment. Nat Commun. 2021;12(1).

75. Wissink T, van de Poll RCJ, Figueiredo MC, Hensen EJM. Stability of In2O3 nanoparticles in PTFE-containing gas diffusion electrodes for CO2 electroreduction to formate. Journal of CO2 Utilization. 2023;67:102331.

76. Sheng X, Ge W, Jiang H, Li C. Engineering the Ni□ N□ C Catalyst Microenvironment Enabling CO2 Electroreduction with Nearly 100% CO Selectivity in Acid. Advanced Materials. 2022;34(38):2201295.

77. Wang M, Lin L, Zheng Z, Jiao Z, Hua W, Wang G, et al. Hydrophobized electrospun nanofibers of hierarchical porosity as the integral gas diffusion electrode for full-pH CO2 electroreduction in membrane electrode assemblies. Energy Environ Sci [Internet]. 2023;16(10):4423–31. Available from: http://dx.doi.org/10.1039/D3EE01866K

78. Li L, Chen J, Mosali VSS, Liang Y, Bond AM, Gu Q, et al. Hydrophobicity graded gas diffusion layer for stable electrochemical reduction of CO2. Angewandte Chemie. 2022;134(39):e202208534.

79. Raciti D, Braun TM, Tackett B, Xu H, Cruz M, Wiley B, et al. Self-Supporting Ag Nanowire Mat Electrodes on PTFE Gas Diffusion Layers for Electrochemical Conversion of CO2 to CO. In: Electrochemical Society Meeting Abstracts 242. The Electrochemical Society, Inc.; 2022. p. 1489.

80. Ren P, Pei P, Li Y, Wu Z, Chen D, Huang S, et al. Diagnosis of water failures in proton exchange membrane fuel cell with zero-phase ohmic resistance and fixed-low-frequency impedance. Appl Energy. 2019;239:785–92.

81. Meyer Q, Zeng Y, Zhao C. Electrochemical impedance spectroscopy of catalyst and carbon degradations in proton exchange membrane fuel cells. J Power Sources [Internet]. 2019;437(July):226922. Available from: https://doi.org/10.1016/j.jpowsour.2019.226922

82. Meyer Q, Liu S, Ching K, Da Wang Y, Zhao C. Operando monitoring of the evolution of triple-phase boundaries in proton exchange membrane fuel cells. J Power Sources [Internet]. 2023;557(January):232539. Available from: https://doi.org/10.1016/j.jpowsour.2022.232539

83. Csoklich C, Xu H, Marone F, Schmidt TJ, Büchi FN. Laser structured gas diffusion layers for improved water transport and fuel cell performance. ACS Appl Energy Mater. 2021;4(11):12808–18.

84. Chen YC, Dörenkamp T, Csoklich C, Berger A, Marone F, Eller J, et al. On the water transport mechanism through the microporous layers of operando polymer electrolyte fuel cells probed directly by X-ray tomographic microscopy. Energy Advances. 2023;2(9):1447–63.

85. Kong Y, Hu H, Liu M, Hou Y, Kolivoška V, Vesztergom S, et al. Visualisation and quantification of flooding phenomena in gas diffusion electrodes used for electrochemical CO2 reduction: A combined EDX/ICP–MS approach. J Catal. 2022;408:1–8.

86. Niu ZZ, Gao FY, Zhang XL, Yang PP, Liu R, Chi LP, et al. Hierarchical Copper with Inherent Hydrophobicity Mitigates Electrode Flooding for High-Rate CO2 Electroreduction to Multicarbon Products. J Am Chem Soc [Internet]. 2021 Jun 2;143(21):8011–21. Available from: https://doi.org/10.1021/jacs.1c01190

87. Liu Z, Lv X, Kong S, Liu M, Liu K, Zhang J, et al. Interfacial Water Tuning by Intermolecular Spacing for Stable CO2 Electroreduction to C2+ Products. Angewandte Chemie International Edition. 2023;62(43):e202309319.

88. Luo Q, Duan H, McLaughlin MC, Wei K, Tapia J, Adewuyi JA, et al. Why surface hydrophobicity promotes CO2 electroreduction: a case study of hydrophobic polymer N-heterocyclic carbenes. Chem Sci [Internet]. 2023;14(36):9664–77. Available from: http://dx.doi.org/10.1039/D3SC02658B

89. Fisher AC. Electrode Dynamics. Electrode Dynamics. 1996.

90. Zhang Z, Che H, Wang Y, Gao J, Zhao L, She X, et al. Facile synthesis of mesoporous Cu 2O microspheres with improved catalytic property for dimethyldichlorosilane synthesis. Ind Eng Chem Res. 2012 Jan 25;51(3):1264–74.

91. Luong S, Atwa M, Valappil MO, Birss VI. The influence of monolayer and multilayer diazonium functionalities on the electrochemical oxidation of nanoporous carbons. J Electrochem Soc. 2022;169(3):31512.

92. Akhtar K, Khan SA, Khan SB, Asiri AM. Scanning electron microscopy: Principle and applications in nanomaterials characterization. Handbook of Materials Characterization. 2018;113–45.

93. Zhu FY, Wang QQ, Zhang XS, Hu W, Zhao X, Zhang HX. 3D nanostructure reconstruction based on the SEM imaging principle, and applications. Nanotechnology. 2014;25(18).

94. Yin Y, Lu Y. Handbook Of Synthetic Methodologies And Protocols Of Nanomaterials [Internet]. Vols 1–4, Handbook Of Synthetic Methodologies And Protocols Of Nanomaterials. World Scientific; 2019. 1–2370 p. Available from: https://www.worldscientific.com/doi/abs/10.1142/11200-vol4

95. Southworth HN. Scanning Electron Microscopy and Microanalysis. 4th ed. 20. Physicochemical Methods of Mineral Analysis. 1975. 421–450 p.

96. Dinnebier RE, Billinge SJL. Powder Diffraction [Internet]. Powder Diffraction. The Royal Society of Chemistry; 2008. Available from: https://doi.org/10.1039/9781847558237

97. Siegrist T. X-Ray Structure Analysis [Internet]. X-Ray Structure Analysis. Berlin, Boston: De Gruyter; 2021. Available from: https://doi.org/10.1515/9783110610833

98. Law KY, Zhao H. Surface wetting: Characterization, contact angle, and fundamentals. Surface Wetting: Characterization, Contact Angle, and Fundamentals. 2015. 1–162 p.

99. Guinier A. X-ray diffraction in crystals, imperfect crystals, and amorphous bodies. New York: Dover Publications, INC.; 1994.

100. Tjong SC, Chen H. Nanocrystalline materials and coatings. Materials Science and Engineering R: Reports. 2004;45(1–2):1–88.

101. Huang YK, Menovsky AA, de Boer FR. Electrical resistivity of nanocrystalline copper. Nanostructured Materials. 1993;2(5):505–13.

102. Ealias AM, Saravanakumar MP. A review on the classification, characterisation, synthesis of nanoparticles and their application. IOP Conf Ser Mater Sci Eng. 2017;263(3).

103. Ijaz I, Gilani E, Nazir A, Bukhari A. Detail review on chemical, physical and green synthesis, classification, characterizations and applications of nanoparticles. Green Chem Lett Rev. 2020;13(3):59–81.

104. Rao CNR, Cheetham AK. Science and technology of nanomaterials: current status and future prospects. 2003;45–52.

105. Anandhavalli N, Mol B, Manikandan S, Anusha N, Ponnusami V, Rajan KS. Green Synthesis of Cupric Oxide Nanoparticles Using Water Extract of Murrya koenigi and its Photocatalytic Activity. Asian Journal of Chemistry. 2015;27(7):2523–6.

106. Eid AM, Fouda A, Hassan SED, Hamza MF, Alharbi NK, Elkelish A, et al. Plant-Based Copper Oxide Nanoparticles; Biosynthesis, Characterization, Antibacterial Activity, Tanning Wastewater Treatment, and Heavy Metals Sorption. Catalysts. 2023 Feb 3;13(2):348.

107. Mistry H, Varela AS, Bonifacio CS, Zegkinoglou I, Sinev I, Choi YW, et al. Highly selective plasma-activated copper catalysts for carbon dioxide reduction to ethylene. Nat Commun. 2016;7.

108. Wang Y, Arandiyan H, Dastafkan K, Li Y, Zhao C. Common pitfalls of reporting electrocatalysts for water splitting. Chem Res Chin Univ. 2020;36(3):360–5.

109. Wei C, Sun S, Mandler D, Wang X, Qiao SZ, Xu ZJ. Approaches for measuring the surface areas of metal oxide electrocatalysts for determining their intrinsic electrocatalytic activity. Chem Soc Rev. 2019;48(9):2518–34.

110. Aoki KJ, He R, Chen J. Double-layer capacitances caused by ion–solvent interaction in the form of Langmuir-typed concentration dependence. Electrochem. 2021;2(4):631–42.

111. Hernandez D, Cabrera CR, Mendez L, Diaz-Serrano M, Vega O, Weiner BR, et al. Oxidized SWCNT chemically attached to a modified copper substrate. Appl Surf Sci. 2015 Aug;346:415–22.

112. Xiang H, Rasul S, Scott K, Portoles J, Cumpson P, Yu EH. Enhanced selectivity of carbonaceous products from electrochemical reduction of CO 2 in aqueous media. Journal of CO2 Utilization. 2019;30:214–21.

113. Komsiyska L, Staikov G. Electrocrystallization of Au nanoparticles on glassy carbon from HClO4 solution containing [AuCl4]-. Electrochim Acta. 2008;54(2):168–72.

114. Lu X, Tuan HY, Chen J, Li ZY, Korgel BA, Xia Y. Mechanistic Studies on the Galvanic Replacement Reaction between Multiply Twinned Particles of Ag and HAuCl 4 in an Organic Medium. J Am Chem Soc. 2007 Feb 1;129(6):1733–42.

115. da Silva AGM, Rodrigues TS, Haigh SJ, Camargo PHC. Galvanic replacement reaction: recent developments for engineering metal nanostructures towards catalytic applications. Chemical Communications. 2017;53(53):7135–48.

116. Bard AJ, Parsons R, Jordan J. Standard Potentials in Aqueous Solution. Routledge; 2017.

117. Haynes WM, editor. CRC Handbook of Chemistry and Physics. CRC Press; 2014.

118. Pal J, Ganguly M, Dutta S, Mondal C, Negishi Y, Pal T. Hierarchical Au–CuO nanocomposite from redox transformation reaction for surface enhanced Raman scattering and clock reaction. CrystEngComm. 2014;16(5):883–93.

119. Cure J, Assi H, Cocq K, Marìn L, Fajerwerg K, Fau P, et al. Controlled Growth and Grafting of High-Density Au Nanoparticles on Zinc Oxide Thin Films by Photo-Deposition. Langmuir. 2018 Feb 6;34(5):1932–40.

120. Yang YF, Sangeetha P, Chen YW. Au/TiO2 catalysts prepared by photo-deposition method for selective CO oxidation in H2 stream. Int J Hydrogen Energy. 2009 Nov;34(21):8912–20.

121. Karimi MB, Mohammadi F, Hooshyari K. Recent approaches to improve Nafion performance for fuel cell applications: A review. Int J Hydrogen Energy. 2019;44(54):28919–38.

122. Droog JMM, Schlenter B. Oxygen electrosorption on copper single crystal electrodes in sodium hydroxide solution. Journal of Electroanalytical Chemistry. 1980;112(2):387–90.

123. Raciti D, Cao L, Livi KJT, Rottmann PF, Tang X, Li C, et al. Low-overpotential electroreduction of carbon monoxide using copper nanowires. ACS Catal. 2017;7(7):4467–72.

124. Du R, Wu Q, Zhang S, Wang P, Li Z, Qiu Y, et al. Cu C (O) Interfaces Deliver Remarkable Selectivity and Stability for CO2 Reduction to C2+ Products at Industrial Current Density of 500 mA cm− 2. Small. 2023;2301289.

125. Li J, Wang Z, McCallum C, Xu Y, Li F, Wang Y, et al. Constraining CO coverage on copper promotes high-efficiency ethylene electroproduction. Nat Catal. 2019;2(12):1124–31.

126. Jouny M, Luc W, Jiao F. High-rate electroreduction of carbon monoxide to multi-carbon products. Nat Catal. 2018;1(10):748–55.

127. Xiang H, Rasul S, Hou B, Portoles J, Cumpson P, Yu EH. CoppEr–indium binary catalyst On A gas diffusion electrode for high-performance CO2 electrochemical reduction with record CO production efficiency. ACS Appl Mater Interfaces. 2019;12(1):601–8.

128. Ma W, He X, Wang W, Xie S, Zhang Q, Wang Y. Electrocatalytic reduction of CO 2 and CO to multi-carbon compounds over Cu-based catalysts. Chem Soc Rev [Internet]. 2021;50(23):12897–914. Available from: http://xlink.rsc.org/?DOI=D1CS00535A

129. Cervantes-Alcalá R, Miranda-Hernández M. Flow distribution and mass transport analysis in cell geometries for redox flow batteries through computational fluid dynamics. J Appl Electrochem [Internet]. 2018;48(11):1243–54. Available from: https://doi.org/10.1007/s10800-018-1246-7

130. Jia F, Yu X, Zhang L. Enhanced selectivity for the electrochemical reduction of CO2 to alcohols in aqueous solution with nanostructured Cu-Au alloy as catalyst. J Power Sources. 2014;252:85–9.

131. Sandberg RB, Montoya JH, Chan K, Nørskov JK. CO-CO coupling on Cu facets: Coverage, strain and field effects. Surf Sci. 2016;654:56–62.

132. Handoko AD, Wei F, Jenndy, Yeo BS, Seh ZW. Understanding heterogeneous electrocatalytic carbon dioxide reduction through operando techniques. Nat Catal. 2018;1(12):922–34.

133. Hori Y, Koga O, Yamazaki H, Matsuo T. Infrared spectroscopy of adsorbed CO and intermediate species in electrochemical reduction of CO2 to hydrocarbons on a Cu electrode. Electrochim Acta. 1995;40(16):2617–22.

134. Wang X, de Araújo JF, Ju W, Bagger A, Schmies H, Kühl S, et al. Mechanistic reaction pathways of enhanced ethylene yields during electroreduction of CO2–CO co-feeds on Cu and Cu-tandem electrocatalysts. Nat Nanotechnol. 2019;14(11):1063–70.

135. Dubouis N, Grimaud A. The hydrogen evolution reaction: from material to interfacial descriptors. Chem Sci. 2019;10(40):9165–81.

136. Zhang Z, Che H, Gao J, Wang Y, She X, Sun J, et al. Shape-controlled synthesis of Cu 2O microparticles and their catalytic performances in the Rochow reaction. Catal Sci Technol. 2012;2(6):1207–12.

137. Wang C, Lv Z, Yang W, Feng X, Wang B. A rational design of functional porous frameworks for electrocatalytic CO 2 reduction reaction. Chem Soc Rev [Internet]. 2023;52(4):1382–427. Available from: http://xlink.rsc.org/?DOI=D2CS00843B

138. Gao J, Bahmanpour A, Kröcher O, Zakeeruddin SM, Ren D, Grätzel M. Electrochemical synthesis of propylene from carbon dioxide on copper nanocrystals. Nat Chem. 2023 May 6;15(5):705–13.

139. Leonard ME, Clarke LE, Forner-Cuenca A, Brown SM, Brushett FR. Investigating Electrode Flooding in a Flowing Electrolyte, Gas-Fed Carbon Dioxide Electrolyzer. ChemSusChem. 2020;13(2):400–11.

140. Lees EW, Mowbray BAW, Parlane FGL, Berlinguette CP. Gas diffusion electrodes and membranes for CO2 reduction electrolysers. Nat Rev Mater. 2022;7(1):55–64.

141. Shi T, Liu D, Feng H, Zhang Y, Li Q. Evolution of Triple-Phase interface for enhanced electrochemical CO2 reduction. Chemical Engineering Journal. 2022;431:134348.

142. Shi T, Liu D, Liu N, Zhang Y, Feng H, Li Q. Triple-Phase Interface Engineered Hierarchical Porous Electrode for CO2 Electroreduction to Formate. Advanced Science. 2022;9(30):2204472.

143. Bohra D, Chaudhry J, Burdyny T, Pidko E, Smith W. Mass transport in catalytic pores of GDE-based CO2 electroreduction systems. 2020;

144. Liu K, Smith WA, Burdyny T. Introductory guide to assembling and operating gas diffusion electrodes for electrochemical CO2 reduction. ACS Energy Lett. 2019;4(3):639–43.

145. Erbil HY. Precursor film formation on catalyst–electrolyte–gas boundaries during CO2 electroreduction with gas diffusion electrodes. Catal Sci Technol [Internet]. 2022;12(23):6933–44. Available from: http://dx.doi.org/10.1039/D2CY01576E

146. Li P, Bi J, Liu J, Wang Y, Kang X, Sun X, et al. p–d Orbital Hybridization Induced by p-Block Metal-Doped Cu Promotes the Formation of C2+ Products in Ampere-Level CO2 Electroreduction. J Am Chem Soc. 2023;145(8):4675–82.

147. Fang M, Wang M, Wang Z, Zhang Z, Zhou H, Dai L, et al. Hydrophobic, Ultrastable Cuδ+ for Robust CO2 Electroreduction to C2 Products at Ampere-Current Levels. J Am Chem Soc. 2023;

148. Sheng Y, Guo Y, Yu H, Deng K, Wang Z, Li X, et al. Engineering under-coordinated active sites with tailored chemical microenvironments over mosaic bismuth nanosheets for selective CO2 electroreduction to formate. Small. 2023;19(16):2207305.

149. Gharibi H, Faraji M, Kheirmand M. The Role of PANI/Nafion on the Performance of ORR in Gas Diffusion Electrodes of PEM Fuel Cell. Electroanalysis. 2012;24(12):2354–64.

150. Knake R, Jacquinot P, Hauser PC. A direct comparison of amperometric gas sensors with gas-diffusion and ion-exchange membrane based electrodes. ANALYST. 2002 Jan;127(1):114–8.

151. Qi Z, Dong H, Yu H, Zhang X, Yu H. In-situ electrochemical DeNOx under mild conditions depending on perovskite-modified gas diffusion electrode. CHEMICAL ENGINEERING JOURNAL. 2019 Feb;358:666–78.

152. Lin Y, Wang T, Zhang L, Zhang G, Li L, Chang Q, et al. Tunable CO2 electroreduction to ethanol and ethylene with controllable interfacial wettability. Nat Commun. 2023;14(1):3575.

153. Shao T, Yang K, Chen S, Zheng M, Zhang Y, Li Q, et al. Tackling the proton limit under industrial electrochemical CO2 reduction by a local proton shuttle. Carbon Energy. 2023;e416.

154. Chang S, Xuan Y, Duan J, Zhang K. High-performance electroreduction CO2 to formate at Bi/Nafion interface. Appl Catal B. 2022;306:121135.

155. Lees EW, Mowbray BAW, Salvatore DA, Simpson GL, Dvorak DJ, Ren S, et al. Linking gas diffusion electrode composition to CO2 reduction in a flow cell. J Mater Chem A [Internet]. 2020;8(37):19493–501. Available from: http://dx.doi.org/10.1039/D0TA03570J

156. Philips MF, Pavesi D, Wissink T, Figueiredo MC, Gruter GJM, Koper MTM, et al. Electrochemical CO2 reduction on gas diffusion electrodes: enhanced selectivity of in–Bi bimetallic particles and catalyst layer optimization through a design of experiment approach. ACS Appl Energy Mater. 2022;5(2):1720–30.

157. de Sousa L, Harmoko C, Benes N, Mul G. Optimizing the ink formulation for preparation of Cu-based gas diffusion electrodes yielding ethylene in electroreduction of CO2. ACS ES&T Engineering. 2021;1(12):1649–58.

158. Wang M, Wan L, Luo J. Promoting CO2 electroreduction on CuO nanowires with a hydrophobic Nafion overlayer. Nanoscale [Internet]. 2021;13(6):3588–93. Available from: http://dx.doi.org/10.1039/D0NR08369K

159. García de Arquer FP, Dinh CT, Ozden A, Wicks J, McCallum C, Kirmani AR, et al. CO2 electrolysis to multicarbon products at activities greater than 1 A cm−2. Science (1979). 2020;

160. Shin SJ, Choi H, Ringe S, Won DH, Oh HS, Kim DH, et al. A unifying mechanism for cation effect modulating C1 and C2 productions from CO2 electroreduction. Nat Commun [Internet]. 2022;13(1):5482. Available from: https://doi.org/10.1038/s41467-022-33199-8

161. Li X, Forouzandeh F, Kakanat AJ, Feng F, Banham DWH, Ye S, et al. Surface Characteristics of Microporous and Mesoporous Carbons Functionalized with Pentafluorophenyl Groups. ACS Appl Mater Interfaces. 2018;10(2):2130–42.

162. Atwa M, Li X, Wang Z, Dull S, Xu S, Tong X, et al. Scalable nanoporous carbon films allow line-of-sight 3D atomic layer deposition of Pt: Towards a new generation catalyst layer for PEM fuel cells. Mater Horiz. 2021;8(9):2451–62.

163. Islam MN, Shrivastava U, Atwa M, Li X, Birss V, Karan K. Highly Ordered Nanoporous Carbon Scaffold with Controllable Wettability as the Microporous Layer for Fuel Cells. ACS Appl Mater Interfaces. 2020;12(35):39215–26.

164. Li X, Forouzandeh F, Kakanat AJ, Feng F, Banham DWH, Ye S, et al. Surface Characteristics of Microporous and Mesoporous Carbons Functionalized with Pentafluorophenyl Groups. ACS Appl Mater Interfaces. 2018;10(2):2130–42.

165. Butkutė A, Merkininkaitė G, Jurkšas T, Stančikas J, Baravykas T, Vargalis R, et al. Femtosecond Laser Assisted 3D Etching Using Inorganic-Organic Etchant. Vol. 15, Materials. 2022.

166. Morales DM, Risch M. Seven steps to reliable cyclic voltammetry measurements for the determination of double layer capacitance. JPhys Energy. 2021;3(3).

167. Modestino MA, Kusoglu A, Hexemer A, Weber AZ, Segalman RA. Controlling nafion structure and properties via wetting interactions. Macromolecules. 2012;45(11):4681–8.

168. Wang H, Pilon L. Physical interpretation of cyclic voltammetry for measuring electric double layer capacitances. Electrochim Acta. 2012;64:130–9.

169. Pech D, Brunet M, Durou H, Huang P, Mochalin V, Gogotsi Y, et al. Ultrahigh-power micrometre-sized supercapacitors based on onion-like carbon. Nat Nanotechnol. 2010;5(9):651–4.

170. Yoo JJ, Balakrishnan K, Huang J, Meunier V, Sumpter BG, Srivastava A, et al. Ultrathin planar graphene supercapacitors. Nano Lett. 2011;11(4):1423–7.

171. Ma M, Hill RM. Superhydrophobic surfaces. Curr Opin Colloid Interface Sci. 2006;11(4):193–202.

172. Li XM, Reinhoudt D, Crego-Calama M. Erratum: What do we need for a superhydrophobic surface? A review on the recent progress in the preparation of superhydrophobic surfaces (Chemical Society Reviews (2007) 36 (1350-1368) DOI: 10.1039/b602486f). Chem Soc Rev. 2007;36(9):1529.

173. Marshall JE, Zhenova A, Roberts S, Petchey T, Zhu P, Dancer CEJ, et al. On the solubility and stability of polyvinylidene fluoride. Polymers (Basel). 2021;13(9):1354.

174. Kuwertz R, Kirstein C, Turek T, Kunz U. Influence of acid pretreatment on ionic conductivity of Nafion® membranes. J Memb Sci. 2016;500:225–35.

175. Allen FI, Comolli LR, Kusoglu A, Modestino MA, Minor AM, Weber AZ. Morphology of hydrated as-cast Nafion revealed through cryo electron tomography. ACS Macro Lett. 2015;4(1):1–5.

176. Lolla D, Gorse J, Kisielowski C, Miao J, Taylor PL, Chase GG, et al. Polyvinylidene fluoride molecules in nanofibers, imaged at atomic scale by aberration corrected electron microscopy. Nanoscale. 2016;8(1):120–8.

177. Papaderakis AA, Polus K, Kant P, Box F, Etcheverry B, Byrne C, et al. Taming electrowetting using highly concentrated aqueous solutions. The Journal of Physical Chemistry C. 2022;126(49):21071–83.

178. O'Hagan D. Understanding organofluorine chemistry. An introduction to the C–F bond. Chem Soc Rev. 2008;37(2):308–19.

179. Heo J, Ahn H, Won J, Son JG, Shon HK, Lee TG, et al. Electro-inductive effect: Electrodes as functional groups with tunable electronic properties. Science (1979). 2020;370(6513):214–9.

180. Siodła T, Oziminski WP, Hoffmann M, Koroniak H, Krygowski TM. Toward a physical interpretation of substituent effects: the case of fluorine and trifluoromethyl groups. J Org Chem. 2014;79(16):7321–31.

181. Saarinen V, Kreuer KD, Schuster M, Merkle R, Maier J. On the swelling properties of proton conducting membranes for direct methanol fuel cells. Solid State Ion. 2007;178(7–10):533–7.

182. Li X, Feng F, Zhang K, Ye S, Kwok DY, Birss V. Wettability of Nafion and Nafion/Vulcan carbon composite films. Langmuir. 2012;28(16):6698–705.

183. Macpherson J V, Unwin PR. Combined scanning electrochemical− atomic force microscopy. Anal Chem. 2000;72(2):276–85.

184. Perry SC, Gateman SM, Malpass-Evans R, McKeown N, Wegener M, Nazarovs P, et al. Polymers with intrinsic microporosity (PIMs) for targeted CO2 reduction to ethylene. Chemosphere. 2020;248.

185. Weber N, Linkhorst J, Keller R, Wessling M. Tailoring Pore Networks–Gas Diffusion Electrodes via Additive Manufacturing. Adv Mater Technol. 2023;8(21):2300720.

186. Wicks J, Jue ML, Beck VA, Oakdale JS, Dudukovic NA, Clemens AL, et al. 3D-Printable Fluoropolymer Gas Diffusion Layers for CO2 Electroreduction. Advanced Materials [Internet]. 2021 Feb 1;33(7):2003855. Available from: https://doi.org/10.1002/adma.202003855

187. Yang S, Wang H, Xiong Y, Zhu M, Sun J, Jiang M, et al. Ultrafast Thermal Shock Synthesis and Porosity Engineering of 3D Hierarchical Cu–Bi Nanofoam Electrodes for Highly Selective Electrochemical CO2 Reduction. Nano Lett. 2023;23(22):10140–7.

188. Wang Y, Lei H, Lu S, Yang Z, Xu B Bin, Xing L, et al. Cu2O nano-flowers/graphene enabled scaffolding structure catalyst layer for enhanced CO2 electrochemical reduction. Appl Catal B. 2022;305:121022.

189. Guzmán H, Roldán D, Russo N, Hernández S. Ultrasound-assisted synthesis of copper-based catalysts for the electrocatalytic CO2 reduction: Effect of ultrasound irradiation, precursor concentration and calcination temperature. Sustainable Materials and Technologies. 2023;35:e00557.

190. Hoffmann H, Kutter M, Osiewacz J, Paulisch-Rinke MC, Lechner S, Ellendorff B, et al. Highly selective Ag foam gas diffusion electrodes for CO 2 electroreduction by pulsed hydrogen bubble templation. EES Catalysis. 2024;2(1):286–99.

191. Weng LC, Bell AT, Weber AZ. Modeling gas-diffusion electrodes for CO 2 reduction. Physical Chemistry Chemical Physics. 2018;20(25):16973–84.

192. Young AP, Schwartz CM. Electrical conductivity and thermoelectric power of Cu2O. Journal of Physics and Chemistry of Solids. 1969;30(2):249–52.

193. Liu C, Sun C, Gao Y, Lan W, Chen S. Improving the Electrochemical Properties of Carbon Paper as Cathodes for Microfluidic Fuel Cells by the Electrochemical Activation in Different Solutions. ACS Omega [Internet]. 2021 Jul 27;6(29):19153–61. Available from: https://doi.org/10.1021/acsomega.1c02507

194. Jannakoudakis AD, Jannakoudakis PD, Theodoridou E, Besenhard JO. Electrochemical oxidation of carbon fibres in aqueous solutions and analysis of the surface oxides. J Appl Electrochem [Internet]. 1990;20(4):619–24. Available from: https://doi.org/10.1007/BF01008872

195. Gupta K, Bersani M, Darr JA. Highly efficient electro-reduction of CO 2 to formic acid by nano-copper. J Mater Chem A Mater. 2016;4(36):13786–94.

196. Heßelmann M, Bräsel BC, Keller RG, Wessling M. Simulation-based guidance for improving ??? reduction on silver gas diffusion electrodes. 2022;

197. Li F, Thevenon A, Rosas-Hernández A, Wang Z, Li Y, Gabardo CM, et al. Molecular tuning of CO2-to-ethylene conversion. Nature. 2020;577(7791):509–13.

198. Morawietz T, Handl M, Oldani C, Friedrich KA, Hiesgen R. Quantitative in situ analysis of ionomer structure in fuel cell catalytic layers. ACS Appl Mater Interfaces. 2016;8(40):27044–54.

199. Tarokh A, Karan K, Ponnurangam S. Atomistic MD study of nafion dispersions: Role of solvent and counterion in the aggregate structure, ionic clustering, and acid dissociation. Macromolecules. 2019;53(1):288–301.

200. Bushuyev OS, De Luna P, Dinh CT, Tao L, Saur G, van de Lagemaat J, et al. What Should We Make with CO2 and How Can We Make It? Joule. 2018;2(5):825–32.

201. Zheng Y, Vasileff A, Zhou X, Jiao Y, Jaroniec M, Qiao SZ. Understanding the Roadmap for Electrochemical Reduction of CO2 to Multi-Carbon Oxygenates and Hydrocarbons on Copper-Based Catalysts. J Am Chem Soc. 2019;141(19):7646–59.

202. Xiang H. Development of electrochemical CO2 reduction to gas and liquid fuels in aqueous media with scale-up potential. Newcastle University; 2019.